

# Direct observation of the moisture distribution in heated calcium alumina- and hydratable alumina-bonded castables during first-drying, using NMR imaging

**Citation for published version (APA):**

Barakat, A. J. (2019). *Direct observation of the moisture distribution in heated calcium alumina- and hydratable alumina-bonded castables during first-drying, using NMR imaging*. [Phd Thesis 1 (Research TU/e / Graduation TU/e), Applied Physics and Science Education]. Technische Universiteit Eindhoven.

**Document status and date:**

Published: 27/11/2019

**Document Version:**

Publisher's PDF, also known as Version of Record (includes final page, issue and volume numbers)

**Please check the document version of this publication:**

- A submitted manuscript is the version of the article upon submission and before peer-review. There can be important differences between the submitted version and the official published version of record. People interested in the research are advised to contact the author for the final version of the publication, or visit the DOI to the publisher's website.
- The final author version and the galley proof are versions of the publication after peer review.
- The final published version features the final layout of the paper including the volume, issue and page numbers.

[Link to publication](#)

**General rights**

Copyright and moral rights for the publications made accessible in the public portal are retained by the authors and/or other copyright owners and it is a condition of accessing publications that users recognise and abide by the legal requirements associated with these rights.

- Users may download and print one copy of any publication from the public portal for the purpose of private study or research.
- You may not further distribute the material or use it for any profit-making activity or commercial gain
- You may freely distribute the URL identifying the publication in the public portal.

If the publication is distributed under the terms of Article 25fa of the Dutch Copyright Act, indicated by the "Taverne" license above, please follow below link for the End User Agreement:

[www.tue.nl/taverne](http://www.tue.nl/taverne)

**Take down policy**

If you believe that this document breaches copyright please contact us at:

[openaccess@tue.nl](mailto:openaccess@tue.nl)

providing details and we will investigate your claim.

Direct observation of the moisture  
distribution in heated calcium alumina-  
and hydratable alumina-bonded castables  
during first-drying, using NMR imaging

Ahmed Jamal Barakat



Direct observation of the moisture distribution in heated  
calcium alumina- and hydratable alumina-bonded castables  
during first-drying, using NMR imaging

PROEFSCHRIFT

ter verkrijging van de graad van doctor aan de Technische Universiteit Eindhoven, op gezag  
van de rector magnificus prof.dr.ir. F.P.T. Baaijens,  
voor een commissie aangewezen door het College voor Promoties, in het openbaar te  
verdedigen op woensdag 27 november 2019 om 16:00 uur

door

Ahmed Jamal Barakat

geboren te Los Angeles, California, Verenigde Staten van Amerika

Dit proefschrift is goedgekeurd door de promotoren en de samenstelling van de promotiecommissie is als volgt:

voorzitter:	prof.dr.ir. G.M.W. Kroesen
1 <sup>e</sup> promotor:	prof.dr.ir. O.C.G. Adan
2 <sup>e</sup> promotor:	prof.dr.rer.nat. O. Krause (Koblenz University of Applied Sciences)
copromotor:	dr.ir. L. Pel
leden:	prof.dr. P. McDonald (University of Surrey)
	prof.dr. P. Coussot (Université Paris-Est)
	prof.dr.ir. D.M.J. Smeulders

*Het onderzoek of ontwerp dat in dit proefschrift wordt beschreven is uitgevoerd in overeenstemming met de TU/e Gedragscode Wetenschapsbeoefening.*

*To the future*

ISBN: 978-94-91909-54-2

Cover design: photo provided by Almatiss/designed by ProefschriftMaken.

Printed by: ProefschriftMaken (<http://www.proefschriftmaken.nl>).

This research was carried out in the group Transport in Permeable Media at the Eindhoven University of Technology, faculty of Applied Physics under project number M41.6.12464 in the framework of the Research Program of the Materials innovation institute (M2i) ([www.m2i.nl](http://www.m2i.nl)) supported by the Dutch government as well as Tata Steel, Almatiss, Imerys Aluminates and Elkem.

# TABLE OF CONTENTS

<b>1: INTRODUCTION .....</b>	<b>7</b>
1.1 REFRACTORIES: THE HISTORICAL BACKGROUND .....	7
1.2 INDUSTRIAL APPLICATION .....	8
1.3 THE RESEARCH CHALLENGE .....	11
1.4 REFRACTORY CASTABLES .....	14
1.4.1 CASTABLE BOND SYSTEMS .....	15
1.4.2 HYDRATION MECHANISMS OF CASTABLES .....	15
1.5 FIRST-DRYING OF CASTABLES: HEATING SCHEDULES .....	18
1.6 LIQUID-VAPOUR TRANSPORT .....	20
1.7 THE RESEARCH GOAL .....	24
1.8 OUTLINE OF THESIS .....	26
1.9 REFERENCES .....	28
<b>2: HIGH-TEMPERATURE NUCLEAR MAGNETIC RESONANCE (NMR).....</b>	<b>31</b>
2.1 INTRODUCTION .....	32
2.2 EXPERIMENTAL SETUP .....	34
2.3 NMR SIGNAL TEMPERATURE DEPENDENCE .....	37
2.3.1 TEMPERATURE INFLUENCE .....	37
2.3.2 RELAXATION CORRECTION .....	39
2.3.3 OVERALL TEMPERATURE CORRECTION .....	41
2.4 FIRST DRYING OF CASTABLES .....	43
2.4.1 SAMPLE PREPARATION .....	43
2.4.2 MOISTURE CONTENT DURING FIRST-DRYING .....	43
2.5 CONCLUSION .....	46
2.6 REFERENCES .....	47
<b>3: DIRECT OBSERVATION OF THE BOILING FRONT BEHAVIOR .....</b>	<b>49</b>
3.1 INTRODUCTION .....	50
3.2 FIRST-DRYING THEORY: A FIRST-ORDER APPROXIMATION .....	51
3.3 EXPERIMENTAL SETUP.....	54
3.4 SAMPLE PREPARATION .....	56
3.4.1 MEASURING MOISTURE LOSS DURING FIRST-DRYING .....	58
3.4.2 COMPARING EXPERIMENTAL RESULTS WITH THE CONCEPTUAL MODEL .....	66
3.5 DRYING BEHAVIOR OF CASTABLES: RESULTS AND DISCUSSION .....	69
3.6 CONCLUSION.....	75
3.7 REFERENCES.....	77
<b>4: INFLUENCE OF PORE STRUCTURE ON VAPOUR TRANSPORT .....</b>	<b>81</b>
4.1 INTRODUCTION .....	82

4.2 EXPERIMENTAL SETUP .....	84
4.3 SAMPLE PREPARATION .....	86
4.4 MOISTURE LOSS DURING FIRST DRYING AS DETERMINED BY NMR .....	87
4.4.1 REGULAR CASTABLES.....	87
4.4.2 HEAT TRANSPORT IN CASTABLES.....	92
4.4.3 FIBER-FREE NCC AND LCC .....	97
4.4.4 THE EFFECT OF FIBER-ADDITION ON DRY-OUT .....	99
4.4.5 MIPORE-FREE LCC FUME .....	101
4.4.6 THE EFFECT OF MIPORE-ADDITION ON DRY-OUT.....	103
4.5 CONCLUSION.....	106
4.6 REFERENCES .....	108
<b>5: MOISTURE TRANSPORT IN HEATED PINE WOOD.....</b>	<b>111</b>
5.1 INTRODUCTION .....	112
5.2 SAMPLE PREPARATION .....	113
5.3 EXPERIMENTAL SETUP .....	113
5.4 T <sub>2</sub> RELAXATION AND SIGNAL CORRECTION .....	115
5.5 DISCUSSION AND RESULTS.....	117
5.5.1 MOISTURE CONTENT AND TEMPERATURE DISTRIBUTION.....	117
5.5.2 PEAK IN MOISTURE CONTENT.....	121
5.5.3 LOW HEATING RATE .....	123
5.6 CONCLUSION.....	124
5.7 REFERENCES .....	125
<b>6: CONCLUSIONS AND OUTLOOK.....</b>	<b>129</b>
6.1 CONCLUSIONS.....	129
6.2 OUTLOOK .....	134
6.2.1 HEATING RATE .....	134
6.2.2 TEMPERATURE .....	136
6.2.3 TEMPERATURE GRADIENT.....	136
6.2.4 NMR RELAXATION.....	136
6.2.5 MIPORE ADDITION.....	138
6.3 REFERENCES .....	144
<b>SUMMARY .....</b>	<b>145</b>
<b>SAMENVATTING .....</b>	<b>149</b>
<b>JOURNAL PUBLICATIONS.....</b>	<b>153</b>
<b>ACKNOWLEDGMENTS .....</b>	<b>155</b>
<b>CURRICULUM VITAE.....</b>	<b>157</b>



---

# Chapter 1: Introduction

---

## 1.1 Refractories: The Historical Background

The first actual use of materials with refractory properties is likely dated as far back as 5000 B.C. Egypt, where gold was melted inside clay-derived crucibles [1]. In fact, the Egyptians and Romans already discovered the hydraulic qualities of reacting lime and alumina [2].

The use of high-temperature refractory furnaces to melt iron can be traced back to 1300, when tall furnaces were first constructed. Some of the earliest furnaces were lined with natural sandstone, but the higher temperatures achieved by the 17th century blast furnaces led to the development of manufactured firebrick from kaolinite-rich clay. The pre-World War II installations used chimney-like hearthwalls derived from fireclay brick that were watercooled through cast-iron stave cooling channels [3].

By the end of the 18<sup>th</sup> century, the industrial revolution was kicking off and thus providing brick manufacturers with more economical access to refractory production. Hand-molded fireclay bricks ultimately replaced natural stone products. Thanks to the industrial revolution, fabrication of bricks in mechanical presses commenced, thus allowing producers to achieve the temperatures required for producing bricks with physical properties comparable to those of the modern day, i.e., several hundreds of degrees celsius [4].

In the early industrial revolution, crushed Dinas rock was utilized to form silica brick made of nearly pure silica, cemented together with very little binding flux (e.g. lime). These brick have been developed by William Weston Young, a porcelain manufacturer, in 1820. They were the most suitable refractory for lining acid open hearth furnaces, where temperatures were much higher than in Bessemer converters [3]. Toward the end of the 19<sup>th</sup> century, the use of doloma as a refractory aggregate would be utilized for tar-bonded bricks. With the introduction of the basic oxygen furnace after WWII, standard basic brick that contained

magnesia, dolomite, and chromite aggregates and matrix powders were developed containing tars and pitches for use in steel melting.

### **1.2 Industrial Application**

In the 21<sup>st</sup> century, conventional use of refractories has come to mean technological materials that are used to line the vessels and crucibles of various steel- and iron-processing facilities (see Figure 1.1). The operation conditions of these industrial sectors require exposure to ceramic temperatures in the full service range of 1000-2000 °C. These temperatures vary for different processes, where in the case of saturated pig iron the melting point is 1400 °C; but the exothermic conversion process in an oxygen blast converter is cooled down to 2000 °C. These are the typical service temperatures at which the vessels are heated as they receive and process molten steel and iron, and thus the lining is exposed to steel and slag contacts at these temperatures. More broadly speaking, refractories are also utilized in (but not limited to) the non-ferrous metallurgy, glass-making and petrochemicals industries, as well as many other sectors too [5].

As 70 % of their consumption is in the basic metals industry (particularly iron and steel), refractories are supposed to be resistant to heat, with exposure to varying degrees of mechanical stress and strain, thermal stress, liquid and gaseous attack, and abrasion over wide temperature ranges [5]. Accordingly, refractories must be designed to ensure structural volume-stability and high mechanical strength under these extreme conditions.

Furthermore, the total global steel production output currently stands above 1000 megatons per year and the lifetime of a steel ladle is close to 80 heats [6]. The refractories consumption ratio is set by 10 kg per ton of steel and overall demand has more than doubled in the last two decades [7]. Therefore, the world supply of industrial resources depends on the availability of adequately performing refractory technology.

All refractories are derived, in varying proportions, from the following list of oxides: alumina, silica, magnesia, chromia and calcia [8]. Refractories are generally divided into two families: shaped and unshaped (monolithic) materials. By definition, monolithics e.g. castables, are premixed combinations of refractory aggregates, bonding agents, fine fillers, and deflocculants to promote workability and other rheological properties [9]. Table 1.1

shows refractory production levels by major producer countries in 2007. As can be seen, the EU and China clearly are heavily reliant on the refractories industry.

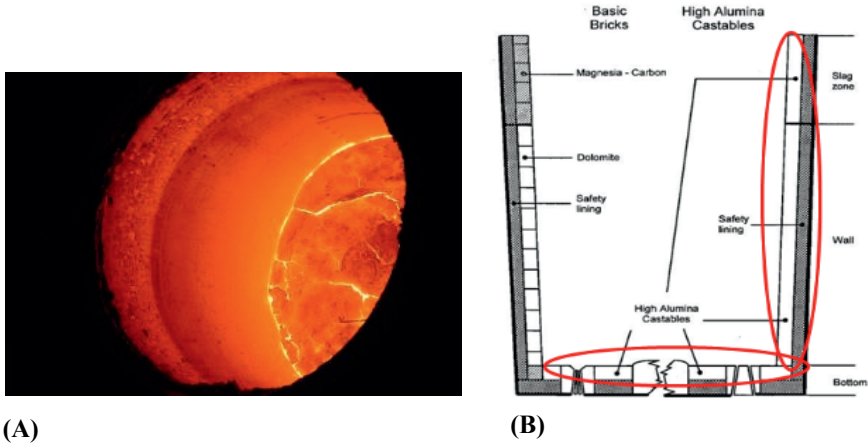


**Figure 1.1:** (A) A photograph of a typical steel ladle where molten steel is processed and transported. (B) A schematic overview of a steel ladle showing the refractory lining.

**Table 1.1:** Refractories production by country of major share.

Country	Total (m.t.)	Shaped (m.t.)	Unshaped (m.t.)	Share Unshaped (%)
European Union	7.3	4.3	3.0	40
USA	2.5	1.4	1.1	45
Japan	1.1	0.36	0.74	67
China	~24	~16	~8	~35
Russia	~2.5	~1.5	~1.0	~40

\*m.t. = million tonnes

On the basis of physical properties alone, shaped refractories can be subdivided into dense bricks e.g. conventional, fusion cast, etc. and insulation materials e.g. bricks, fibrous, etc. On the other hand, monolithics are comprised of mortars, plastics, ramming mixes, high-alumina castables, etc. These physical properties are associated with the way in which refractories are manufactured and distributed. An overview of the different material families is given in Table 1.2, along with the advantages and disadvantages of each family, e.g. spalling resistance (strength), thermal and insulation properties (conductivity), etc. in relation to their specific function within the refractory lining [1].

The monolithics family have seen an expansion in their use since the beginning of the 20th century, the demand of which exploded since WWII where net total production of ramming mixes, castables, mortars, and coatings increased by more than one-third between 1937 and 1943 [10]. In 2007, Japanese production of unshaped refractories outnumbered shaped materials two-fold.

**Table 1.2:** *A list of the different refractory families and their associated properties.*

<b>Material Family</b>	Dense Brick (< 40 vol. % porosity)	Insulation (>40 vol. % porosity)	Monolithics
<b>Material Subfamily</b>	<ul style="list-style-type: none"> <li>• Conventional</li> <li>• Fusion Cast</li> <li>• Iso-Pressed/Slip Cast</li> <li>• Ceramic Bond</li> <li>• Chemical Bond</li> </ul>	<ul style="list-style-type: none"> <li>• Brick</li> <li>• Fibrous</li> </ul>	<ul style="list-style-type: none"> <li>• Mortars</li> <li>• Plastics</li> <li>• Ramming Mixes</li> <li>• Coatings</li> <li>• Gunning Mixes</li> <li>• Hydrated Castables</li> </ul>
<b>Advantages</b>	<ul style="list-style-type: none"> <li>• Good cold/hot strength</li> <li>• Good slag resistance</li> </ul>	<ul style="list-style-type: none"> <li>• Low Thermal Conductivity</li> <li>• Lightweight</li> </ul>	<ul style="list-style-type: none"> <li>• Good spalling resistance</li> <li>• Low Thermal Conductivity</li> </ul>
<b>Disadvantages</b>	<ul style="list-style-type: none"> <li>• Structural stability</li> <li>• Expensive shaping</li> <li>• Requires skilled labour for installation</li> <li>• High Thermal Conductivity</li> </ul>	<ul style="list-style-type: none"> <li>• Poor cold/hot strength</li> <li>• Poor slag resistance</li> </ul>	<ul style="list-style-type: none"> <li>• Special installation techniques</li> <li>• Quality of installation not easily visible</li> <li>• Different labour skills compared to brick</li> </ul>

### 1.3 The Research Challenge

In contrast to shaped refractories (e.g. magnesia-carbon bricks), the installation of unshaped monolithic refractories (i.e., castables) require less maintenance costs and fewer repairs where they can be rapidly installed. This is due to the fact that improvements have been made over the years in placement and installation, mixing process, water content, curing conditions, strength development, etc. It is for this reason that today monolithics make up more than twice the production output of bricks in countries like Japan [11].

Despite these improvements, high-alumina castables still pose a serious challenge as they contain a significant quantity of moisture that is transformed into highly pressurized steam from 100-300 °C. This high pressure build-up is induced by the low-permeability microstructure entrapping the moisture. Removing this pressurized moisture is critical to ensuring a safe first-heat up for industrial service.

In Figure 1.2A, a schematic plot of the vapour pressure as a function of time (dashed line), along with the corresponding furnace temperature (solid line), is given for three different heating rates (in decreasing order):  $H_1$ ,  $H_2$  and  $H_3$ . The higher the heating rate, the faster the temperature increases and thus also the vapour pressure build-up. The final furnace temperature is the same for all heating rates. If the permeability is too low, moisture cannot be released faster than the pressure increases. In this case, the rapid heat-up will cause the vapour pressure to quickly climb above the *green tension strength* of the material  $\sigma_{\text{green}}$ , which is the mechanical resistance attained during the hardening stage of the curing process (prior to heating) and corresponds to the hydrate phases only. If this pressure development occurs, the material will be destroyed in the process of a violent explosion. Therefore, slow pre-drying, also known as *first-drying*, of castable materials is typically necessary.

As a consequence of the vapour pressure development in castables, special attention is required during the curing process, i.e., conditions of aging since the moment of formulation. This is to ensure the optimal development of the material's mechanical and microstructural properties, i.e., green strength and permeability. In Figure 1.2B, the explosive spalling temperature (solid line) and the green strength (dashed line) are plotted as a function of curing temperature. The explosive spalling temperature corresponds to the maximum sample temperature just before the material will explode. For high curing temperatures, the green

strength will increase and shift the spalling temperature to higher values (in correlation with the higher green strength). This is due to the fact that at higher curing temperatures, the pore microstructure is more permeable and at the same time will display higher strength [11].

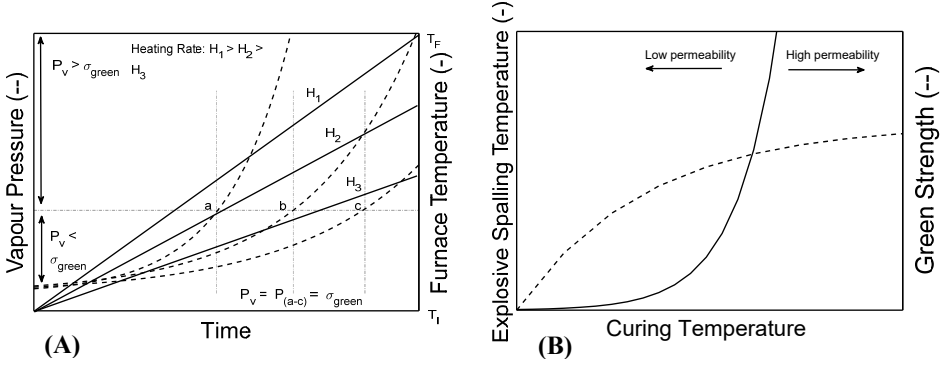


**Figure 1.2:** Schematic of the industrial challenge of drying castables. (A) A plot of the vapour pressure (dashed line) and the furnace temperature (solid line) as a function of time, shown for three different heating rates (in decreasing order):  $H_1, H_2, H_3$ . Regardless of the chosen heating rate, the final furnace temperature is the same. Three critical stages of pressure build-up are considered with reference to the green strength  $\sigma_{green}$ :  $P_v > \sigma_{green}$ ;  $P_v = \sigma_{green}$ ;  $P_v < \sigma_{green}$ . Points a, b and c correspond to  $P_v = \sigma_{green}$ . (B) The explosive spalling temperature (solid line) and green strength (dashed line) are plotted as a function of curing temperature. The lower the permeability, the lower the explosive spalling temperature and the higher the permeability, the higher the explosive spalling temperature.

Using a curing temperature that is too low can, in fact, decrease the density, green strength and increase the amount of water contained in the hydrates thereby heightening the risk of explosive spalling [12]. This is because hydrate formation is a kinetically driven process, where lower temperatures may inhibit the formation of hydrates and lead to water rich calcium alumina phases e.g.  $CAH_{10}$  that release water at temperatures below 200 °C. The relationship between low strength and low curing temperature has already been visualized in Figure 1.2B, where the maximum explosion temperature plotted as a function of temperature drops with decreasing curing temperature and green strength. Therefore, a carefully chosen curing temperature and well-controlled ambient environment is critical to perfecting high-quality castable technology. The industrial standard (EN ISO 1927) is to choose a curing temperature and time of at least 20 °C and 48 hours, respectively, which is high enough to ensure adequate strength development, i.e., via the development of stable hydraulic phases within a sufficient amount of time. This is a typical match for ambient conditions in the

laboratory. Using a curing temperature less than 20 °C will require a longer curing time, introducing metastable hydrate phases and thus increase the risk of spalling.

To remedy concerns of mechanical failure, from a materials design point-of-view, various additives are used for promoting permeability and thus safe escape of the moisture in deflocculating castables (medium/low/non-cement systems). Some of these schemes include polypropylene fibers, which are known to melt and open up continuous, permeable pathways for the steam to safely escape in the temperature range of 160-200 °C [13][14][15][16].

The spalling temperature of a material is very much a function of the castable properties, i.e., curing conditions, binder content, etc. as well as the applied heating rate. Cardoso et al. (2004) found that calcium aluminate cement-bonded samples which were cured for 16 days displayed a higher strength development (more than 3-fold), despite a reduced permeability compared to samples cured for 1 day and therefore were more likely to explode, albeit at a higher temperature of 440 °C vs. 416 °C when subjected to an aggressive heating rate of 20 °C/minute [17]. When a CAC- and HA-bonded sample cured for 48 hours were subjected to the same aggressive heating rate of 20 °C/minute, the latter exploded at 256 °C, despite having a wider temperature range of moisture release [18].

Concerning the adjustment of the heat-up schedule, it is important to remember that while increasing the *furnace* heating rate will decrease the total drying time (as shown in Figure 1.2A), the final temperature at which the *sample* has fully dried is higher than that of the samples with lower heating rates. In other words, even though a constant furnace heating program is chosen (e.g. 1 °C/min vs. 10 °C/min) and the final furnace temperature the same in all cases (700 °C), the sample heating rate is non-linear thus resulting in different temperatures of moisture release. Innocentini et al. (2003) found that increasing the sample's heating rate by a factor of 10 corresponded with a 45 % increase of the final drying temperature (180 to 260 °C), even though the timescale of drying was shorter [19]. This is due to the fact that water vapour is being generated faster than it can be released, thus leading to a shift of the vapour pressure to higher temperatures.

As can be seen from these industrial trials, in this lower range of temperatures (< 300 °C) spalling is expected to occur before the moisture even has a chance to evacuate the system. Therefore, a quantitative understanding of the moisture distribution in the regime of first-

drying (100-300 °C) is a crucial, yet up to this point only vaguely understood aspect of drying schedules.

In the succeeding sections, the physical and chemical properties of refractory castables will be presented, as well as the different material families of castables along with their advantages and disadvantages. This will be followed by an introduction to the industrial problem of first-drying and the experimental techniques available for investigating the dewatering process during pre-drying of castables, as well as the stated goal of this thesis.

#### 1.4 Refractory Castables

According to the International Standards definition of castables (ISO 1927-1) castables are mixtures of aggregates and bonds, supplied in a dry state requiring only a water/or liquid component for mixing. Furthermore, they are placed by casting and vibration, where the bond is formed by hardening.. For the interest of discussion here, we present three different categories of materials (based on the recipe formulation) that will be considered in this study:

- Regular Castables (RC): 20 % Calcium Alumina Cement; 9 % H<sub>2</sub>O.
- Low-Cement Castables (LCC): 5 % Calcium Alumina Cement; 4-5 % H<sub>2</sub>O.
- Non-Cement Castables (NCC): 3 % Hydratable Alumina Binder; 4-5 % H<sub>2</sub>O.

More generally speaking, the international classification of castables according to ISO 1927-1 is as follows:

- Medium-Cement Castables (MCC); CaO content > 2.5 %
- Low-Cement Castables (LCC); 1 % < CaO content ≤ 2.5 %
- Ultra-Low Cement Castables (ULCC); 0.2 % < CaO content ≤ 1 %
- Non-Cement Castables (NCC); 0 % < CaO content ≤ 0.2 %

As already stated, castables (a subclass of monolithic refractories) are composed of various components: aggregates, binder, fines and deflocculants for promoting workability and other rheological properties. Officially, deflocculated castables contain at least 1 deflocculant and at least 2 % ultrafine particles less than 1 micron in size (i.e., excluding RC). The aggregates compose the skeleton and the binder is required to bond the matrix components together. The majority of these castable systems are supplied as bagged, blended mixes in the dry state. At the point of installation, castables require a liquid water additive, i.e., for wet mixing so as to



be vibrated, poured, pumped, or pneumatically shot into place to form refractory shapes or structures that become rigid due to hydraulic or chemical setting effects.

### 1.4.1 Castable Bond Systems

The most widely used bonding agent in castables is Calcium Aluminate Cement (CAC), which can contain anywhere from 40 to 90 % alumina product, with the remaining component being calcium oxide. Originally, CAC are derived by melting bauxite and limestone or by sintering alumina and limestone [20]. The higher the cement purity, the greater the refractory properties of the castable. In the next section, the different hydration pathways of castables as a function of curing conditions, i.e., temperature, time, etc. will be explored.

### 1.4.2 Hydration Mechanisms of Castables

When reacted with water, the calcium alumina particles become hydroxylated and release  $\text{Ca}^{2+}$  and  $\text{Al}(\text{OH})_4^-$  ions into the pore liquid solution, followed by nucleation and precipitation of the low-solubility hydrate phases [11][21]. It is these hydrate phases that impart refractory strength to the castable's matrix components.

The final hydration state and performance of the castable structure corresponds to the uniquely generated hydrated phases. The form and stability of these phases specifically depends on the curing temperature, as provided by Table 1.3 [17][22].

**Table 1.3:** Hydration reaction series for CAC.

Anhydrous Phase		Hydrate Phase	T (°C)
6CA (calcium monoaluminate)	+ 60H →	6CAH <sub>10</sub>	≤ 10
	+ 33H →	3C <sub>2</sub> AH <sub>8</sub> + 3AH <sub>3</sub> (gel)	10-35
	+ 24H →	2C <sub>3</sub> AH <sub>6</sub> + 4AH <sub>3</sub>	≥ 35
6CA <sub>2</sub> (calcium dialuminate)	+ 78H →	6CAH <sub>10</sub> + 6AH <sub>3</sub> (gel)	≤ 10
	+ 51H →	3C <sub>2</sub> AH <sub>8</sub> + 9AH <sub>3</sub> (gel)	10-35
	+ 42H →	2C <sub>3</sub> AH <sub>6</sub> + 10AH <sub>3</sub>	≥ 35

C = CaO, A = Al<sub>2</sub>O<sub>3</sub>, H = H<sub>2</sub>O

Depending on the ambient temperature and relative humidity, there can be intermediate metastable phases e.g. CAH<sub>10</sub> and AH<sub>3</sub> (gel), which are usually converted to stable products

without inflicting any structural changes to the material, assuming well controlled curing conditions, i.e., temperature, time, humidity, etc [17]. This means that water release from the structure corresponds with higher density mineral phases, where the number and sizes of pores increases. However, the cumulative change in products e.g.  $CAH_{10}$  to  $C_3AH_6$  is not drastic at these lower temperatures and is purely a function of kinetic processes. Where at higher temperatures, there is more bond water to be released.

While the reactions shown in Table 1.3 produce stable hydrate phases at temperatures 10-35 °C, the chemical bonds lose their strength at elevated temperatures of 170-300 °C such that water is released in the form of vapour. And while CA (calcium monoaluminate) is the principle, rapidly hydrating refractory phase, its reaction kinetics is actually accelerated by the presence of a second anhydrous phase (calcium dialuminate). This latter phase is hindered by the former and therefore, the consumption of  $CA_2$  is slower and requires a longer hydration period, for a given curing temperature [21].

For instance, with a curing temperature of 10 °C (well below the acceptable value for structural stability) CA is entirely consumed by hydration only after two days of curing; however, the evolving bond system is still abundant in  $CA_2$  which is not even fully hydrated after 30 days of aging and generates transitional metastable phases (e.g. gels) that clog the pores and reduce permeability. This corresponds to the region of Figure 1.2B, where the permeability is indicated to be lower due to the lower curing temperature.

The first generation of castables were high-cement products containing anywhere from 15-30 % CAC, the so-called Regular Castables (RC). In these lower-purity formulations, the water is distributed throughout the aggregate-matrix system according to three distinct modes [23]:

- Part of the water is consumed by the grain porosity and does not contribute to chemical bonding (0-5 %).
- A large fraction of water reacts with the binder and generates the hydraulic bond (6-10 %).
- The remaining water (2-6 %) goes into forming and densification of the refractory castable. This is necessary in order to achieve an acceptable rheology.

There are several disadvantages to RC. Firstly, unreacted water (0-5 %) that has not been fully absorbed into the development of minimum green strength is immediately lost upon

heating, since this fraction of water is retained within the grain porosity of the aggregate component. As a consequence, the green strength isn't fully utilized when RC is heated.

Secondly, on heating the hydraulic bond is modified and then degraded by dehydration, where the pore size distribution and porosity considerably increases. Since the pore structure upon curing determines the green strength, an evolving pore structure will lead to structural instability and a reduction in the strength via dehydration (between 500-1000 °C).

Another problem with RC is the high lime content due to the CaO component of the CA phase, i.e., high lime content compromises the ceramic properties (lower thermal stability) of the material in cases where SiO<sub>2</sub> is present [2][23]. In the case of high Si, Fe and Na impurities, the composition will lead to the formation of a liquid-viscous phase above ceramic temperatures of 800-1000 °C, which is deleterious to both corrosion resistance and hot strength. This temperature range is specifically a function of the composition of the calcium alumina binder, i.e., the relative amount of CaO. Consequently, these drawbacks render RC inferior to high-alumina bricks, the latter of which possess better hot strength properties.

To address such challenges, a new generation of high-purity, low-cement refractory systems have emerged, the so-called Low-Cement Castables (LCC) that contain less than 2.5 wt. % CAC [23][24]. This upgrade to low- and ultralow-cement alternatives offers the advantage of lower porosity, which improves the strength properties of the material. On the other hand, permeability will also be reduced, thus heightening the risk of explosive spalling [25][26].

These more advanced systems are incorporated with various ingredients and additives as well as a whole selection of accelerators (e.g. lithium salts, hydratable aluminas, etc.) and retarders (e.g. citric and phosphoric acid) for controlling flow properties [2][20]. RC can also be formulated with retarders and accelerators. Fine and ultrafine fillers e.g. microsilica or alumina particles are applied to utilize the available intergranular voids in-between the aggregates that would otherwise be occupied by water, thereby resulting in reduced water demand [27]. Dispersants and deflocculating agents are also used to enhance flowability and dispersion of the matrix particles within the active bond system. The application of dispersion leads to a decrease in the particle surface tension, in which case less water is necessary for achieving good flow properties. Due to the improvements of density, strength, porosity and particle packing density, these new upgraded, engineered LCC systems offer

equal or superior physical properties e.g. strength, thermal shock and corrosion resistance, etc. than those of fired high-alumina bricks. Such developments have contributed to the increased production output of castables for use in the refractory lining over the decades.

To this end, non-cementitious Hydratable Alumina Binders (HAB) have also been developed (see Table 1.4) that only require adding water upon mixing to facilitate reaction with the hydratable alumina phases. It is a glassy phase that is activated by water, and through gibbsite, resulting in a structure that delivers the green tension strength. The advantage of this system is that a significant fraction of chemically bonded water is released over a wider temperature range from 100-180 °C, where vapour starts to be released at lower temperatures close to 100 °C, unlike the LCC family. Additionally, the physically deteriorating effect of lime, unique to CAC bond systems, is entirely eliminated with HAB. Microsilica gel-bonded castables, which are activated by the presence of water, are also available on the market as non-cement alternatives. Despite these gains, these lower-strength materials also pose the risk of dangerous explosive spalling around 200 °C [28][29].

**Table 1.4:** Hydration reaction for HAB.



### 1.5 First-Drying of Castables: Heating Schedules

Since castable bond systems require a liquid water addition during mixing, the finally formed, set and cured products need to be slowly pre-dried (typically 24-48 hours at less than 1 °C/min) in order to expel entrapped pore water before taking the vessels into full service, as shown in Figure 1.3. This typical heating program (ISO 1927) is slowly scaled up according to the following procedure:

- Increase from room temperature until 100 °C (first 2 hours)
- Increase from 100-200 °C (2-9 hours)
- Dwell time at 200 °C (9-14 hours)
- Increase from 200-400 °C (14-29 hours)
- Dwell time at 400 °C (29-33 hours)
- Increase from 400-800 °C (33-44 hours)
- Dwells at 800 °C

In a first-drying heating program, there are three primary dewatering stages of consideration for industrial producers: evaporation, ebullition and dehydration. Evaporation occurs from 25-100 °C (depending on the relative humidity), where the vapour pressures are too low to pose any risk of explosive spalling. Ebullition is attributed to the high pressurized steam generated by entrapped free moisture, which is released from 100-300 °C; dehydration is related to the decomposition of the hydrate phases, i.e., due to the hydraulic phases and occurs in the temperature range of 250-300 °C. However, depending on the specific hydrate structure, dehydration can also occur at lower temperatures. From a safety-control point of view, the most critical part of first heat-up corresponds to the ebullition stage and dehydration stage.

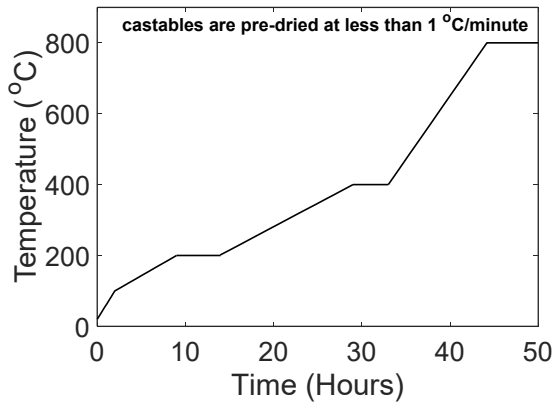


**Figure 1.3:** The prescribed temperature as a function of time for the typical first-heat up of castables before service time in industry.

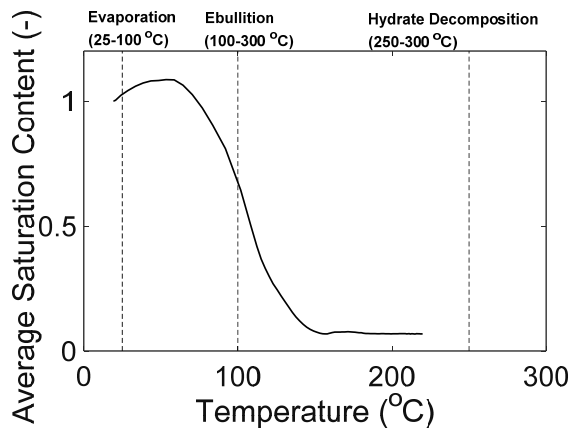


**Figure 1.4:** A plot of the average moisture content as a function of temperature for an RC sample cured for 48 hours subjected to first-drying, as measured by Nuclear Magnetic Resonance. The temperature regimes shown above correspond to the different stages of moisture release: evaporation (rapid moisture release), ebullition (vapour pressure build-up) and dehydration (decomposition of the hydrate phases).

In Figure 1.4, all three drying stages are shown in an atypical plot of the average moisture content as a function of temperature, for an RC sample cured for 48 hours. The purpose of this figure is to illustrate how the drying behavior changes from one temperature regime to another. In the early stage of evaporation, there is a minor shoulder, i.e., increase in moisture content, which corresponds to the release of metastable chemically bonded water, followed by the ebullition stage (drop in moisture content). Dehydration is most dominant at temperatures higher than that reached during the measurement.

The cautious heating rates are necessary due to generated steam pressures inside the pore network that are within a first-order approximation of the material's initial mechanical resistance (2-5 MPa), i.e., green strength. If the porous microstructure does not offer enough permeable pathways for moisture to escape, the refractory system may be compromised by dangerous explosive spalling as already shown in Figure 1.2. This violent destruction of the refractory lining can result in unwanted downtime, repair costs, energy consumption, etc.

## 1.6 Liquid-Vapour Transport

The physics of the problem of first heat-up can be understood by considering a 1D drying situation, i.e., one-sided, non-uniform heating from the exposed surface (see Figure 1.5). Once exposed to heat, large bodies of liquid water just beneath the solid surface begin to migrate toward the external atmosphere. Over time, moisture is withdrawn from deeper regions and expelled at the surface through liquid transport. Here, the rate of moisture loss is entirely limited by external boundary conditions, such as humidity, temperature or heat flux at the surface. Therefore, it is commonly referred to as *externally limited* drying.

Once the liquid clusters begin to break up, the water is locally distributed throughout the pores, where liquid transport is too slow to efficiently drive out the remaining pockets of water. At this point, the discontinuous fluid can only be transported toward the surface as

vapour, which happens through a boiling front. Thus, the rate of moisture loss depends on how fast the pressurized steam can escape from the pores; this means that vapour transport is the rate-limiting process. As vapour transport is the primary driving force, the internal pore characteristics e.g. gas permeability, have to be taken into account. Therefore, moisture loss is referred to here as *internally limited* drying.

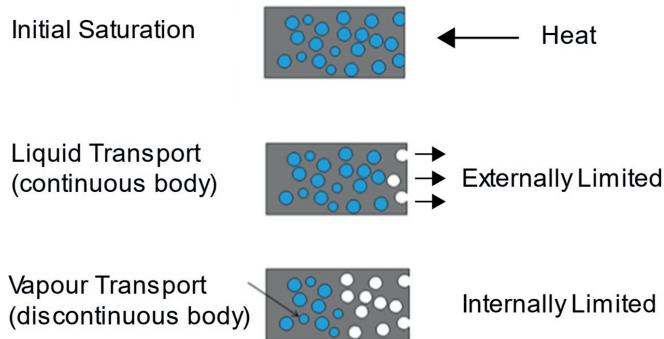


**Figure 1.5:** A diagram of the physical 1D drying process. Initially, the material pores are filled with water after freshly curing. During the externally limited period of drying, liquid transport removes water toward the surface. After the liquid clusters have broken up, the locally distributed moisture can only be transported as vapour toward the surface as high-pressure steam.

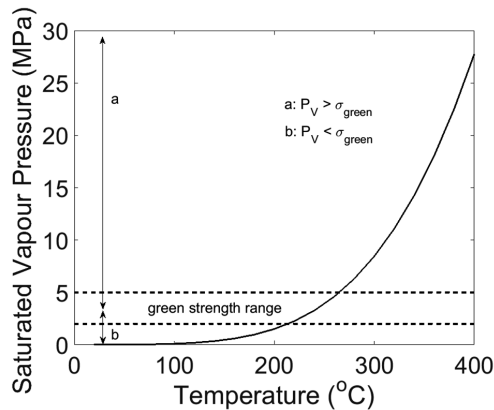


**Figure 1.6:** Plot of the saturated vapour pressure as a function of temperature. The dashed line indicates the balance between vapour pressure and range of green strength on the order of  $\sigma_{green} = 2-5$  MPa.

If we assume a closed system, i.e., a thermodynamic equilibrium, such as the case of a sealed kettle of boiling water, to a first-order approximation the vapour pressures inside the pores can be calculated on the basis of the equilibrium vapour pressure, i.e., the saturated vapour pressure. For such a closed system, the vapour pressure will be a function of temperature as shown in Figure 1.6. At room temperature, the water vapour pressure is less than atmospheric pressure. However, at 100 °C the vapour pressure will be equal to atmospheric pressure, 0.1 MPa. As can be seen by 200 °C the vapour pressure can be as high as 1 MPa and by 300 °C it will reach 10 MPa, which is well above the maximum green strength of 5 MPa, which has already been visualized in Figure 1.2 and Figure 1.6.

One main disadvantage of the LCC formulation is that physical water can only be released as highly pressurized steam above the boiling point of water, thereby approaching the strength of the material. This is due to the fact that LCC are low permeability systems, meaning that the moisture is released more slowly. Additionally, chemically combined water is decomposed above 250 °C, where the vapour pressure is already 4 MPa. This is problematic in consideration of the limitations of the green strength.

As the green tension strength of castables is on the order of 2-5 MPa, it is clear that explosive spalling is quite possible. In Figure 1.7, we have provided an example of an actual steel ladle in which the refractory lining has exploded. Based on these calculated pressures, we can see that slow drying schedules are a matter of practical concern and safety for industrial producers.



**Figure 1.7:** An example of a monolithic steel ladle bottom in which the refractory lining has exploded (steam spalling) due to an improper heat-up procedure.



While the heating rates should be chosen to be safe for dry-out, at the same time they should not be so slow that the pressure build-up is insufficient to rapidly drive out the moisture. Modern castables are designed with the intention of promoting easy escape of liquid water e.g. more permeable structures (fibers) and less water demand, once the minimum green strength has been attained, for the benefit of the refractory consumer. Otherwise, this would defeat the whole purpose of dry-out.

As provided in Table 1.3, there are various temperature regimes of stability for the hydrate phase transformation, showing that moving from one regime to the other will generate a different phase structure. This is a rough estimation of the stability range of hydrates, where at low temperatures, the hydrate state is a kinetically-driven process. However, at higher temperatures (see Table 1.5) the stabilized hydrates lose their crystal water and decompose into free water, thereby disrupting the hydraulic-refractory bond structure. Therefore, there are two main drawbacks during the drying process: (i) green strength loss incurred by degradation of the stabilized hydraulic bonds and transformation of the pore structure (at high temperatures) and (ii) build-up of steam pressure inside the pores that becomes more destructive as a consequence of (i). This drying phenomenon in (i) and (ii) is a multivariate, complicated process that depends on the behavior of the different states of water: bulk water, physical water or chemical water.

**Table 1.5:** *Temperature range of dehydration (decomposition) for various hydrate phases in castable bond systems.*

Hydrate Phases	Decomposition Temperature (°C)
CAH <sub>10</sub>	120
C <sub>2</sub> AH <sub>8</sub>	170-195
C <sub>3</sub> AH <sub>6</sub>	240-370
AH <sub>3</sub> - gibbsite	210-300
Alumina gel	100

## 1.7 The Research Goal

In the foreword to his book *Practical Refractories* (1988), J.D. Hancock wrote [1]:

*“Refractory technology is widely seen by many users as "black magic" and this is understandable as refractory application technology is not a science, but rather an engineering discipline in which the conflicting demands of an application have to be balanced against material properties. Since most of these demands are assessed qualitatively rather than quantitatively and some are unknown, it is not unusual for different solutions to be offered for the same problem according to the viewpoint and experience of the refractory technologist.”*

In the absence of a fundamental scientific understanding of castable drying, some of the leading causes of poor material performance have been identified by the industry as being due to a lack of: (i) adjustments or maintenance of the heating system and (ii) adequate training of the processing staff. Even with ultraslow heating rates lower than 30 °C/minute, mechanical failure can occur. As such, there are a few recommendations for minimizing spalling risks [11]:

- (A) Simulating the likelihood of castable steam spalling, by facilitating evaluation tests related to mass loss, temperature and pore pressure development.
- (B) Attempting to control dry-out and adjusting heat-up schedules. To this end, measurements are performed on the internal pore pressure at different lining depths and locations.
- (C) Developing drying models (implementing inputs such as permeability, thermal conductivity, etc.) for optimizing the heating curves.

So far, the only way to quantify mass transport of moisture is through indirect and destructive methods: X-ray Diffraction (XRD), Differential Scanning Calorimetry (DSC) and/or Thermal Gravimetric Analysis (TGA). Furthermore, these methods are limited by the information they can provide, e.g. after crushing sample to small pieces, non-local information, etc. Much knowledge is to be gained from measuring the spatially resolved moisture distribution, i.e., local information, which provides direct access to parameters involved in important endothermic transformations (e.g. speed of the boiling front, dehydration, etc.) as a function

of material characteristics (e.g. permeability) and inputs (e.g. binder content and additives). Such direct information is non-observable with conventional measuring techniques and thus poses a serious challenge to optimizing heating curves for pre-drying schedules. Until a suitable alternative is offered for quantifying moisture loss, refractory science will continue to be paralyzed by the subjective limitations elucidated by J.D. Hancock.

This gap in knowledge has presented some research challenges to refractory science. Some of the questions that arise in this challenge are the following:

- Effect of chemically bonded water vs. physically free water on the dry-out behavior in terms of boiling front temperature and pressure development.
- The physical processes that determine the boiling front temperature when adjusting material selection.
- Drying behavior (boiling front temperature and pressure) as a function of changing permeability.

The goal of this study is to relate the drying behavior of various materials, to their physical and chemical properties, e.g. permeability, fiber content, water demand, etc. in such a way that can be used to validate a more fundamental understanding of 1D moisture and heat transport. For this thesis, the research undertaken focuses specifically on monolithic castables composed of high-alumina bond systems.

Additionally, it has been shown that there are a number of critical control parameters when preparing these materials that can affect the dry-out behavior. Since castable properties are a complex function of various different inputs, e.g. raw components, binder, water demand, additives, etc. we have chosen a variety of castables to test.

On the basis of this comparative-quantitative analysis, differences in the drying behavior should be identified (e.g. front speed, temperature, pressure) and cross-referenced with different material families (in terms of material properties e.g. pore structure, ingredients, etc.) and furthermore serve as a practical roadmap for pre-drying schedules.

To this end, a high-temperature Nuclear Magnetic Resonance (NMR) setup is proposed as an alternative technique for investigating the moisture distribution during a 1D first-drying heating experiment. As NMR is a resonance tool commonly used in medical imaging applications, the probe can be tuned to the frequency of hydrogen nuclei, i.e., moisture,

thereby allowing direct, continuous and non-destructive observation of the spatial distribution of moisture. At the same time, the temperature distribution can also be measured alongside the NMR moisture profiles. Therefore, it is possible to directly and simultaneously observe the mass and heat transport throughout a first-drying experiment with this setup.

### **1.8 Outline of Thesis**

Here we have presented the industrial and scientific challenge for the first-drying of castables, showing how various moisture and heat transport processes are involved in controlling dry-out in terms of externally and internally limited drying. From the industrial side, castables are perceived as a kind of “black magic” where fundamental transport processes are not quantifiable. In this thesis, we argue that the industrial and scientific sphere of knowledge can be reconciled through a specialized high-temperature NMR setup that can directly measure and quantify these transport processes.

As a starting model material, we introduce a high-water demand Regular Castable for demonstrating the capability of our high-temperature Nuclear Magnetic Resonance setup. This material is rich in water and quite porous, thus providing a good opportunity for calibrating the setup in Chapter 2.

In chapter 3, we will present a whole survey of various castable materials which differ in their formulation properties: water demand, binder content and fines. The moisture and temperature profiles will be shown and analyzed to investigate the differences in the drying behavior between the various materials. To gain a more conceptual understanding of the experimental data, a simple vapour transport model will also be introduced to account for the differences in drying behavior.

In chapter 4, the effect of fiber-addition and a permeability enhancing active compound (MIPORE) on dry-out behavior will be investigated since in the preceding chapters the experiments were done with a formulation in which fibers were already added to all of the materials. Removing the fibers or MIPORE will allow us to quantify the development of a boiling front and how it affects the moisture release.

The research subject of the thesis deals with the drying of castables. From a scientific point of view, it is interesting to compare the drying of castables under similar heating conditions

with the drying of another porous material, which in this case is wood. This will be the subject of chapter 5.

In chapter 6, we will review the final results and present the conclusions and outlook of the thesis, the main findings and what the implications and constraints are for future work into the first-drying of castables.

## 1.9 References

- [1] J.D. Hancock, *Practical Refractories*. West Yorkshire, Hensman Graphics/Cartworth Industries, 1988.
- [2] W.E. Lee, W. Vieira, S. Zhang, K.G. Ahari, H. Sarpoolaky and C. Parr, "Castable refractory concretes," *International Materials Reviews*, vol. 46, no. 3, pp. 145-167, 2001.
- [3] W.E. Lee and R.E. Moore, "Evolution of in Situ Refractories in the 20th Century," *Journal of the American Ceramic Society*, vol. 81, no. 6, pp. 1385-1410, 1998.
- [4] D. A. Brosnan, "Alumina-Silica Brick," in *Refractories Handbook*. Marcel Dekker, Inc., 2004, p. 80.
- [5] S. Banerjee, "Properties of Refractories," in *Refractories Handbook*. Marcel Dekker, Inc., 2004, pp. 1-4.
- [6] World Steel Association, "Press Release: July 2017 crude steel production for the 67 countries," 2017.
- [7] A. Baaske, R. Fandrich, J. Pischke, P. Quirnbach, J. Rzepczyk and L. Schottler, "Refractory Products - the TC Refractories Perspective," in *Refractories Worldforum*, Baden-Baden, pp. 15-23, 2017.
- [8] W. D. Callister, *Fundamentals of Materials Science and Engineering: An Integrated Approach*, Second ed. J. W. & Sons, 2005.
- [9] L. Krietz, "Refractory Castables," in *Refractories Handbook*. Marcel Dekker, Inc., 2004, pp. 259-262.
- [10] R. Krebs, "Unshaped Refractory Products," in *Refractories Handbook*. Marcel Dekker, Inc., 2004, pp. 287-289.
- [11] A. P. da Luz, M. A. L. Braulio and V. C. Pandolfelli, *Refractory Castable Engineering*. Baden-Baden & Karlsruhe: Federation for International Refractory Research and Education & Goller Verlag, 2015.

- [12] D. Schmidtmeier, A. Buhr, G. Wams, S. Kuiper, S. Klaus, F. Gotz-Neunhofer, D. Zacherl and J. Dutton, "Cement Hydration and Strength Development- How Can Reproducible Results be Achieved?," in *Proceedings of the Unified International Technical Conference on Refractories*, Victoria, British Columbia, Canada, pp. 1057-1060 2013.
- [13] R. Salomao and V. C. Pandolfelli, "Drying Behavior of Polymeric Fiber-Containing Refractory Castables," *Journal of the Technical Association of Refractories (Japan)*, vol. 24, no.2, pp. 83-87, 2004.
- [14] C.M. Peret, R. Salomão and V.C. Pandolfelli, "Polymeric Fibers as Additives for the Drying of Refractory Castables," *Journal of the Technical Association of Refractories (Japan)*, vol. 24, no. 2, pp. 88-92, 2004.
- [15] M.D.M. Innocentini, C. Ribeiro, R. Salomao, V.C. Pandolfelli and L.R.M. Bittencourt, "Assessment of Mass Loss and Permeability Changes during the Dewatering Process of Refractory Castables Containing Polypropylene Fibers," *Journal of the American Ceramic Society*, vol. 85, no. 8, pp. 2110-2112, 2002.
- [16] R. Salomao and V.C. Pandolfelli, "Polypropylene Fibers and their Effect on Processing Refractory Castables," *International Journal of Applied Ceramic Technology*, vol. 4, no. 6, pp. 496-502, 2007.
- [17] F.A. Cardoso, M.D.M. Innocentini, M.M. Akiyoshi and V.C. Pandolfelli, "Effect of curing time on the properties of CAC bonded refractory castables," *Journal of the European Ceramic Society*, vol. 24, no. 7, pp. 2073-2078, 2004.
- [18] F.A. Cardoso, M.D.M. Innocentini, M.F.S. Miranda, F.A.O. Valenzuela and V.C. Pandolfelli, "Drying behavior of hydratable alumina-bonded refractory castables," *Journal of the European Ceramic Society*, vol. 24, no.5, pp. 797-802, 2004.
- [19] M.D.M. Innocentini, M.F.S. Miranda, F.A. Cardoso and V.C. Pandolfelli, "Vaporization Processes and Pressure Buildup during Dewatering of Dense Refractory Castables," *Journal of the American Ceramic Society*, vol. 86, no. 9, pp. 1500–1503, 2003.

- [20] P. Pilate, J. Tirlocq and F. Cambier, "Refractory Castables: an Overview," *Process Engineering*, vol. 84, no. 6, pp. 43-49, 2007.
- [21] C. Parr, "Calcium Aluminate Cement- What Happens When Things Go Wrong?," in *Proceedings of the Institute of Refractories Engineers Annual Conference*, Rotherham, United Kingdom, pp. 1-11, 2008.
- [22] J. Spink, "A review of explosive spalling of castable materials," *The Refractories Engineer*, pp. 13-17, January 2014.
- [23] B. Clavaud, J.P. Kiehl and R.D. Schmidt-Whitley, "15 Years of Low Cement Castables in Steelmaking," in *International Conference on Refractories*, Tokyo, Japan, pp. 589-606, 1983.
- [24] T. Eguchi, I. Takita, J. Yoshitomi, S. Kiritani and M. Sato, "Low-Cement-Bonded Castable Refractories," *Taikabutsu Overseas*, vol. 9, no. 1, pp. 10-25, 1989.
- [25] C. Wohrmeyer, C. Parr, J.M. Auvray, M. Lievin and E. Frier, "The Impact of Hydration and Dehydration Conditions on the Permeability of LCC Systems," in *Proceedings of the Unified International Technical Conference on Refractories*, Dresden, Germany, pp. 536-539, 2007.
- [26] E. Karadeniz, C. Gurcan, S. Ozgen and S. Aydin, "Properties of Alumina Based Low-Cement Self Flowing Castable Refractories," *Journal of the European Ceramic Society*, vol. 27, no. 2-3, pp. 1849-1853, 2007.
- [27] R. Kockegey-Lorenz, A. Buhr, D. Zacherl, B. Long, S. Hayashi and J. Dutton, "Review of Matrix Aluminas for Refractory Formulations," in *Proceedings of the Unified International Technical Conference on Refractories*, Kyoto, Japan, 2011.
- [28] W. Mista and J. Wrzyszczyk, "Rehydration of Transition Aluminas Obtained by Flash Calcination of Gibbsite," *Thermochimica Acta*, vol. 331, no. 1, pp. 67-72, 1999.
- [29] B. Myhre, "Microsilica-gel bond castables for rapid heat-up," in *RCD 48th Annual Symposium*, St Louis, USA, 2012.



---

## Chapter 2: High-Temperature Nuclear Magnetic Resonance (NMR)

---

### Abstract

In this study a specialized high-temperature NMR setup is presented for measuring free moisture in monolithic refractory castables during one-sided heating (100-300 °C). This setup makes use of a high thermal-stability Birdcage-coil for measuring the quantitative moisture content at high-temperatures, while also utilizing a mini-coil for calibrating transverse relaxation changes, as a function of temperature and hydration state, taking place in the sample throughout a drying experiment. We employ a high-temperature correction scheme that calibrates the effects of rising temperatures on the NMR signal. With this configuration, we can non-destructively measure moisture and temperature profiles continuously and achieve a spatial resolution of 2-3 mm for samples as long as 74 mm. After applying the NMR correction, we can extract information about the physical and chemical components of water as they are released from the porous matrix during first heat up. As a model material, we demonstrate the capability of our setup with a conventional castable after it has been cast and cured for 48 hours.

*This chapter has been adapted from Barakat, A.J., Pel, L. & Adan, O.C.G., Appl. Magn. Reson. (2018) 49: 739.*

## 2.1 Introduction

In steel and iron processing plants, the hot ladles where these metals are transported must be lined with refractories. These materials are capable of withstanding physical, thermal and chemical stresses and strains over a wide range of temperatures [1][2]. In contrast to brick (shaped refractories), the installation and maintenance of unshaped monolithic refractories (i.e., castables) require less labour costs and fewer repairs since they have a longer service lifetime. It is for this reason that monolithics (of which castables constitute half of production output) make up more than twice the production level of bricks in Japan, for instance [3].

However, prior to installation, the refractory elements must be slowly pre-dried at less than 1 °C/minute for at least 24 hours to temperatures higher than 500 °C, in order to remove the free and chemically bound water components from the porous matrix.

The conservative heating rates are necessary due to generated steam pressures within the pores that soar rapidly beyond the mechanical strength of the material (2-6 MPa), sometimes causing physical destruction via explosive spalling. While these drying temperatures are quite high for laboratory measurements, it is known that the heightened risk of spalling is actually found in both the dangerous so-called ebullition stage (100-300 °C) and hydrate decomposition stage (250-300 °C). In fact, damage can actually occur at these relatively low temperatures. Therefore, a quantitative understanding of the transport dynamics in the regime of first-drying (100-300 °C) is paramount to optimizing the durability and lifetime of these materials for industrial applications. With current global steel production output exceeding 1000 million tons per year [4], there is great urgency for improving the design and performance of castables. Therefore, increasing the heating rate, altering the drying behavior through control of material inputs and minimizing service failure is of great economic concern for industrial producers.

In order to assess the potential of spalling, indirect and destructive methods are often employed to characterize the phase morphology (XRD), dehydration and mass loss of water (TGA/DSC). Unfortunately, all of these methods suffer from limitations on information that can be obtained due to inadequate sample size (preventing development of a thermal gradient) or sample destruction (i.e., by crushing to grains/powder). Evermore, measuring the mass loss over time only provides information about the total moisture content, without providing any direct observation of the spatially resolved moisture distribution. More importantly, crucial information for calculating transport properties, such as the speed and

position of the drying front, as well as the corresponding vapour pressure, is completely lost on such conventional experimental methods. While the use of neutron and X-ray radiography can also provide information about the moisture distribution, these techniques are limited by the maximum sample size, boundary artifacts and inability to distinguish between the different components of water [5].

Modelling the transport dynamics is another alternative for quantifying the moisture distribution, but this relies on either second-guessing the behavior of drying (e.g. advection vs. diffusion) or introducing simplifying assumptions (e.g. single phase vs. multiphase phenomena) into the underlying theory [6][7].

In light of these constraints, a new experimental approach is in order that incorporates the need for direct, non-destructive and continuous measurement of the moisture and temperature distribution throughout a first-drying experiment. The goal of this study is to demonstrate that the quantitative moisture content can be directly measured by Nuclear Magnetic Resonance (NMR) and is related to the drying behavior for high-temperatures without compromising the sample.

Previous work on quantifying moisture loss with NMR focused on materials (e.g. concrete) that have already aged for one full year [8]. At this point curing conditions become less determinate of pore structure, which is almost fixed in time for low temperatures. In practice, however, castables must be freshly cured, pre-dried and then immediately installed for service. Therefore, unlike concrete, the castable pore structure is continuously developing and changing, starting at room temperature until 100 °C [9]. As a result we had to perform a correction of the signal for both the temperature and the pore-size development based on the measured  $T_2$ . Furthermore, castables are suitable materials to study under NMR as their composition is abundant in aluminum oxide, thereby containing very little paramagnetic impurities (e.g. iron oxide).

In the next section, we will present the outline for an experimental NMR setup which is capable of performing quantitative moisture content measurements at high temperatures on a sample material. To this end, we use conventional castables (CC) that can be formulated in the lab and scanned inside the NMR insert for continuous periods of time. The temperature calibration of the NMR signal will also be presented and discussed at length.

## 2.2 Experimental Setup

A home-built NMR setup was used for performing one-sided, non-isothermal first-drying experiments on conventional castables. In order to perform these measurements we use the main magnetic field of a whole-body MRI scanner. A schematic view of the setup is presented in Figure 2.1. The experiments are conducted inside a Philips whole-body 1.5 T magnet (INTERA). The samples are cast into 8 cm-diameter cylindrical Teflon moulds (preventing moisture loss, with exception to the front face which remains open to heating) and additionally isolated with 5 cm thick and 8 cm long rock wool in the same manner to prevent heat loss during an experiment. In this way, we can simulate one-dimensional heating (as in a real world setting) allowing for the development of a moderate temperature gradient in one direction.

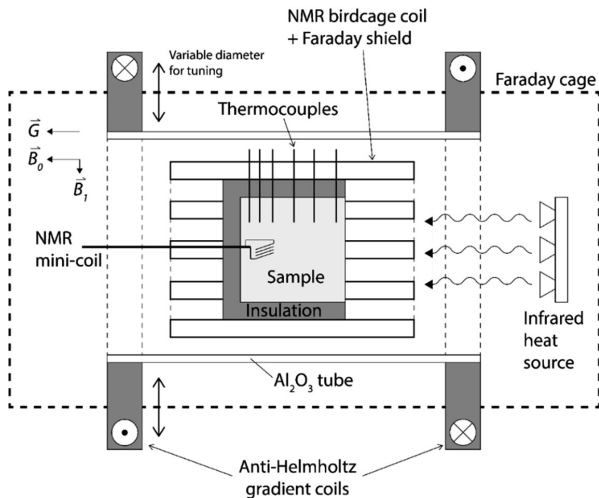


**Figure 2.1:** Schematic view of the high-temperature NMR setup. The birdcage coil is enclosed by a pair of anti-Helmholtz gradient coils with a calibrated strength of 80 mT/m and a Faraday cage for tuning and matching. The heat source is provided by an array of seven halogen lamps.

As we aim to perform quantitative measurements over the full temperature range up to 300 °C, special attention was given to the design of the birdcage coil. Here we make use of a home-built low-pass 64 MHz RF homogeneous birdcage resonator for conducting pulsed measurements. The birdcage is built around an Al<sub>2</sub>O<sub>3</sub> tube capable of withstanding high temperatures, without introducing a background signal to the NMR. A schematic diagram of the birdcage used in these experiments is presented in Figure 2.2. In order to make sure the birdcage does not detune excessively during the measurements, as both the temperature and

moisture content are changing, we added a shielding coil between the sample and RF birdcage coil. This coil consists of electrically grounded and interconnected conducting segments running parallel to the legs of the birdcage resonator [10] (also see Figure 2.1 and 2.2). On one side these are connected to the ground to prevent as much as possible any dielectric variations, due to the changing moisture content. In addition, the other side of the legs are interconnected through a small resistance ( $1\text{ k}\Omega$ ), which means that this coil will also act as a load, decreasing the quality factor  $Q$  of the LC-circuit to about 40. In combination with the low filling factor, this makes the system capable of performing quantitative measurements of the mass loss.

The birdcage itself is enclosed by a second shield composed of a copper mesh. The function of this shield is two-fold: protecting the MRI magnet in case of an explosion from the sample and tuning the resonance frequency of the birdcage by changing the diameter of the shield. The resonator is related to the spectrometer through an inductive coupling loop opposing the conducting segments of the probe. With this current setup we are able to generate a Hahn spin-echo with a pulse time of  $50\text{ }\mu\text{s}$  using a  $4\text{ kW}$  homebuilt power amplifier. The shortest echo time we can achieve is  $300\text{ }\mu\text{s}$ . For such a sequence, a block-shaped pulse is employed for exciting the sample protons.

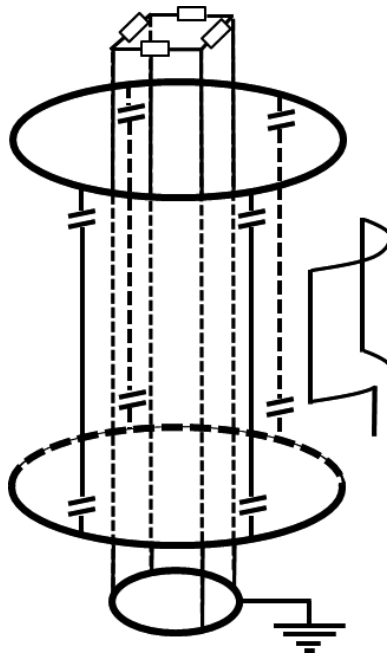


**Figure 2.2:** *A schematic diagram of the home-built low-pass birdcage. The conducting segments of the birdcage are excited by an inductive coupling loop. A shielding coil between the sample and RF Birdcage coil is inserted to prevent detuning, in order to minimize the effect of dielectric variations. The other side of the legs are interconnected through a small resistance (1 k $\Omega$ ), effectively acting as a load to decrease the  $Q$  of the LC-circuit to about 40.*

In order to perform profile measurements, two anti-Helmholtz magnetic field gradient coils are used with a maximum strength of 80 mT/m. With this maximum gradient, we can achieve a one-dimensional resolution on the order of 2-3 mm for the castables considered. With 25 slices, a single-slice excitation imaging technique is used in conjunction with the Hahn pulse sequence described above for measuring one-dimensional profiles. As the bandwidth of the insert is 250-300 kHz, the moisture profile is measured by changing the resonance frequency, i.e., during our experiment we do not switch the gradient. Furthermore, because the castable's  $T_1$  is on the order of a few tens of milliseconds, using a Hahn spin echo excitation scheme allows for measuring a complete profile over 100 mm within 5-10 minutes.

In order to get a better idea of how the relaxation time of our sample is changing with time, a solenoidal mini-coil of 10 mm in diameter was added to the back of each sample (which is accomplished by casting). The details of this installation procedure are explained more precisely in section 2.4.1. Due to the significantly smaller scanning volume (of the mini-coil) and greater filling factor (10-fold greater than the birdcage coil), a better signal-to-noise ratio enabling faster measuring time was achieved. Furthermore, with such a tiny probe in place, a short echo time of 110  $\mu$ s is achieved that allows us to measure the shorter  $T_2$  components as a function of temperature. The gathered  $T_2$  data is used for calibrating the temperature effect at every slice of the sample. Since the samples are homogeneous, performing a CPMG measurement at every slice is not necessary. A practical advantage of this approach is that it allows positioning the coil perpendicular to the main field, ensuring a 90° rotation of the spins regardless of the orientation of the sample. It was found that this mini-coil had almost no effect on the performance of the main birdcage.

When casting materials, the samples are punctured with holes accommodating thermocouple placement for temperature profile measurements, which are also necessary for correcting the temperature effects on the NMR signal. Using a template scale, 6 thermocouples are non-linearly fixed into the sample holder, starting from front to back: 7, 27, 44, 56, 64 and 71 mm. The RF mini-coil is located at the same position as the last thermocouple (71 mm). The heat source for the experiments is provided by an array of seven gold-coated halogen lamps facing

the front of the sample (with a corresponding heat flux on the order of 3.5 kW/m<sup>2</sup> and a dissipated power of 100 W per lamp). The maximum heating rate was found to be on the order of 1-2 °C/min in the present setup.

## 2.3 NMR signal temperature dependence

### 2.3.1 Temperature influence

In a high-temperature NMR experiment, the temperature will have a profound effect on both the relaxation and the magnetization. In which case, the standard expression for the magnetization must be rewritten as:

$$M(t_E, t_R, T) = M_0(T) \exp\left(-\frac{t_E}{T_2(T)}\right) \left[1 - \exp\left(-\frac{t_R}{T_1(T)}\right)\right]. \quad (2.1)$$

Above  $M$  is the time-dependent magnetization,  $t_E$  the Hahn spin-echo time,  $t_R$  the repetition time and  $T_1$  and  $T_2$  correspond to longitudinal and transverse relaxation, respectively. The equilibrium magnetization  $M_0$  will scale inversely proportional to the absolute temperature  $T$  of the field as given by the well-known Curie law [11]:

$$M_0(T) = \frac{N\mu\hbar\gamma B_0}{2kT}, \quad (2.2)$$

where  $N$  is the number of nuclei,  $\mu$  the magnetic moment,  $\hbar$  the Planck constant,  $\gamma$  the gyromagnetic ratio,  $B_0$  the magnetic field and  $k$  the Boltzmann constant.

In Figure 2.3 we have provided the results for a measurement of the signal of water as a function of temperature by heating a small container of water up to the boiling point, inside our experimental setup. As can be seen, the relationship between the signal and reciprocal temperature is linear, in accordance with the Curie law.

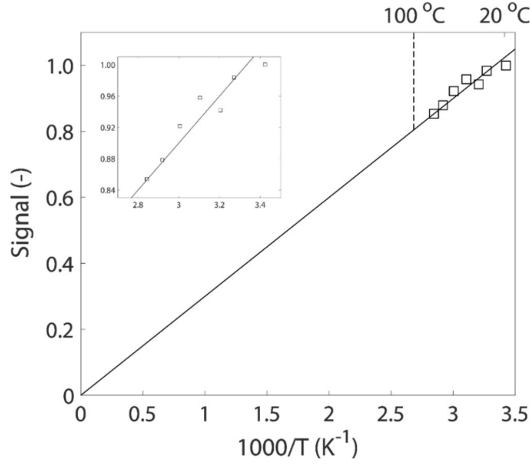


**Figure 2.3:** The measured NMR signal amplitude of water as a function of reciprocal temperature. The straight line demonstrates the Curie-law from 20-100 °C.

By partially differentiating the logarithm of the magnetization with respect to temperature, we can decompose the separate effects of various mechanisms on the temperature-dependence of the measured signal [12]:

$$\frac{\partial \ln M(t_E, t_R, T)}{\partial T} = \frac{\partial \ln M_0}{\partial T} + \frac{t_E}{T_2^2(T)} \frac{\partial T_2(T)}{\partial T} - \frac{t_R}{T_1^2(T)} \frac{\exp\left(-\frac{t_R}{T_1(T)}\right)}{1 - \exp\left(-\frac{t_R}{T_1(T)}\right)} \frac{\partial T_1(T)}{\partial T}. \quad (2.3)$$

Here we see the main contributions to the temperature dependence are due to magnetization and  $T_1$  and  $T_2$  relaxation. If we set  $t_R \gg T_1$  in our experiments, we can then neglect the  $T_1$  dependence to get:

$$\frac{\partial \ln M(t_E, t_R, T)}{\partial T} \approx \frac{\partial \ln M_0}{\partial T} + \frac{t_E}{T_2^2(T)} \frac{\partial T_2(T)}{\partial T}. \quad (2.4)$$

Hence we see that the temperature correction is a function of both the echo-time and the spin-spin relaxation time of our sample. Hence for a fixed  $t_E$  any change in  $T_2$  will result in a change of the NMR signal.



### 2.3.2 Relaxation correction

During an NMR experiment, the water molecules in a porous material will diffusively probe the pore space over a certain amount of time. As a result, relaxation will be dependent on the pore geometries and spin-spin relaxation can be described in the fast diffusion regime according to the well-known Brownstein-Tarr model (1979), i.e:

$$\frac{1}{T_2} = \frac{1}{T_{2,Bulk}} + \rho_2 \frac{S}{V}, \quad (2.5)$$

where  $\rho_2$  is the surface relaxivity,  $S/V$  the surface-to-volume ratio and  $T_{2,bulk}$  the bulk relaxation for water. In most conventional castables the pores are in the range of 10-100 nm. In this length scale,  $T_2$  relaxation will consequently be dominated by surface relaxation. Accordingly, we can neglect the contribution of bulk relaxation. For comparison, gypsum has a pore-size distribution on the order of 1  $\mu\text{m}$  and will therefore be dominated by slow-diffusion in the pores [13].

In our drying experiments, the relaxation will change due to the transforming pore-size distribution as the materials are hydrating. Furthermore, the temperature-dependence of the surface relaxivity will also cause the relaxation to change. The latter effect can be phenomenologically described by an Arrhenius-type equation [14][15]:

$$\rho_2 = \rho_{2,0} \exp\left(\frac{\Delta E}{RT}\right). \quad (2.6)$$

Here  $\rho_{2,0}$  is the surface relaxivity at a certain reference temperature, and  $\Delta E$  is an effective surface interaction energy. The surface interaction energy is a combination of both the energies involved in surface relaxation and surface diffusion [14].

In Figure 2.4 the measured relaxation times as a function of reciprocal temperature are demonstrated for two castables of different hydration time and an aluminum oxide reference material. As can be seen, the initial increase of the relaxation times can be described by an Arrhenius equation. From these measurements we find that in the case of castables  $\Delta E = 4\text{-}5$  kJ/mol, which is of the same order as previously found for concrete  $\Delta E = 1\text{-}5$  kJ/mol [15]. Here it has to be taken into account that for castables  $T_2$  will not only be a function of the temperature but also the hydration state, since the pore structure is not chemically inert with temperature.

The metastable hydrate phases are changing from room temperature until the boiling point of water, thereby redefining the structure of the solid network. However, around the boiling point, the molecules experience a phase change from liquid to vapour, followed by evacuation from the pores and a corresponding decrease in  $T_2$  as can be seen in Figure 2.4A and B. It is also at this point that  $T_2$  spikes to a maximum value for a short time before the moisture evaporates. The moisture at this juncture is relaxing slower than it was before being heated. The exact cause for this spiking behavior is not fully understood at the moment. One possible reason is that heated moisture is less bound to the confined geometry of the pores, which is likely since in this temperature range the porosity may also change and the viscosity is significantly lower than before (30 % of the initial value at room temperature). In Figure 2.4B we have also plotted the corresponding CPMG amplitude as a function of temperature. As can also be seen at this point, around 100 °C, the CPMG amplitude temporarily levels off as  $T_2 \rightarrow T_{2,max}$ . Furthermore, between the temperatures 90-100 °C,  $T_2$  is clearly increasing to a maximum value while the corresponding CPMG amplitude is decreasing. This suggests that in the fast-diffusion regime, either the surface relaxivity or surface area of the pore must be simultaneously changing along with the volume fraction of moisture.

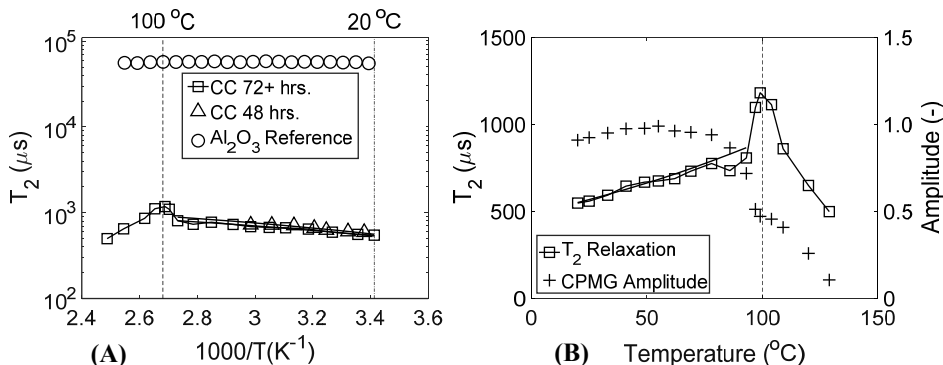


**Figure 2.4:** (A) The  $T_2$  as measured with the mini-coil plotted as a function of reciprocal temperature for conventional castables cured for 48 and 72 hours, along with an aluminum oxide reference sample. The straight lines are a fit of the Arrhenius temperature-dependence. (B) The  $T_2$  measured for conventional castables cured for 72 hours from (A) plotted against a normal temperature scale. The straight line is a fit to the Arrhenius temperature-dependence as given in (A). The corresponding CPMG amplitude in relation to  $T_2$  is also plotted in the same figure.

Furthermore, the spontaneous jump in  $T_2$  cannot be attributed to just free water relaxing in the pores. To test this hypothesis, a chemically inert reference sample, i.e., aluminum oxide, with

a uniform pore size distribution (on the order of 200 nm) was taken and capillary saturated for 24 hours, before being heated under a heating program similar to the one used in the experiments considered here as shown in Figure 2.4A. The results yielded a constant  $T_2$  with respect to temperature well above 100 °C. Therefore, it is probable that a chemical/or structural change is occurring in the castable's porous network as the hydrates are transforming into more stable products in the higher temperature regime of 90-100 °C.

### 2.3.3 Overall Temperature Correction

In an isothermal NMR experiment the water signal in a porous medium will decay multi-exponentially, reflecting the different pore states, i.e.,  $T_2$  components of the system:

$$M(t) = \sum_i m_i \exp\left(-\frac{t}{T_{2,i}}\right). \quad (2.7)$$

To obtain the total quantitative moisture content for a temperature induced drying experiment, the total NMR signal should incorporate effects from the magnetization as a function of temperature, and relaxation as a function of both the temperature and hydration. In conjunction with Eq. (2.1) we get:

$$M(t, T) = \sum_i (A_c(T) m_i) A_i(T) \exp\left(-\frac{t}{T_{2,i}(T)}\right). \quad (2.8)$$

Above,  $A_i$  and  $A_c$  correspond to temperature correction for both the Arrhenius and Curie law, respectively, and  $m_i$  is the signal amplitude for the  $i$ th pore system. For castables, the  $T_2$  correction is dependent on both temperature and hydration, which requires measuring  $T_2$  as a function of temperature and hydration for every profile. Accordingly, the measured temperature profiles based on the 6 thermocouples are furthermore interpolated for a greater number of points that will supply the correction function.

As an example, in Figure 2.5A we have shown the correction to the Curie law and  $T_2$ , along with the total correction for the signal. Furthermore, the correction to the Curie law is independent of the material's properties, whereas the  $T_2$  correction depends on the temperature and pore structure.

As can be seen for the total correction of both the magnetization and relaxation, the maximum correction (i.e., highest temperature) for the shortest  $T_2$  components is just 20 %. The maximum total correction, including both relaxation and magnetization, at the highest temperatures will be 25-30 %.

As an example, in Figure 2.5B, we have plotted the uncorrected saturation for some selected profiles along with the total corrected profiles, i.e., for both temperature and hydration. Saturation is the raw data normalized to the first isothermal profile. The profiles illustrate that, as alluded to in the previous paragraph, the total correction to the degree of saturation is no more than 30 %.

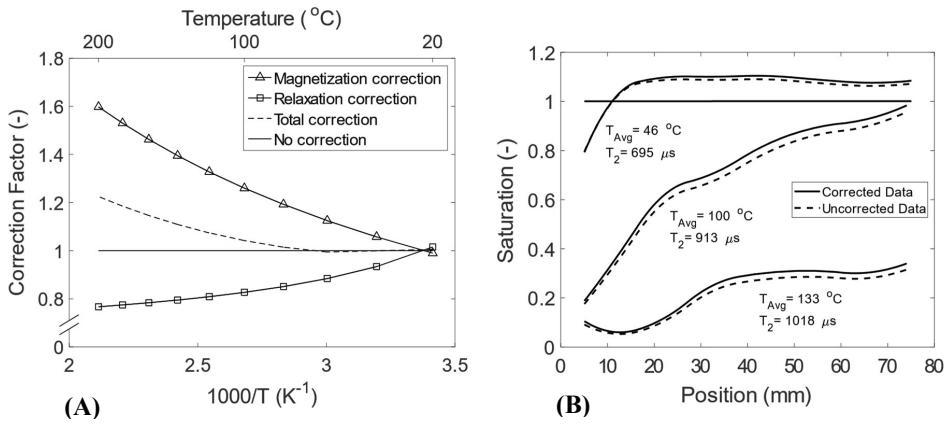


**Figure 2.5:** (A) Total temperature correction of the NMR signal for a sample cured for 48 hours. The contributions from both the relaxation and magnetization effects are included. The solid line corresponds to no correction to the signal. (B) Selected moisture profiles (raw uncorrected + corrected) for an experiment with Conventional Castables cured for 48 hours plotted next to each other. The corrected profiles are a sum of all different terms: magnetization (temperature) and relaxation (temperature, hydration state). The relaxation value is changing with every profile.

It is important to note that the correction only applies to the wet part of the sample, which is the fraction of pore space that is still saturated with liquid water. As the  $T_2$  calibration line corresponds to the relaxation dynamics of a saturated pore from  $T = 20$ - $100$  °C and since the signal drops to values below 10 % in the vapour region, the dry part of the sample does not significantly affect the relaxation correction. Indeed it can be seen from Figure 2.5B that the correction to the profiles in the front part of the sample is almost identical to the uncorrected profiles within the same region.

## **2.4 First drying of castables**

### **2.4.1 Sample Preparation**

The chosen sample for this study was a freshly prepared conventional castable cured for 48 hours at room temperature. This particular curing time was chosen since it provides sufficient time for the calcium alumina binder to consume the water. The pre-mix is composed of tabular alumina (TA) grains which range in size from the micrometer to millimeter range. The pre-mix and binder constitute the total dry formulation (80/20 % by mass), where the water demand is approximately 9 % by mass (dry basis). The samples are dry mixed for 1 minute and wet mixed for 4 minutes with a Hobart mixer, then subjected to mechanical vibration in order to achieve optimum densification of the porous matrix. The mixing time is fixed in order to ensure homogenisation and dispersion of water throughout the solid skeleton. After the samples have been vibrated, they are cast into 8 cm x 8 cm cylindrical Teflon moulds and covered overnight. The samples are 7.4 cm in length and 7.4 cm in diameter.

Furthermore, the solenoidal RF mini-coil is casted into the sample at the center, back-end. This means that the coil is initially fixed inside the mould, where fresh material is directly poured into it, i.e., during the wet phase when the material hardens into and around the coil. After 48 hours have passed, the coil is rigidly secured for performing high-temperature NMR measurements.

### **2.4.2 Moisture Content during First-Drying**

In Figure 2.6, the results of the heating experiment are shown. Due to the sample length, the timescale of the experiment is around 1.5 hours, after which there is no remaining signal. The temperature profiles were measured simultaneously along with the saturation profiles, with an average time of 3-4 minutes in between profiles. The temperature profiles reflect the conventional method of measuring heat transport during a first-drying experiment, where only superficial information is obtainable such as the temperature gradient and beginning of the boiling front. Figure 2.6C reveals that the boiling front begins around 100 °C, corresponding to the increase in energy intake of the sample.

Along with the temperature profiles, the saturation profiles are simultaneously measured and plotted in Figure 2.6A. The saturation profiles are generated by taking every raw profile and dividing it by a reference taken at the beginning of the experiment, prior to switching on the heat. This allows for eliminating inhomogeneities that may arise from the field. Depending

on the number of averages used to improve the signal-to-noise ratio, the time between each profile is 3-4 minutes. The maximum surface temperature reached is around 180-200 °C. Beyond this temperature, there is no remaining NMR signal.

Initially upon heating, we observe a slight increase in the total moisture content by about 5 % (i.e., a minor shoulder at 20 minutes). This reflects the fact that the shortest components of chemically combined water can be released from the hydrated state (the CPMG amplitude also increases in this range), even after correcting the signal for temperature effects. This transformation is not complete (i.e., towards the more stable crystallized gibbsite  $\text{Al}_2\text{O}_3 \cdot 3\text{H}_2\text{O}$ ) until 110 °C, as shown by the  $T_2$  data (i.e., where it rapidly drops off around 120 °C), noted in the earlier discussion. However, the most pronounced observation in the drying behavior is displayed by the inhomogeneous moisture distribution almost immediately after initial heat-up as shown in Figure 2.6. In this next stage, there is only drying at the top part of the sample. The moisture is then driven out very rapidly until about 50 minutes have passed, corresponding to the second stage of drying. These first-two stages of moisture loss fall into the *externally limited* period of drying, where ambient conditions, such as temperature and humidity, determine the speed of drying.

However, after about 50 % of the total moisture content has been removed from the sample, the drying front develops and slowly penetrates the pores (indicated by the markers in Figure 2.6A and 2.6C). This slower stage of drying is known as the *internally limited* period and is governed by internal transport processes that reflect the pore structure and material characteristics of the sample, e.g. the ebullition and dehydration stages. The *critical moisture* content is defined as the boundary separating these characteristic stages of drying. It is only for quantities below the critical moisture content that the drying front emerges and travels through the sample.

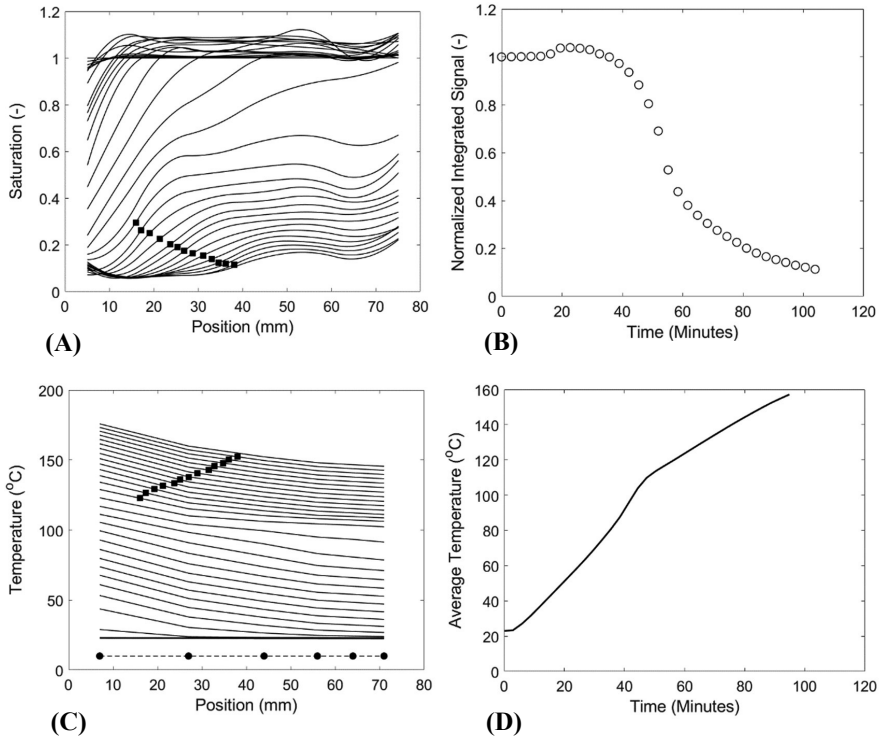


**Figure 2.6:** First-drying of a conventional castable cured for 48 hours. The (A) NMR saturation profiles (B) total normalized saturation as a function of time (C) temperature profiles and (D) the average temperature as a function of time. The black square markers from (A) and (C) are a visual guide for the drying front in the saturation and temperature profiles. The 6 circular markers in (C) correspond to the thermocouple positions. The average time in between profiles is 3-4 minutes, with a total measuring time of 1.5 hours.

It is also this lower range of moisture content that is most problematic from an industrial point of view, since the residual moisture must be slowly released as the corresponding steam pressures within the pores become aggressively high (depending on specific material characteristics). For Conventional Castables, the temperature of the front begins at 100 °C and does not exceed 150 °C. Therefore, the maximum pressure (based on the saturated vapour pressure curve) at the drying front is only 5 bars (0.5 MPa). These pressures are not significantly high compared to the strength of the material ( $\gg 1$  MPa).

## 2.5 Conclusion

In this study we have demonstrated and presented the functionality of a high-temperature NMR setup capable of performing non-destructive measurements on conventional castables during first-heat up. Due to the influence of changing temperature on transverse relaxation and magnetization, we have shown that the scale of the total correction factor to our signal is on the order of 25-30 % of the degree of saturation. Therefore, the  $T_2$  relaxation has to be measured at the same time as the temperature for each point in the sample. Furthermore, we demonstrate the possibility of measuring quantitative moisture content profiles during drying of conventional castables by NMR, thereby providing direct observation of transport processes that are otherwise unobservable by destructive methods.

Applying the correction scheme to a first-drying experiment on a conventional castable cured for 48 hours reveals that there are two principal drying stages: externally limited and internally limited drying; in the former case fast, environment-driven drying is observed, whereas in the latter case slow transport-driven drying is observed. Furthermore, the internally limited drying period correlates with the development of a drying front that penetrates the pores in the temperature range of 120-150 °C at the front position. By the time the maximum temperature of the front is reached, the average temperature across the sample is just under 200 °C.



## 2.6 References

- [1] W.E. Lee and R.E. Moore, "Evolution of in Situ Refractories in the 20th Century," *Journal of the American Ceramic Society*, vol. 81, no. 6, pp. 1385-1410, 1998.
- [2] J.D. Smith and W.G. Fahrenholtz, "Refractory Oxides," in *Ceramic and Glass Materials: Structure, Properties and Processing*. Davis, Troy, Springer, 2008, pp. 87-108.
- [3] A.P. da Luz, M.A.L. Braulio and V. C. Pandolfelli, *Refractory Castable Engineering*. Baden-Baden & Karlsruhe: Federation for International Refractory Research and Education & Goller Verlag, 2015.
- [4] World Steel Association, "Press Release: July 2017 crude steel production for the 67 countries," 2017.
- [5] N. Toropovs, F. Lo Monte, M. Wyrzykowski, B. Weber, G. Sahmenko, P. Vontobel, R. Felicetti and P. Lura, "Real-time measurements of temperature, pressure and moisture profiles in High-Performance Concrete exposed to high temperatures during neutron radiography imaging," *Cement and Concrete Research*, vol. 68, pp. 166-173, 2015.
- [6] K.G. Fey, I. Riehl, U. GroB and R. Wulf, "Modelling the First Heat-Up of Refractory Concrete," in *Proceedings from the 56th International Colloquium on Refractories*, Aachen, Germany, pp. 99-102, 2013.
- [7] O. Valentin and F. Nazaret, "Industrial Simulation for Pore Pressure Prediction During the First Drying of Refractory Castables," in *Proceedings from the 57th International Colloquium on Refractories*, Aachen, Germany, pp. 2-6, 2014.
- [8] G.H.A. van der Heijden, L. Pel and O.C.G. Adan, "Fire spalling of concrete, as studied by NMR," *Cement and Concrete Research*, vol. 42, no. 2, pp. 265-271, 2012.
- [9] W.E. Lee, W. Vieira, S. Zhang, K.G. Ahari, H. Sarpoolaky and C. Parr, "Castable refractory concretes," *International Materials Reviews*, vol. 46, no. 3, pp. 145-167, 2001.

- [10] K. Kopinga and L. Pel, "One-dimensional scanning of moisture in porous materials with NMR," *Review of Scientific Instruments*, vol. 65, no. 12, pp. 3673-3681, 1994.
- [11] A. Abragam, *The Principles of Nuclear Magnetism*. Oxford University Press, 1961.
- [12] D.H. Gultekin and J.C. Gore, "Temperature dependence of nuclear magnetization and relaxation," *Journal of Magnetic Resonance*, vol. 172, no. 1, pp. 133-141, 2005.
- [13] G.H.A. van der Heijden, L. Pel, H.P. Huinink and K. Kopinga, "Moisture transport and dehydration in heated gypsum, an NMR study," *Chemical Engineering Science*, vol. 66, no. 18, pp. 4241-4250, 2011.
- [14] S. Godefroy, M. Fleury, F. Deflandre and J.P. Korb, "Temperature Effect on NMR Surface Relaxation in Rocks for Well Logging Applications," *Journal of Physical Chemistry B*, vol. 106, no. 43, pp. 11183-11190, 2002.
- [15] G.H.A. van der Heijden, H.P. Huinink, L. Pel and K. Kopinga, "One-dimensional scanning of moisture in heated porous building materials with NMR," *Journal of Magnetic Resonance*, vol. 208, no. 2, pp. 235-242, 2011.

---

## Chapter 3: Direct observation of the boiling front behavior

---

### Abstract

The drying behavior for various calcium alumina- and hydratable alumina-bonded refractory castables was investigated in the temperature regime of first-drying (100-300 °C). Using a specialized high-temperature Nuclear Magnetic Resonance setup, we were able to directly and non-destructively measure the spatially and temporally resolved moisture distribution, while simultaneously measuring the temperature distribution as well. These measurements show that the drying front position is a linear function with time, which can be explained on the basis of a simplified model where only vapour transport is considered. Based on the measurements and the model one can directly determine the permeability at high temperatures. Moreover, the results demonstrate that the drying front speed and temperature strongly correlates with control of key material parameters (e.g. water demand, binder content, etc.). In particular, microsilica fume-containing Low-Cement Castables displayed the highest vapour pressures, while Regular Castables generated the lowest vapour pressures reflecting the permeability of these materials.

*This chapter has been adapted from Barakat, A.J., Pel, L., Krause, O. & Adan, O.C.G., Am. Ceram. Soc. (2019). doi:10.1111/jace.16814.*

### 3.1 Introduction

Calcium alumina/hydratable alumina castables still pose a serious challenge with regards to removing the physically and chemically bound water components from the porous network prior to their application in steel ladles. Due to the high-risk of generated steam pressures destroying the material at temperatures above 100 °C, castables must be pre-dried under conservative heating schedules below 1 °C /minute to ensure safe evacuation of the moisture. In particular, the dangerous ebullition stage and hydrate phase decomposition stage pose the greatest concern during heat-up. Therefore, a quantitative understanding of the transport physics in the range of first-drying, that is from 100-300 °C, will help guide industrial producers and refractory engineers in selecting suitable heating schedules for a given set of materials.

Furthermore, recent spalling events suggest that controlling key parameters, such as material selection, i.e., binder content, additives, etc., curing time and environmental conditions, is critical to ensure adequate refractory performance [1]. The stability of the chemical hydrates, for instance, very much depends upon the curing time, temperature and ambient environment of castable preparation [2]. Evermore, the mixing time, water demand, binding phases, e.g. calcium alumina vs. hydratable alumina, as well as the use of additives for improving rheology and flow characteristics also affect the properties of these materials, e.g. porosity, permeability, etc [3][4].

However, the exact contribution to mechanical failure, from the respective de-watering stages of drying already alluded to above, are not quantitatively understood. On the one hand, the release of physically free water from the pores is intensified by the ebullition stage of drying, due to the pressure-determined escape of water from the pores. Since there is fast formation of vapour at some distance from the surface, as more liquid is located at greater depths within the material, the balance between internal gas development and removal from the surface, for a given applied heating rate, material permeability and material thickness, is not easily attained [3]. Furthermore, at higher temperatures the hydraulic bonds release their water molecules, thereby generating increased porosity and diminishing the mechanical strength of the material [5].

Therefore, in order to evaluate the likelihood of spalling, destructive and indirect methods are often employed to characterize the dehydration and mass change of water (DSC/TGA); or phase morphology (e.g. by XRD). Unfortunately, these techniques are limited by a lack of access to information due to inadequate sample sizing, thereby preventing development of a temperature gradient, or destruction of the specimen. More importantly, vital information for deriving transport properties, such as the position, temperature and speed of the boiling front, and thus the associated vapour pressure, cannot be obtained through these conventional experimental techniques. Furthermore, extracting reliable empirical data on the moisture distribution throughout first-drying will help narrow the assumptions that are often made in conceptual modelling, which until now have been mostly based on second-guessing the internal transport dynamics, such as the relationship between vapour/liquid mass flux [6,7,8].

In the previous chapter, a high-temperature Nuclear Magnetic Resonance (NMR) setup was developed and characterized demonstrating that the moisture distribution can be directly measured for Regular Castables (RC) [9][10]. As NMR is a resonance technique, it can be made sensitive to only hydrogen and therefore to moisture as well. Hence, the moisture profile can be non-destructively measured with a high spatial resolution on the order of 2-3 mm. In this chapter, we use the same experimental setup to investigate the moisture and temperature profiles as a function of position for a variety of castables based on different material formulation inputs. By measuring the moisture distribution over time, we can quantify the position of the drying front, where the moisture removal is dependent on internal transport processes, as well as the temperature and vapour pressure at the front position.

### **3.2 First-drying theory: a first-order approximation**

During a one-sided first-drying experiment, the total moisture-loss of castables can be described by two general stages: (i) externally limited and (ii) internally limited drying. In the first case (i), the mass-loss rate is governed by externally controlled boundary conditions, such as humidity, temperature or heat flux at the surface. In this regime, liquid transport will be the dominant process, which is furthermore reflected in the homogeneous moisture profiles. Therefore, for stage (i) drying the environment is the limiting factor.

However, after the moisture content drops below a certain threshold, i.e., the so-called critical moisture content, the liquid network connectivity is no longer maintained. Therefore, the

locally distributed moisture can only escape as vapour. This release occurs as a liquid-vapour boiling front developing and entering the pores of the material, corresponding to stage (ii). Depending on the material of choice, this transition can occur at temperatures in the range of 100-200 °C. From this moment on the vapour flux is pressure-driven by ebullition, where the transport process is limited by internal properties of the pore structure, i.e., the permeability of the material. Therefore, for stage (ii) drying the internal vapour transport is the limiting factor.

Once the drying front has entered the material we can model the vapour transport on the basis of a sharp front approximation, which is schematically shown in Figure 3.1 [11]. Here, we assume that the moisture and heat transport can be described in 1D, where  $x$  is the distance towards the heated surface of a sample with length  $L$ . At the position  $x=u(t)$ , the sharp boiling front of the sample divides the material into a wet part and a dry part. In this model, we introduce a couple of simplifying assumptions. First, we assume that the liquid saturation content in the wet region of the sample remains constant, i.e.,  $S(x,t) = S$ ; here  $S$  corresponds to the moisture level where a drying front appears. Therefore, liquid transport over time in the wet zone can be neglected. At the same time, we assume that in the dry part vapour transport is the dominant process. Secondly, while we are close to the temperatures of dehydration 200-300 °C, it is physically free water (i.e., non-chemically bound water) which is mostly released from 100-300 °C.

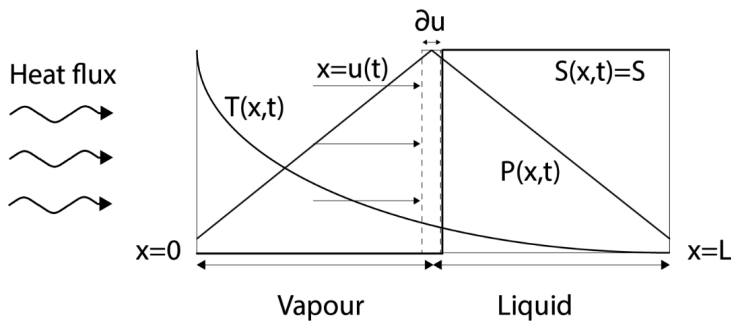


**Figure 3.1:** Schematic of the conceptual model describing one-dimensional moisture and vapour transport during heating. The variables  $P$ ,  $T$  and  $S$  correspond to the pressure, temperature and saturation (moisture content), respectively. A uniform heat flux is directed toward the surface of the sample, at  $x = 0$ . The back end of the sample ( $x = L$ ) is closed and insulated. At the boiling front ( $x = u(t)$ ) the moisture evaporates and is pushed out at the drying surface.

Driven by the boiling of moisture, the drying front will recede into the material. Assuming the pore liquid volume per unit area  $nS du$  is transformed into vapour over time  $dt$ , the boiling front enters the material with speed  $du/dt$ ; here  $n$  corresponds to porosity. Accordingly, a vapour mass-flux  $J_V$  is established. This mass-flux is determined by the product of the volumetric-flux  $q$  and the liquid density  $\rho$ . The density is defined by the molar volume  $V_m$  and molecular weight  $M_w$ . Based on this relationship, liquid water is boiling at the front and evacuated from the pores by escaping toward the surface as vapour:

$$J_V = q\rho = -\frac{nS}{V_m} \frac{\partial u}{\partial t}. \quad (3.1)$$

In our system, the pore length scale is much greater than the mean free path of a water molecule, therefore the continuum approximation of vapour transport is valid. Hence the vapour flow can be calculated from Darcy's law where the vapour flow will be determined by the pressure distribution, reaching a maximum value at the boiling front position. The surface pressure is fixed by external boundary conditions, i.e., atmospheric pressure of 101 kPa. Furthermore, the vapour phase itself can be modeled as an ideal gas and hence the vapour flux is given by [11]:

$$J_V = q\rho = \left( -\frac{k}{\mu} \frac{\partial P_V}{\partial x} \right) \left( \frac{P_V M_w}{RT} \right), \quad (3.2)$$

where  $k$  is the permeability,  $V_m$  the molar volume,  $\mu$  the viscosity of vapour,  $R$  the universal gas constant and  $T$  the temperature. (Here we have used  $p = \rho RT/M_w$ )

The pressure at the boiling front is determined from the Antoine equation, assuming a local thermodynamic equilibrium exists between liquid and vapour,

$$\log_{10}(P_V) = A - \frac{B}{C + T}, \quad (3.3)$$

where  $A=8.14$ ,  $B=1810$  and  $C=244$  are constants [12][13].

As a first-order approximation, we may assume that  $\partial P/\partial x \approx \Delta P/u$  and hence by combining Eq. (3.1) and (3.2), we get the following expression for the boiling front position as a function of time:

$$\frac{\partial u}{\partial t} = \frac{kV_m}{2\mu RTnS} \frac{\Delta P_v^2}{u} \quad (3.4)$$

The input for temperature can be taken directly from the experimental data, i.e., the measured temperature profiles which will be presented later on. Hence, by combining Eq. (3.1) and (3.2), we arrive at Eq. (3.4), a first-order differential equation that relates the velocity of the boiling front with the other properties of the material. The numerical solutions to Eq. (3.4) are presented in the subsequent sections and compared with the experimental results. In this simplified transport model, the only free parameter is the permeability which allows us to quantitatively assess the difference in drying behavior for different materials.

### 3.3 Experimental Setup

A home-built NMR setup was used for conducting non-isothermal one-sided heating on freshly cured castables in the temperature regime of 100-300 °C. A schematic view of the setup is presented in Figure 3.2. The experiments were conducted inside a whole-body 1.5 T magnet (Intera, Philips). In order to send the RF pulses and receive the NMR signal for measuring moisture profiles, a home-built, low-pass Birdcage coil was constructed and tested. With this configuration we achieved pulse times as short as 50  $\mu$ s. The birdcage coil is secured around a ceramic aluminum oxide tube, which is capable of withstanding temperatures beyond 1000 °C. Therefore, the setup can be exposed to high temperatures without risking damage to the equipment. For providing the magnetic field gradient use is made of two larger coils, oriented in an anti-Helmholtz configuration. With a calibrated strength of 80 mT/m, this gradient allows us to perform one-dimensional slice imaging without moving the sample. With this gradient and applied pulse, we can achieve a spatial resolution on the order of 2-3 mm. Situated around the birdcage is a diametrically adjustable Faraday cage for tuning/matching of the Birdcage coil. In addition, this Faraday cage should also protect the superconducting magnet of the wholebody MRI in case explosive spalling will occur.

Special attention has been given to ensure the NMR signal can be measured quantitatively. In order to achieve this, an additional shielding coil is placed between the sample and the birdcage coil in order to minimize the effects of changes in the dielectric constant [14][15].



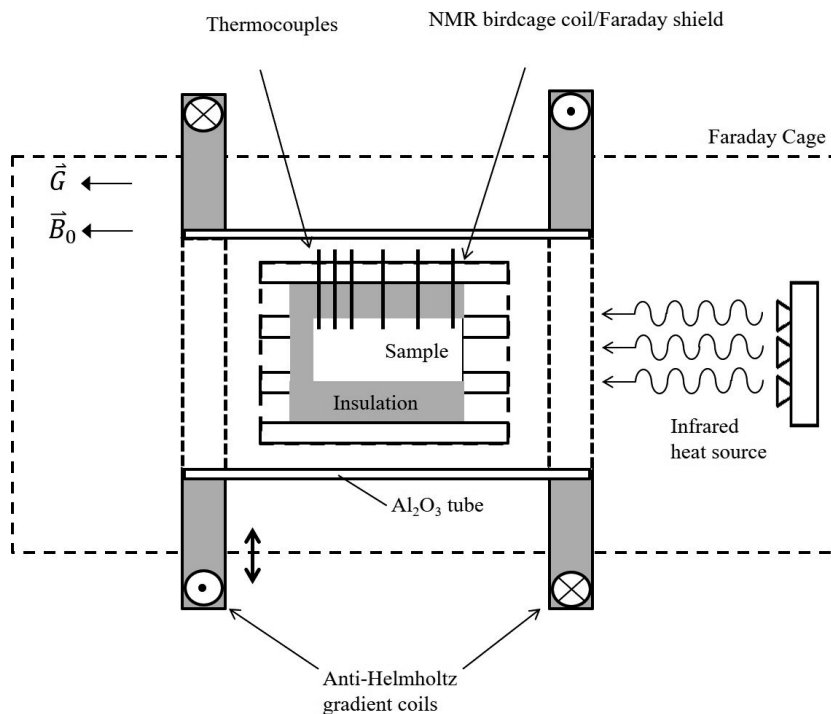


**Figure 3.2:** Schematic of the experimental setup for measuring the moisture profiles during heating up. The sample is placed inside the birdcage coil, secured by an aluminum oxide ceramic tube. Thermocouples are placed inside the holes of the sample. The insert is enclosed by a Faraday cage for tuning/matching. A pair of anti-Helmholtz coils is used to generate the magnetic field gradient. An array of 100 W halogen lamps is used to provide the heat, with a typical heat flux of  $3.5 \text{ kW/m}^2$ .

The cylindrical samples, 74 mm in diameter by 74 mm in length, themselves are isolated with rock wool and Teflon, preventing heat and moisture loss, respectively, exposing only one surface toward external heating. In this way, we can create a 1D heat and moisture flow experiment. In order to measure temperature profiles, each sample is equipped with 6 K-type thermocouples. The heating source itself is provided by an array of gold-coated 100 W halogen lamps capable of heating the surface up to temperatures above 200 °C. The maximum heat flux and heating rate is  $3.5 \text{ kW/m}^2$  and  $2 \text{ °C/minute}$ , respectively. The lamps were gold-coated, because gold has a high infrared reflectivity of 0.98. For comparison purposes, the final measured moisture and temperature profiles should be aligned in time; to

this end, both datasets were linearly interpolated to the same points in time, without significantly shifting the data beyond a threshold that would impact our conclusions.

### **3.4 Sample Preparation**

The materials for this study were selected for comparison according to different formulation parameters: water demand, binder content, fillers and additives. On this basis, the materials are grouped into three different families: Regular Castables (RC); Low-Cement Castables (LCC); and Non-Cement Castables (NCC). By adjusting these material inputs, we can map the influence of specifically chosen material parameters on the drying behavior, in particular the speed and temperature of drying.

The different samples were prepared according to a formulation recipe list as shown in Table 3.1. The castable components (total batch weight 5 kg) were dry mixed for 1 minute and then wet mixed for 4 minutes in an A 200 Hobart mixer at speed 1 before being mechanically vibrated at an amplitude of 0.5 mm. NCC required a longer wet mixing time of 6 minutes, in order to achieve optimum dispersion of the solid components. The dry components themselves consist of the aggregate, which are broadly sized tabular alumina grains ranging from tens of micrometers to millimeters, and fine filler, e.g. reactive alumina or microsilica addition [16]; chemical binder, i.e., calcium alumina or hydratable alumina and additives for controlling rheology, reaction kinetics and/or dry-out behavior, i.e., accelerators, dispersing agents and permeability enhancing fibers. The commercial label for these components is provided in Table 3.1.

**Table 3.1:** Recipe list of the different castables considered in this study. The mixing components consist of the aggregate, fine filler, binder, additive and water demand along with the associated commercial description. The dry components (aggregate, fines and binder) add up to 100 %; the water demand is taken with respect to the dry components. The tabular alumina component is a broad grain size distribution for which only the upper bound is provided in the table.

Component	Commercial Label	RC (% Dry)	LCC (% Dry)	LCC Fume A (% Dry)	LCC Fume B (% Dry)	NCC (% Dry)
Tabular Alumina T60/64	≤ 6 mm	80	82	82	82	84
Alumina	CL 370	-----	13	-----	10	13
	CT 9 FG	-----	-----	10	-----	-----
Microsilica	Elkem U971	-----	-----	3	3	-----
Binder	Secar 71	20	5	5	5	-----
	Alphabond 300	-----	-----	-----	-----	3
Additives	ADS 3/ADW 1 (LCC/NCC)	-----	1	-----	-----	1
	M-ADS 1/M-ADW 1 (LCC Fume)	-----	-----	1	1	-----
	PP Fibers	0.08	0.08	0.08	0.08	0.08
Water Demand (% dry basis)	Dry Basis (excluding additives)	9	4.7	4.7	4.5	4.6

The samples are cast into cylindrical Teflon beakers, with dimensions of 74 mm in diameter by 74 mm in length. A template scale and Teflon needles are used for positioning the thermocouples for temperature profile measurements: 7, 27, 44, 56, 64 and 71 mm from top to bottom. Immediately after casting the samples are completely covered, so as to prevent evaporation, and cured for 24 and 48 hours at 20 °C. The curing times were chosen in order to assess the effect of changes in the hydration state, which is reflected in the pore structure, on drying behavior. In Table 3.2, typical values for the initial moisture content, permeability and density are provided for materials cured for 48 hours. The initial free moisture content is calculated according to the total amount of moisture loss, i.e., of free water, after an experiment. The permeability measurements were performed using the Air Permeability Test,

at room temperature, by passing gas through the specimen and into a vacuum chamber [17]. It was found that there was little difference in the permeability from 24-48 hours curing time, i.e., within an experimental accuracy of 0.01 mD. In the case of NCC, the permeability is taken from literature in which the samples were cured at higher temperatures and characterized with different equipment. Therefore, it is only provided as a reference and not to be directly compared with the permeability results of the other materials.

**Table 3.2:** Typical values for the initial free moisture content, permeability, density and boiling front speed of the different materials considered in this study.

Material Properties	RC	LCC	LCC Fume B	NCC
Initial Free Moisture Content ( $\text{m}^3 \text{m}^{-3}$ )	0.05	0.12	0.10	0.20
Permeability ( $\text{m}^2$ )	$1.33 \times 10^{-16}$	$4 \times 10^{-17}$	$7.30 \times 10^{-17}$	$3.8 \times 10^{-17}$ [3]
Density ( $\text{kg}/\text{m}^3$ )	2850	3191	3157	3248
Front Speed (mm/min)	0.60	0.22	0.35	0.08(48 h)/0.17(24 h)
Time Front Appears (minutes)	50	100	100	170

### 3.4.1 Measuring moisture loss during first-drying

As an example material, RC is used to discuss the one-dimensional, one-sided moisture loss throughout a first-drying experiment. Due to the relatively short sample length (74 mm), the timescale of an experiment is around 1.5 hours. In Figure 3.3B, the measured temperature profiles are shown, which demonstrate the standard techniques of evaluating moisture loss in a first-drying experiment. As can be seen, once the heat flux is applied the temperature at the surface begins to rise and a temperature gradient develops. The sample average heating rate is 1.5 °C/minute. The maximum surface temperature reached at the top is around 180-200 °C. As soon as the temperature at the surface reaches values on the order of 110 °C, a decrease in both the heating rate and temperature gradient is observed. This indicates that around 110 °C a drying front should develop, however no direct information can be taken from this temperature data.

In Figure 3.3A, the corresponding saturation profiles are shown demonstrating what additional information can be measured by NMR. Here we have plotted the saturation profiles, i.e., each profile is obtained by dividing by a reference taken at the beginning of the experiment at room temperature, corresponding to a uniform saturation of 1. This allows for sample inhomogeneities to be eliminated from the measured quantitative moisture content. Depending on the number of averages, measuring each profile for RC takes on average 1 minute. The time step in-between subsequent measurements is 3 minutes.

As can be observed from the saturation profiles in Figure 3.3A, three drying stages are identified (I-III). Initially as the temperature is increasing from room temperature up to about 70 °C we see that the total moisture content rises above the first profile, corresponding to a saturation level above 1. This initial rise (I) corresponds to the transforming pore structure upon initial heating. During this initial heating stage up to 70 °C, dehydration will occur [2][9], where chemically combined water is released, resulting in an increase of the moisture content.

As soon as the temperature rises above 70-80 °C a new drying stage has begun (II). From this moment on the sample is drying quite fast as the internal transport is dominated by liquid transport and the dewatering rate is determined by external boundary conditions, such as temperature and humidity, i.e., the externally limited drying. At the same time this is a combined process of drying and moisture release as in this temperature range the metastable hydrate  $\text{CAH}_{10}$  also loses its water and converts to the stable crystalline  $\text{AH}_3$ , and thereby transforms the pore structure, according to a multistep process:  $6\text{CAH}_{10} (-27\text{H}) \rightarrow 3\text{C}_2\text{AH}_8 + 3\text{AH}_3 (-9\text{H}) \rightarrow 2\text{C}_3\text{AH}_6 + 4\text{AH}_3$ .

However, these phases evolve as a function of time and temperature. Previous investigations suggest that  $\text{CAH}_{10}$  and  $\text{C}_2\text{AH}_8$  will transform into the stable  $\text{AH}_3$  and  $\text{C}_3\text{AH}_6$  at 110-120 °C or dehydrate entirely ( $\text{C}_2\text{AH}_8$  at higher temperatures)[2][5]. It is also expected that the rapid transformation of  $\text{C}_2\text{AH}_8$  to  $\text{C}_3\text{AH}_6$  at 80-100 °C, or complete decomposition, can occur which is consistent with the fast moisture increase we also observe in these temperature ranges [2].

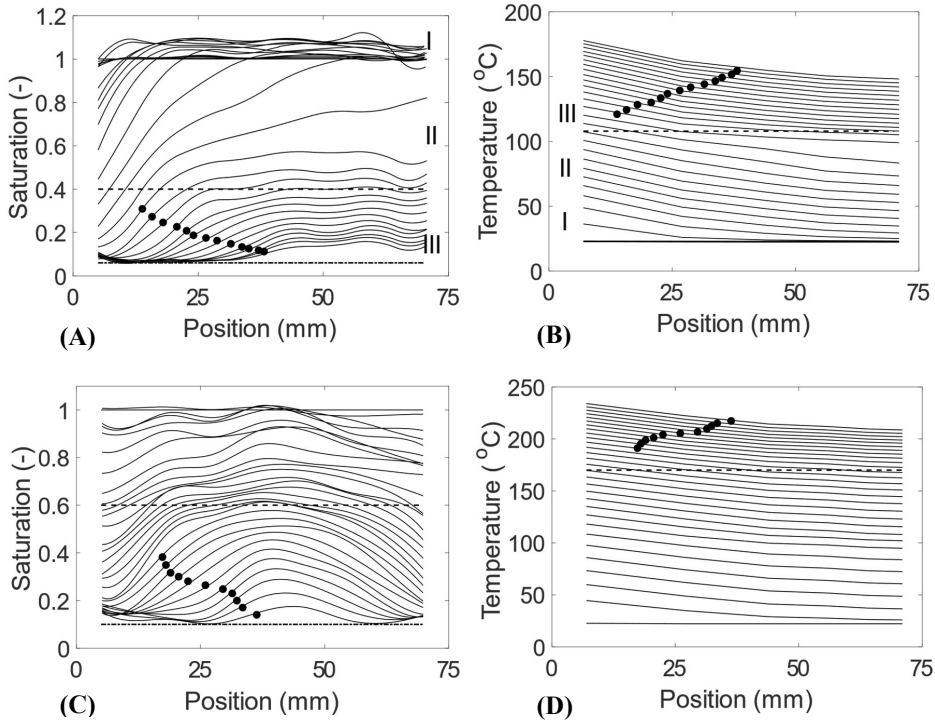


**Figure 3.3:** The measured saturation and temperature profiles for RC (A) and (B) and LCC Fume A (C) and (D) cured for 48 hours. The black markers indicate the position of the drying front as a function of time. The time in between each profile for RC is 3 minutes and LCC Fume is 6 minutes. The data from each experiment was normalized to an initial isothermal reference profile at room temperature, with a significantly high number of averages to correct for inhomogeneities in the sample. The dashed lines in the figures indicate the critical moisture content. The dashed-dotted line at the bottom of the saturation profile figures corresponds to the residual moisture background level. Items I-III in (A-B) correspond to the three different drying stages of RC: (I) early dehydration (II) externally limited drying and (III) internally limited drying.

As also indicated by the temperature measurements around 110 °C, a new phase in the drying process has begun (III). From this point on a drying front begins to develop and the drying slows down. This transition coincides with the critical saturation content of 0.4 in the sample, which is indicated by the dashed line. From this moment on the dewatering process is internally limited, as the drying is dependent on the internal pore structure and transport processes governing moisture loss. At the same time, the greater amount of energy required to remove large quantities of free water from the porous network results in a decreased sample heating rate. This latter effect is due to the high latent heat of evaporation of water.

We can identify the drying front position by taking the midpoint along the liquid-vapour boundary in the moisture distribution, as indicated by the black markers in Figure 3.3A. The corresponding temperatures at the drying front are indicated by markers in the temperature profiles in Figure 3.3B.

The critical saturation content corresponds to the transition point in the drying rate, i.e., from externally limited (fast) to internally limited (slow) drying. In Figure 3.4 we have demonstrated this by plotting the total average saturation content as a function of time for four different materials: RC, LCC, LCC Fume and NCC. Again, we use RC (from Figure 3.3A) as the standard example and employ linear fitting of the data for the two different stages of drying. To a first-order approximation, the critical saturation content is quantitatively defined as the interception point of these two fitted lines (see small dashed line in Figure 3.4). For the other materials, the transition is less sharp due to the different characteristics of those materials.

In Figure 3.5A and 3.5B we have plotted the corresponding front position and the temperature at the front for RC as a function of time. Indeed, the measurement reveals that the temperature at the drying front is increasing as the boiling front progresses deeper into the material. As can be seen, both the front position and front temperature are linear functions of time. Furthermore, the drying front first emerges 50 minutes after the heat is turned on. It is observed here that as the front is entering the material, the temperature at the front increases thus indicating the increasing boiling pressure in order for the vapour to escape at the top of the sample. In Figure 3.5C, the front temperature has been plotted as a function of the front position, where again a linear relation is observed. The maximum front temperature reached is 150 °C, with a corresponding position of 40 mm from the hot face of the material. The vapour pressure can be calculated on the basis of the boiling front temperature (see Figure 3.5B). Hence, the saturated vapour pressure of the front starts at 0.1 MPa and rises up to 0.5 MPa (5 bars) during this experiment with RC.

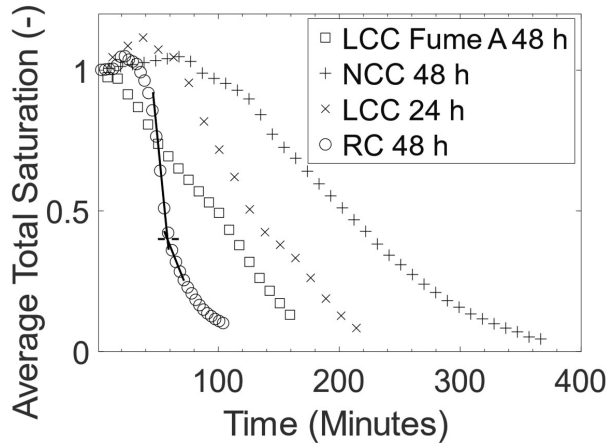


**Figure 3.4:** A plot of the total average saturation content as a function of time for four different materials: RC, LCC, LCC Fume A and NCC. The plot of RC demonstrates the quantitative determination of the critical moisture (saturation) content by fitting two lines (solid lines) to the externally and internally limited drying stages. The intercept of these fits quantitatively defines the critical moisture content, which for RC is 0.4 (short dashed line).



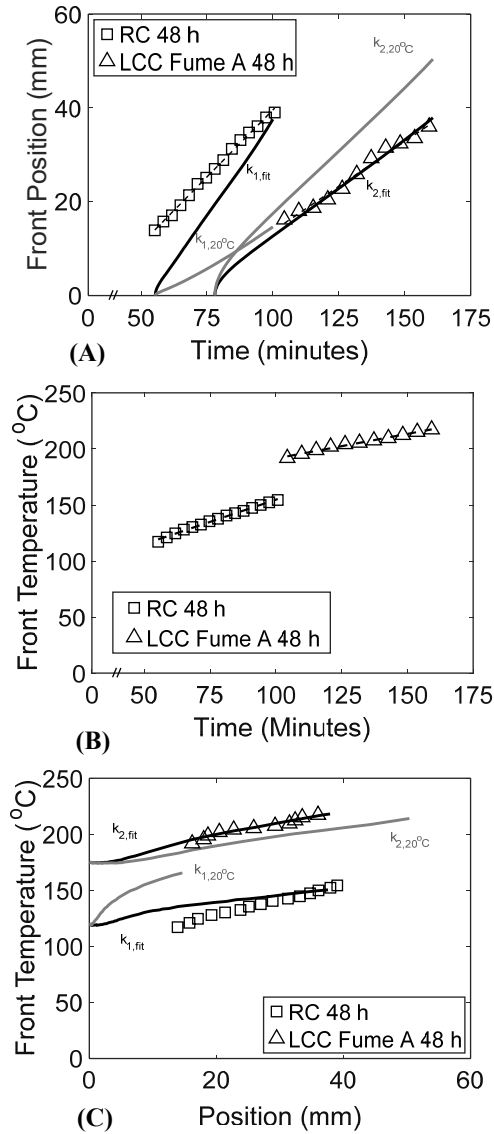


**Figure 3.5:** The boiling front position as a function of time (A), the boiling front temperature as a function of time (B) and front temperature as a function of front position (C) for LCC Fume A and RC cured 48 hours as determined from the measured moisture and temperatures profiles (see Figure 3.3). The simulations based on the best fitted permeabilities are indicated by the solid black lines ( $k_{fit}$ ). The simulations based on the experimentally determined permeabilities at 20  $^\circ C$  are indicated by the solid grey lines ( $k_{20^\circ C}$ ). The dashed lines passing through the data are a linear fit to the boiling front speed.

As can be seen in Figure 3.3A, at the end of the drying process there is still some residually distributed moisture on the order of 10 % in the sample. This moisture content is however well above the noise level, which is just under 1 %.

This is likely due to the fact that free moisture remains in the small pores over increasing time and increasing temperature. If we look at the average moisture content at the surface of the sample, i.e., the averaged moisture content over 7-25 mm, which is shown in Figure 3.6A, we see that the moisture level stagnates toward the end of the experiment.

One possible explanation for the source of this feature is that since we are approaching 200 °C, chemically bonded water is becoming released from the solid matrix and thereby contributing to the signal as free moisture [2]. In Table 3.3 we have provided the various temperature regimes where hydrate decomposition occurs [2][3]. Accordingly, the stable components  $AH_3$  and  $C_2AH_8$  are expected to release water through a mineralogical phase transformation from 170 °C onwards. This process will continue for temperatures above 200 °C where the activation energy associated with dehydration can be found elsewhere [18]. Since we are within the starting temperature range of the dehydration process, it is likely that water still remains inside the small, isolated pores. Indeed taking an RC sample, after drying in an NMR experiment, and placing it in a 1000 °C furnace reveals that more than twice as much previously liberated water will continue to be released over higher temperatures.

To further test the hypothesis that free water is trapped in the small pores, the experiment was repeated over a longer time, where at the end of the experiment the heating was turned off and the results are shown in Figure 3.6B. Here, we have again plotted the average moisture content as a function of time. As can be seen, the moisture content slowly decreases with time as the heat is turned off, which is likely due to rehydration with the cementitious phases. After the sample sits for 1-2 days at room temperature, following the end of the experiment, the total signal has decreased to 2 %. Therefore, there is still free moisture trapped inside the small pores, which has not rehydrated.

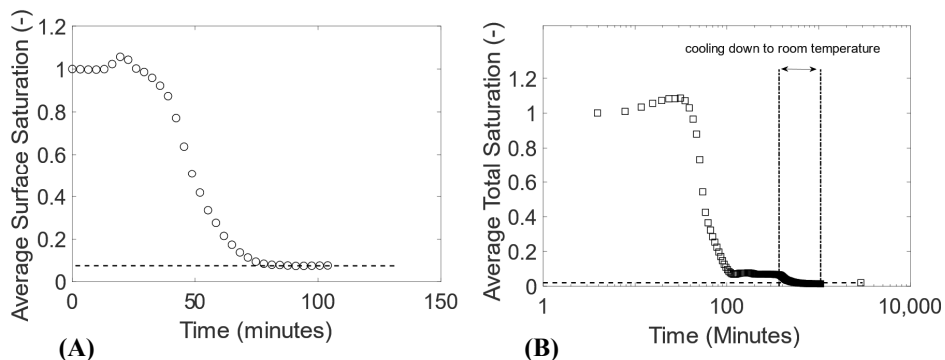


**Figure 3.6:** The averaged moisture content over 7-25 mm of the sample as a function of time (A). The dashed line illustrates the stagnating background moisture level. The average moisture content over the whole sample as a function of time (B). After 400 minutes have passed, the heat is turned off and the sample cools. The final moisture content here is 0.02 and indicated by the dashed line.

**Table 3.3:** List of hydrate phases and their corresponding dehydration temperatures [2,3].

Hydrate Phases*	Decomposition Temperature (°C)
CAH <sub>10</sub>	120
C <sub>2</sub> AH <sub>8</sub>	170-195
C <sub>3</sub> AH <sub>6</sub>	240-370
AH <sub>3</sub> - gibbsite	210-300
Alumina gel	100

\*C = CaO, A = Al<sub>2</sub>O<sub>3</sub>, H = H<sub>2</sub>O

For the purpose of comparing two materials with very different properties, we have also plotted the results of the measured temperature and moisture profiles for LCC Fume A as shown in Figure 3.3C and 3.3D, where the time-step between subsequent profiles is 6 minutes. The material properties are listed in Table 3.1. As a first observation, we see the moisture content doesn't rise above 1 for LCC Fume. The changing hydration kinetics seen with RC, once the sample heats up corresponding to the transformation of the high-solubility metastable hydrates as a function of temperature, is not observed with LCC Fume.

In contrast to RC, we observe that as the surface temperature of LCC Fume A increases, the material immediately begins to dry uniformly until the saturation level is on the order of 0.6. From this moment on there is a transition, i.e., the temperature slowly increases until 200 °C after which a drying front begins to enter the material. This feature again corresponds to the transition in the temperature profiles where the heating rate decreases. It should be taken into

account LCC Fume A contains four times less hydraulic binding phases than RC. From the moment boiling occurs, again we observe a linear drying front position as a function of time. If we identify the front position and the corresponding temperature at the drying front, as we did before with RC, we observe that in this case the temperature at the boiling front increases up to 220 °C. This increase in temperature at the boiling front implies that the vapour pressure will approach a maximum of 4 MPa (40 bars), i.e., 15-40 times as high as RC.

### 3.4.2 Comparing experimental results with the conceptual model

In order to validate the observed drying behavior of RC and LCC Fume A we would like to identify the limiting process governing moisture transport in our experiments, i.e., the heat transfer or the vapour transfer. On the one hand, the combined effect of heat capacity and thermal conductivity, i.e., thermal diffusivity, will influence the temperature distribution. That is because more energy must be supplied to evaporate the moisture at the boiling front and hence limits the maximum moisture boiling/loss and therefore the dewatering rate. On the other hand, vapour transport as determined by the high-temperature permeability can also be the limiting factor and therefore limit the dewatering rate.

In order to determine the limiting process we can make a first-order estimation of the characteristic timescales corresponding to the vapour mass-flux and thermal diffusivity,  $t_j$  and  $t_D$ , respectively. The characteristic time scale for the vapour mass-flux is given by;

$$t_j = \frac{L^2 \mu}{k \hat{P}} \quad (3.5)$$

where  $L$  is the length scale,  $\mu$  the dynamic viscosity of vapour,  $k$  the permeability and  $\hat{P}$  the typical vapour pressure. On the other hand, the characteristic timescale for the thermal diffusivity is given by;

$$t_D = \frac{L^2 \rho C}{\lambda} \quad (3.6)$$

where  $\lambda$  is the thermal conductivity and  $\rho$  and  $C$  the density and specific heat capacity, respectively. A list of the values for these parameters is provided in Table 3.4, for both RC and LCC Fume. Here, we apply the same characteristic heat capacity  $C = 900$  J/kg·K for both materials, for which values have been previously determined by the Hot Wire Method [19][20]. The values of thermal conductivity in Table 3.4 are determined for each material on

the basis of the established relationship between bulk density and thermal conductivity of partially dried dense, insulating castables [20]. A plot of the ratio of timescales corresponding to thermal diffusivity and vapour transport as a function of vapour pressure is given in Figure 3.7 for RC and LCC Fume. The typical pressure corresponds to the range of values calculated according to the boiling front temperature in Figure 3.5B for the two different materials. The boiling pressure of RC is in the range of 0.1 – 0.5 MPa; for LCC Fume the pressures are 1-4 MPa. Based on these values, the timescale of thermal diffusivity for RC is 2-3 times slower than that of the mass flux; for LCC Fume, the ratio is 9-10 times. It is only for pressures above 0.1 MPa that  $t_D > t_J$ , as indicated by the dashed line in Figure 3.7. Hence, on the basis of these characteristic timescales we see that thermal transport is too slow, compared to mass transport, to have any significance on the physical interpretation of the data. Thus, for the purpose of validating the experimental data, permeability is the limiting factor affecting vapour transport, and we can thus apply our simplified model.

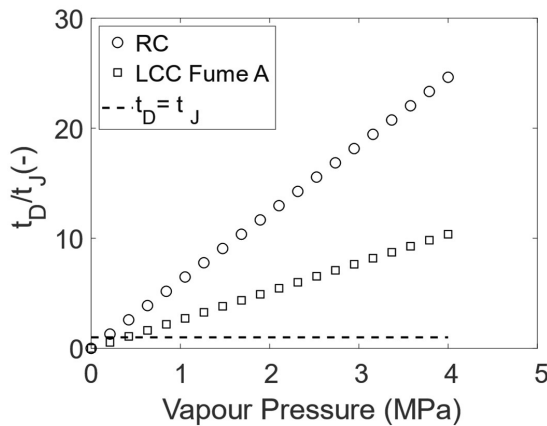


**Figure 3.7:** A plot of the ratio of the characteristic timescales of thermal diffusivity and vapour mass-flux as a function of the typical boiling front vapour pressure for RC and LCC Fume.

**Table 3.4:** Material properties for RC and LCC Fume used to calculate the transport timescales of thermal diffusivity and vapour mass-flux.

Material Properties	RC	LCC Fume A
Permeability (m <sup>2</sup> )	1.33x10 <sup>-16</sup>	7.30x10 <sup>-17</sup>
Density (kg/m <sup>3</sup> )	2850	3157
Thermal Conductivity (W/m·K)	2.77	4
Vapour Pressure Range (MPa)	0.1-0.5	1-4
Specific Heat Capacity (J/kg·K)	900	900

We will use the experimentally determined temperature distribution as an input for the simplified model. Based on these temperature distributions and the experimentally determined permeability at room temperature (see Table 3.2) we can now simulate the front positions as a function of time using this model. The results of these simulations for both RC and LCC are given in Figure 3.5A and 3.5C by a grey solid line. As can be seen only in the case of LCC is the simulation able to reasonably describe the experimental data. This is most probably due to the fact that we have used the permeability as determined at room temperature.

Therefore, we have chosen to use the high-temperature permeability  $k$  as a fitting parameter to our experimental data. The simulations based on the best fitted permeabilities are indicated by the black solid lines in Figure 3.5A and Figure 3.5C. As can be seen in this case the simplified model is able to describe the drying behavior more accurately than before, i.e., using the room temperature-based permeability.

If we now compare the permeability as determined by fitting the simplified model to the data with the permeability determined at room temperature we see that there is a 2- fold difference ( $k_{2,\text{fit}} = 3.5 \cdot 10^{-17} \text{ m}^2$ ,  $k_{2,20^\circ\text{C}} = 7.3 \cdot 10^{-17} \text{ m}^2$ ) for LCC Fume and a 15-fold difference ( $k_{1,\text{fit}} = 2 \cdot 10^{-15} \text{ m}^2$ ,  $k_{1,20^\circ\text{C}} = 1.33 \cdot 10^{-16} \text{ m}^2$ ) for RC. This permeability is a direct reflection of the boiling front speeds of both materials where RC travels through the sample 50-70 % faster than that of LCC Fume A.

The most plausible explanation for this discrepancy in the experimental and fitted values of the permeability is that the materials were dried at 110 °C for 24 hours before the measurements were carried out at room temperature via the Air Permeability Test. As has already been shown in a previous study [9], the pore system of RC undergoes structural transformation from 20-110 °C. This means that over the course of 24 hours the pore network has changed. In fact, after 110 °C the sample mass has slightly decreased as a result of the 24 hour thermal treatment process, indicating moisture loss. Finally, the permeability is measured at room temperature which therefore cannot capture the high-temperature effects taking place throughout an actual first-drying experiment [21][22]. In this sense, the simplified model results more accurately capture the reality of the pore structure than room temperature measurements. As such, the experimentally determined permeability at room temperature should be taken with caution.

It should be mentioned that the pore size distribution of castables is expected to change, thereby transforming the permeability as a function of time and temperature. However, assuming a constant permeability over the narrow temperature range of 100-200 °C still yields a quantitatively reasonable fit of the model to our data for different materials. Therefore, to a first-order approximation, the effects of a dynamic permeability are insignificant to the validation of our experimental data in this temperature range.

### **3.5 Drying Behavior of Castables: Results and Discussion**

The measured moisture and temperature profiles of all other materials tested, i.e., LCCs and NCC (also see Table 3.1), subjected to the same heating program are shown in Figure 3.8. The timescale of these experiments is 2-3 hours. Regardless of material choice, the saturation profiles display similar behavior to RC at the end of the experiment, where a small, residual moisture quantity remains indicating that moisture is still trapped in the small pores.

In the case of LCC/NCC, we observe that the drying front does not emerge until 100 minutes in the experiment have passed. At this point (see Figure 3.9), the temperature at the drying front is on the order of 150 °C and continues on until 200 °C (and above that for NCC) corresponding to a vapour pressure of 0.5-1.5 MPa. For LCC Fume A and B, we observe that the starting and maximum front temperatures reached are close to 200 °C and 250 °C corresponding to a vapour pressure of 1.5-4.0 MPa, respectively. Furthermore, the drying front does not appear until about 100 minutes have passed. These maximum saturated vapour pressures of the front are almost eight-times higher than that of RC.

The slowest drying behavior is observed for NCC cured for 48 hours. For NCC aged 48 hours, it takes 5 full hours before the sample completely dries out, in comparison to the RC, NCC 24 hours and LCC systems. It should be mentioned that the heating for NCC 48 hours was not switched on for the first hour of the experiment. Furthermore, while the drying of the other NCC/LCC materials does not generate an initial moisture content that rises above 1, as we saw in the case of RC, it is seen with NCC cured 48 hours that the initial moisture content does indeed rise above 1 after the heat is turned on. As a note of consideration, this particular material is unique in the sense that it uses a non-cementitious aluminobond binder, which has entirely different bonding phases than CAC.

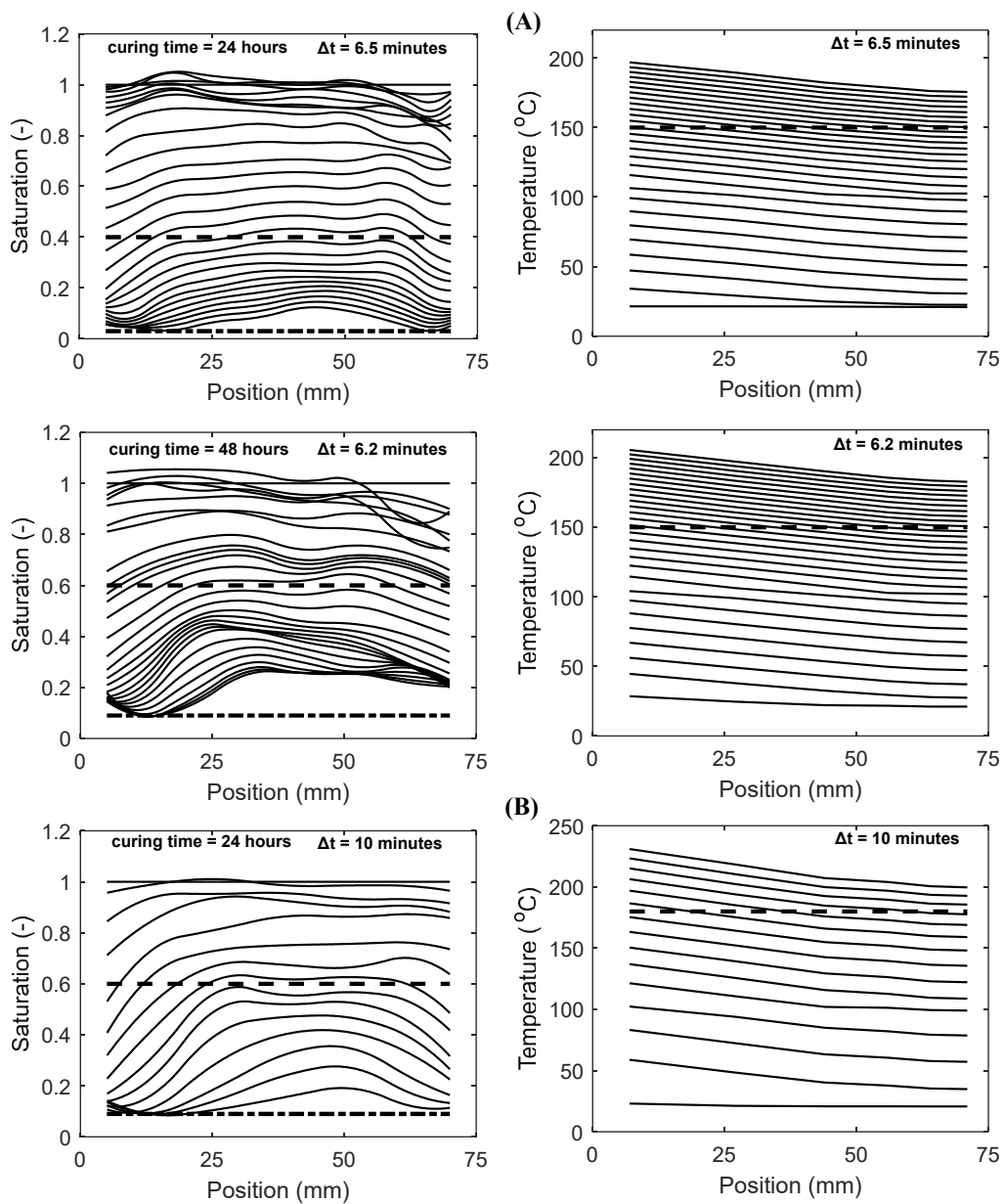
Finally with LCC/NCCs, it is also observed that the moisture is decreasing at the back of the sample, which is not seen in the case of RC. This moisture decrease at the back of the sample correlates with the low-permeability, high-front temperature matrix systems, i.e., all except RC. Since a low-permeability is related to the higher front temperature, it means that the vapour pressure will also be higher. It must be emphasized that the no-flux boundary condition at the back of the sample still remains unviolated and the decreasing moisture content does not corrupt our analysis of quantitative differences in the drying behavior between different materials.

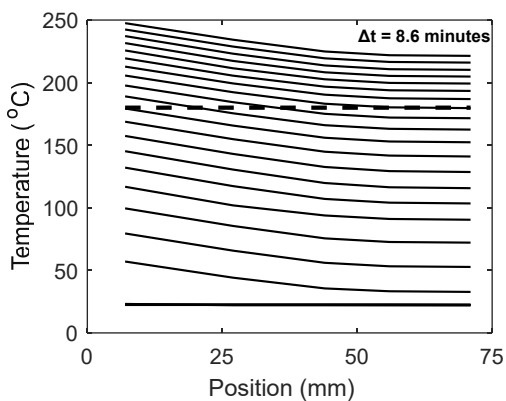
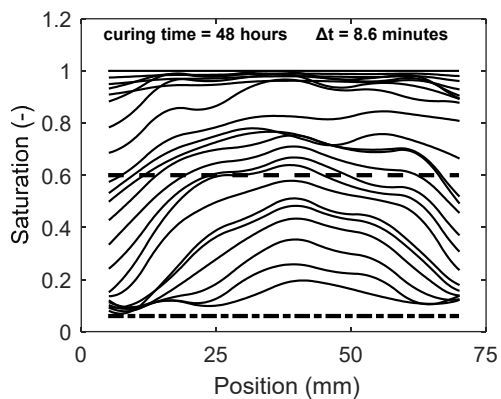
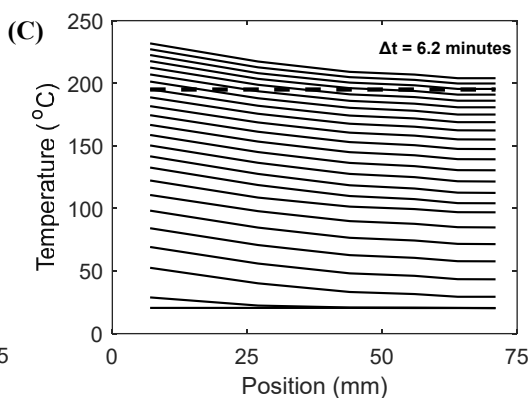
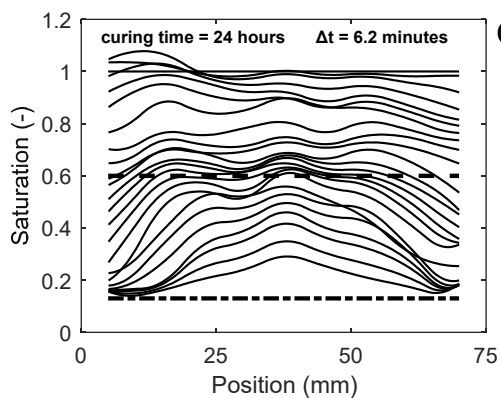
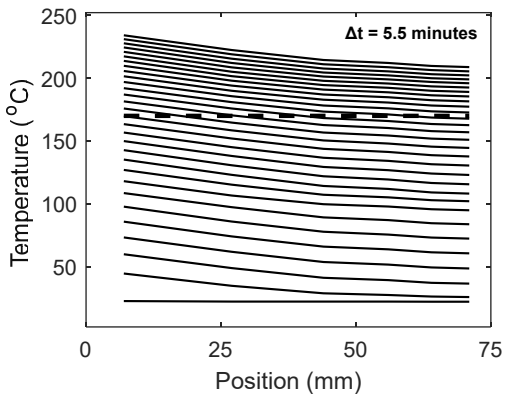
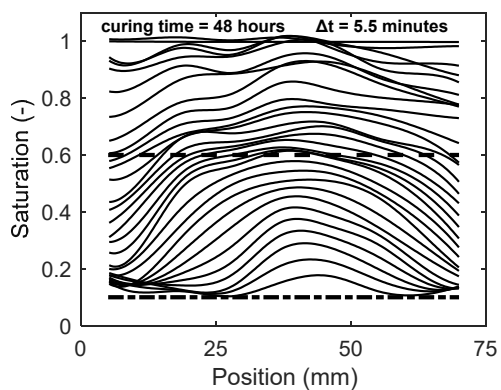
However, although differences can be observed from one material to another, it is difficult to compare all the drying experiments for the various materials. But, as shown in the previous section the drying behavior can be characterized by looking to the front positions and temperatures as a function of time. Such data is provided for all materials considered in this study in Figure 3.9, that is both the front positions and the front temperature as a function of time. As can be seen, there are some common features displayed by the drying behavior of most materials. Firstly, the drying front speed is approximately linear, regardless of material choice. The slope of this front is related to the high-temperature vapour permeability, as already discussed in the previous section according to the simple model. Secondly, it is seen that all materials (with exception to NCC cured for 48 hours) have similar drying front speeds to the first-order approximation (also see Table 3.2). Thirdly, if the front temperatures for various materials are combined into one figure, thereby reflecting the vapour pressure as a function of temperature, the materials can be grouped into roughly three families in order of increasing starting front temperature: (A) RC at 120 °C (B) LCC/NCC at 150 °C and (C) LCC Fume A and B at 170-200 °C.



By again employing the simplified vapour transport model, the drying behavior of these families of materials can be related with the high-temperature vapour permeability. The four solid lines given in Figure 3.9B provide the fitted permeability for these three families of materials, which can be identified, indicating similar drying behavior independent of the material in consideration. In the first case of family A ( $k_1$ ), RC displays the lowest drying front temperature, 120 °C corresponding to the highest permeability on the order of  $10^{-15}$  m<sup>2</sup>. In the second case of family B ( $k_2$ ), the materials LCC (24 and 48 hours) and NCC (24 hours) display intermediate drying front temperatures of 150 °C with all permeabilities on the order of  $10^{-16}$  m<sup>2</sup>. Finally, for family C ( $k_3$ ) Fume-containing LCC materials (24 and 48 hours) display the highest drying front temperature, 170-200 °C, in comparison to families A and B, with a permeability on the order of  $10^{-17}$  m<sup>2</sup>. While NCC cured for 48 hours has a similar starting front temperature as NCC cured 24 hours, it however has a front speed 2-times slower and thus a permeability on the order of  $10^{-18}$  m<sup>2</sup>. Therefore, it is the only outlier case ( $k_4$ ) that lies outside the permeability families A-C.

Therefore, what can be gathered from the experimental results in Figure 3.9 is that the drying front speed is approximately the same for all materials (except NCC cured 48 hours), as shown in Figure 3.9A. Looking further, each family of materials is characterized according to a common starting drying front temperature. Furthermore, while each family has a characteristic fitted permeability, it is observed that there can be an exceptional case in which a material within a family has a unique permeability that is uncommon to the other materials of that same family, i.e., NCC cured for 48 hours. In terms of pressure this means that NCC cured for 48 hours will have the same front temperature and vapour pressure as the materials from family set B, but a lower permeability. Therefore, release of pressurized steam toward the surface will be a relatively slower process than for other materials in the same family. With family C (LCC Fume), it has the second lowest permeability of all materials and displays the highest front temperature and pressure, i.e., on the order of 4 MPa.





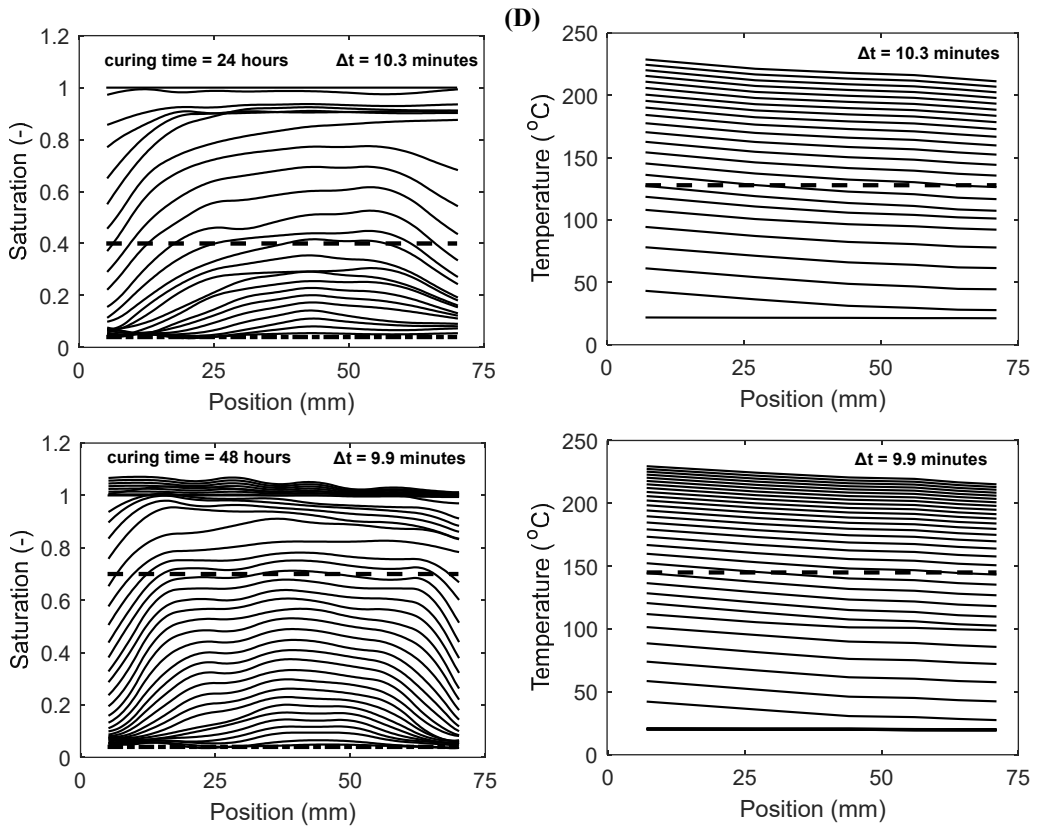


**Figure 3.8:** The measured moisture and temperature profiles for the different materials considered cured for 24 and 48 hours: (A) LCC (B) LCC Fume A (C) LCC Fume B and (D) NCC. The dashed line in the middle of the figures corresponds to the critical moisture content and the solid-dotted line at the bottom indicates the moisture background level. For each material the time between the measurement of two subsequent profiles is indicated.

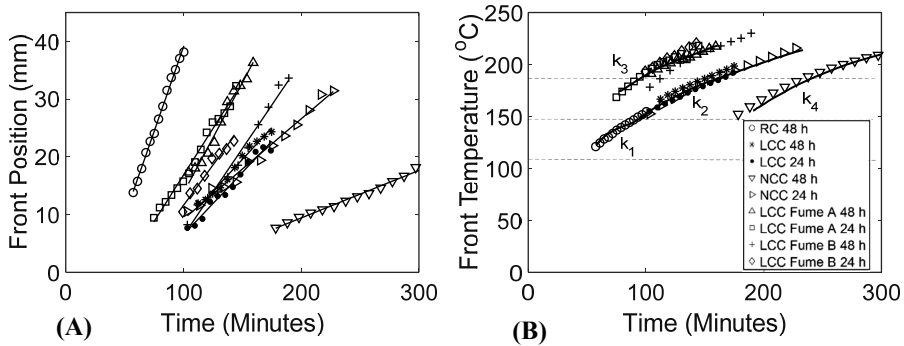


**Figure 3.9:** The boiling front position as determined from the measured moisture profiles as function of time (A) and the boiling front temperature as determined from the measured temperature and moisture profiles as a function of time (B) for all the materials from Figure 3.8 (A)-(D). The solid lines running through (B) are the fitted permeabilities of different material families, with associated fitted values of  $k_1 = 2 \cdot 10^{-15} \text{ m}^2$ ,  $k_2 = 9 \cdot 10^{-17} \text{ m}^2$ ,  $k_3 = 3.5 \cdot 10^{-17} \text{ m}^2$  and  $k_4 = 1 \cdot 10^{-18} \text{ m}^2$ .

### 3.6 Conclusion

In this study, the results for an experimental investigation into the drying behavior of different calcium alumina- and hydratable alumina-bonded castables have been presented. It has been shown that a specialized high-temperature NMR setup is capable of directly and non-destructively measuring the moisture profiles along with temperature profiles during a first-drying experiment, where the samples can reach temperatures as high as 250-300 °C. The measured moisture profiles gathered from the NMR data, in conjunction with the temperature profiles for different materials, provide direct information on the drying front speed and front temperature.

Two primary features are gathered from the analysis of the profiles. First, all materials display a linear drying front speed, regardless of differences in drying behavior for various material compositions. The linear functional form of this drying behavior can possibly be related to the evolution of the moisture diffusivity parameter that appears in analytic models for the non-linear drying problem [23][24].

In order to further interpret this drying front behavior, a simple vapour transport model demonstrates that the boiling front behavior is closely related to the high-temperature vapour permeability; the high permeability corresponds with a low front temperature, where low

permeability materials display high front temperatures. The assumption in this simple model is that pressure-driven flow is the main transport mechanism for vapour.

Based on the drying front temperatures, the materials can be grouped into different families of materials. Additionally, on the basis of the simple model a fitted permeability can be assigned to these different families of materials: (A) RC at 120 °C (B) LCC/NCC at 150 °C and (C) LCC Fume A and B at 170-200 °C, with A-C in increasing order of front temperature and decreasing order of permeability, with exception to NCC cured for 48 hours which has the lowest fitted permeability of all materials. Therefore, the LCC Fume family displays the highest front temperature and vapour pressure. This simple model is unique in the sense that only one free parameter is required,  $k$  the permeability. Here, it is found that the fitted results justify the simple model, where the first-order approximation is quite valid in the regime of vapour transport.

However, there is still one outlier case which does not depend on the fitted permeability alone, that is the exceptionally slow drying of NCC 48 hours. This material has a boiling front temperature range which is within the 150 °C family of materials, even though the fitted permeability is more reflective of the 200 °C family. Here, it has to be taken into account that curing NCC for 48 hours will slow the progression of the boiling front position. Therefore, everything else being equal, adjusting both  $k$  and  $du/dt$  will determine the correct drying front temperature.

### 3.7 References

- [1] J. Spink, "A review of explosive spalling of castable materials," *The Refractories Engineer*, pp. 13-17, 2014.
- [2] F.A. Cardoso, M.D.M. Innocentini, M.M. Akiyoshi and V.C. Pandolfelli, "Effect of curing time on the properties of CAC bonded refractory castables," *Journal of the European Ceramic Society*, vol. 24, no. 7, pp. 2073-2078, 2004.
- [3] A.P. da Luz, M.A.L. Braulio and V.C. Pandolfelli, *Refractory Castable Engineering*. Baden-Baden & Karlsruhe: Federation for International Refractory Research and Education & Goller Verlag, 2015.
- [4] F.A. Cardoso, M.D.M. Innocentini, M.F.S. Miranda, F.A.O. Valenzuela and V.C. Pandolfelli, "Drying behavior of hydratable alumina-bonded refractory castables," *Journal of the European Ceramic Society*, vol. 24, no. 5, pp 797-802, 2004.
- [5] W.E. Lee, W. Vieira, S. Zhang, K.G. Ahari, H. Sarpoolaky and C. Parr, "Castable refractory concretes," *International Materials Reviews*, vol. 46, no. 3, pp. 145-167, 2001.
- [6] O. Valentin and F. Nazaret, "Industrial Simulation for Pore Pressure Prediction During the First Drying of Refractory Castables," in *Proceedings from the 57th International Colloquium on Refractories*, Aachen, Germany, pp. 2-6, 2014.
- [7] D. Gawin, F. Pesavento, and B.A. Schrefler, "What physical phenomena can be neglected when modelling concrete at high temperature? A comparative study. Part 1: Physical phenomena and mathematical model," *International Journal of Solids and Structures*, vol. 48, no. 13, pp. 1927–1944, 2011.
- [8] B.A. Schrefler, C.E. Majorana, G.A. Khoury, D. Gawin, "Thermo-hydro-mechanical modelling of high performance concrete at high temperatures," *Engineering Computation*, vol. 19, no. 7, pp. 787-819, 2002.
- [9] A.J. Barakat, L. Pel and O.C.G. Adan, "One-dimensional NMR imaging of high-temperature first-drying in monolithics," *Applied Magnetic Resonance*, vol. 49, no. 7,

- pp 739–753, 2018.
- [10] G.H.A. van der Heijden, H.P. Huinink, L.Pel and K. Kopinga, “One-dimensional scanning of moisture in heated porous building materials with NMR,” *Journal of Magnetic Resonance*, vol. 208, no. 2, pp. 235-242, 2011.
- [11] G.H.A. van der Heijden, R.M.W. van Bijnen, L. Pel and H.P. Huinink, “Moisture transport in heated concrete, as studied by NMR, and its consequences for fire spalling,” *Cement and Concrete Research*, vol. 37, no. 6, pp. 894-901, 2007.
- [12] R.C. Reid, J.M. Prausnitz, B.E. Poling, *The properties of gases and liquids*. McGraw-Hill International, 1987.
- [13] J.G. Speight, *Formulas and Calculations for Drilling Operations*, Second ed. Scrivener Publishing LLC & Wiley, 2018.
- [14] K. Kopinga and L. Pel, "One-dimensional scanning of moisture in porous materials with NMR," *Review of Scientific Instruments*, vol. 65, no. 12, pp. 3673-3681, 1994.
- [15] L. Pel, P.A.J. Donkers, K. Kopinga and J.J. Noijen, “ $^1\text{H}$ ,  $^{23}\text{Na}$  and  $^{35}\text{Cl}$  Imaging in Cementitious Materials with NMR,” *Applied Magnetic Resonance*, vol. 47, no. 3, pp 265–276, 2016.
- [16] R. Kockegey-Lorenz, A. Buhr, D. Zacherl, B. Long, S. Hayashi, and J. Dutton, “Review of Matrix Aluminas for Refractory Formulations,” *Proceedings of the Unified International Technical Conference on Refractories*, Kyoto, 2011.
- [17] J. Canon and T. Sander, “New Test Method for Evaluating Permeability of Refractory Castables,” *Refract. Appl.* vol. 2, no. 1, pp. 6–7, 1997.
- [18] N. Schmitt, J.F. Hernandez, V. Lamour, Y. Berthaud, P. Meunier and J. Poirier, “Coupling between kinetics of dehydration, physical and mechanical behaviour for high alumina castable,” *Cement and Concrete Research*, vol. 30, no. 10, pp. 1597-1607, 2000.
- [19] W.N. dos Santos, “Effect of moisture and porosity on the thermal properties of a conventional refractory concrete,” *Journal of the European Ceramic Society*, vol. 23,



- no. 5, pp. 745-755, 2003.
- [20] G. Routschka, "Thermal Conductivity of Refractory Castables," *Interceram*, vol. 37, pp.1-6, 1988.
- [21] C. Ribeiro, M.D.M. Innocentini and V.C. Pandolfelli, "Dynamic Permeability Behavior during Drying of Refractory Castables Based on Calcium-Free Alumina Binders," *Journal of the American Ceramic Society*, vol. 84, no. 1, pp. 248-250, 2001.
- [22] M.D.M. Innocentini, M.G. Silva, B.A. Menegazzo and V.C. Pandolfelli, "Permeability of Refractory Castables at High Temperatures," *Journal of the American Ceramic Society*, vol. 84, no. 3, pp. 645-647, 2001.
- [23] K.A. Landman, L. Pel, E.F. Kaasschieter, "Analytic modelling of drying of porous materials," *Mathematical Engineering Industry*, vol. 8, no. 2, pp. 89-122, 2001.
- [24] L. Pel, K.A. Landman, and E.F. Kaasschieter, "Analytic solution for the non-linear drying problem," *International Journal of Heat and Mass Transfer*, vol. 45, no. 15, pp. 3173-3180, 2002.



---

## Chapter 4: Influence of pore structure on vapour transport

---

### Abstract

In this study, we investigate the one-dimensional drying behavior of microsilica gel-bonded low- and non-cement castables (LCC/NCC) in the temperature regime of first-drying (100-300 °C). Specifically, the influence of permeability-enhancing agents (fibers and MIPORE 20) is explored in order to assess their added effects on the drying schedules. By subtracting or adding these agents to the material formulation step, we are able to control the dry-out behavior i.e., progression of the boiling front temperature. To this end we employ a specialized high-temperature Nuclear Magnetic Resonance (NMR) setup capable of continuously measuring moisture and temperature profiles on 74 mm-long cylindrical samples, without interrupting the sample. Our results demonstrate that incorporation of fiber and MIPORE 20 significantly alters the dry-out behavior. In particular, it can be seen that as the fibers begin to melt there is a noticeable increase in permeability which results in faster drying, as well as a decrease of the drying front temperature and therefore the generated maximum pressure.

## 4.1 Introduction

In Chapter 1, we introduced high-alumina castables as they are used in the refractory lining of hot ladles around 1000-2000 °C, where the castables need to be slowly pre-dried (typically 24 hours at less than 1 °C/min) in order to release the water as pressurized steam prior to taking the ladles into full service. It was seen that in some instances the castable's internal pore vapour pressure exceeds mechanical thresholds that may destroy the refractory matrix structure, thereby resulting in dangerous explosive spalling. This physical disintegration often occurs in the temperature regime of first-drying (100-300 °C), where moisture is released in a combined process of (i) evaporation and (ii) dehydration [1].

Over the past few decades, the quality of commercial calcium alumina- and hydratable-alumina bonded castables has considerably increased, resulting in lower water demand and binder content, less porosity and greater strength. Unlike regular castables (RC), the newer generation of low- and non-cement castables (LCC/NCC) require slower drying schedules to accommodate the aggressively high vapour pressures. Consequently, these conservative heating rates result in longer downtimes. Furthermore, fixing important parameters like the curing time, temperature and mixing program is critical to assuring microstructural consistency of the refractory matrix. Therefore, there is a growing demand for exploring alternative material recipes that can retain the optimum properties of castables, while controlling the dry-out time.

The use of microsilica gel-bonded castables instead of colloidal silica- has several advantages in this regard. Some of these promising qualities include: mixing by only adding water to the dry components; excellent shelf life; and relatively fewer hydrate phases as compared to cement-bonded systems. As compared to colloidal silica bonded castables, microsilica gel-bonded castables offer comparatively better strength and shorter setting time [2]. Furthermore, the use of organic fibers, which are known to melt before 200 °C, offer additional permeable pathways for the steam to evacuate fast enough. However, up until this point, there have been no available techniques capable of directly observing the local effects of these material adjustments on the transport dynamics of castable dry-out, i.e., quantitative measurements of the moisture distribution.

A high-temperature Nuclear Magnetic Resonance (NMR) setup has been constructed and presented, demonstrating that spatially resolved moisture content profiles can be simultaneously measured along with temperature profiles on the first drying of high-cement regular castables (RC) [3][4]. Since NMR is highly sensitive to hydrogen nuclei, the signal can be directly related to the liquid moisture content. With NMR, the sample does not need to be moved or interrupted throughout an experiment thereby allowing for continuous measurement time during heating.

The research literature has tended to focus on a variety of low- and non-cement castables (LCC/NCC) with adjusted material properties: curing time, water-to-binder ratio and effective additives, i.e., accelerators, dispersing agents, etc [5]. However, regardless of the material of choice, all the dry components are usually impregnated with polypropylene fibers (PP) to promote escape of moisture at higher temperatures.

Furthermore, there is still a growing demand for improved experimental techniques capable of directly quantifying local features of drying; preserving sample dimensions; and providing direct insight into physical phenomena resulting from fiber burn-out e.g. escape of vapour, boiling front, etc. [6][7][8]. The effect of fiber addition on drying behavior of castables has demonstrated that the amount and type of fiber used (e.g. polypropylene, polyethylene terephthalate) can affect the drying rate and mechanical properties (e.g. reinforced strength) of the castable [6][9][10]. A new permeability enhancing active compound, MIPORE 20, has also been introduced into the market. This material is composed of powdered mineral phases, with a structural form that changes upon heating. Unlike the typical crystalline phases associated with calcium aluminate hydrates, MIPORE is supposed to generate gel hydrate phases that lose their water before 150 °C [11][12][13][14]. However, there is not much literature on the subject that characterizes the behavior of this active compound. In this study, we aim to investigate the effects of both fiber- and MIPORE-addition on dry-out behavior, i.e., moisture distribution, in particular. Therefore, we have chosen a fiber-free reference material and compared it with the drying profiles of fiber-containing products, with the same water-to-binder ratios. To explore the effects of MIPORE on drying, we have chosen to compare it to a MIPORE-free reference material. This material was selected because it is a standard choice used in industry, as well as being a low permeability material.

The castables used here are Tabular Alumina based generic model systems. In detail, a low-cement castable (LCC) and a microsilica gel-bonded NCC were chosen. In order to control the influence of permeability on dry-out characteristics, polypropylene fibers are considered in this study. For MIPORE, we have decided to compare it to an LCC Fume-containing reference material. The drying behavior is quantified via the moisture boiling front speed and corresponding temperature at the front. Based on this temperature, the saturated vapour pressure can be calculated according to the Antoine equation. However, we will first briefly describe the experimental setup, followed by an example of a combined measurement of the moisture and temperature development in a regular castable. Finally, we will discuss the measurement on fiber-free and fiber-containing gel-bonded LCC and NCC, as well as a MIPORE-free and MIPORE-containing LCC Fume castable.

## 4.2 Experimental Setup

In this study, one-sided heating of castables is performed using a specialized home-built high-temperature Nuclear Magnetic Resonance setup [3][4]. NMR is a magnetic resonance technique whereby the signal can be made sensitive to only water and therefore proportional to the moisture content. This technique is best known for its application in hospitals. An extensive description of NMR is out of the scope of this article and can be found elsewhere e.g. in [15][16]. A detailed schematic of this setup is shown in Figure 4.1. For the intended purpose of this study, the experimental configuration employs a whole-body 1.5 T MRI magnet (Intera, Philips). For sending the RF pulses and receiving the NMR signal, a home-built, low-pass Birdcage coil was designed, built and tested; we can achieve pulse times as short as 50  $\mu$ s. The conducting elements of the birdcage coil enclose an Al<sub>2</sub>O<sub>3</sub> tube, i.e., the sample holder, which can tolerate temperatures above 1000 °C. Therefore, the setup can withstand ceramic temperatures without risking any damage to the equipment. Furthermore, two larger circular coils, oriented in an anti-Helmholtz configuration, generate the magnetic field gradient for 1D imaging. With a calibrated strength of 80 mT/m, this uniform gradient allows for one-dimensional slice imaging without physically moving the sample. Under these settings, we can achieve a 1D spatial resolution on the order of 2-3 mm. Furthermore, a diametrically adjustable Faraday cage for tuning/matching of the Birdcage coil is secured around the primary coil. This Faraday cage should also protect the superconducting magnet of the wholebody MRI in the case of explosive spalling.

In order to perform quantitative measurements of the moisture loss, a shielding coil has been carefully interjected between the sample and birdcage coil, which allows us to minimize the effects of changes in the dielectric constant throughout a first-drying experiment [3][4][17][18].

The cylindrical samples themselves are placed inside Teflon beakers and wrapped with rock wool, so as to prevent moisture and heat loss, respectively, whereas only one surface is exposed toward drying and external heating. Hence we create a 1D heat and moisture flow experiment for studying the dryout of castables. For the purpose of measuring temperature profiles, each cylindrical sample is prepared with 6 K-type thermocouples positioned according to a template scale. The heat source itself is supplied by a circular array of gold-coated 100 W halogen lamps, which can heat the surface up to temperatures of 200-300 °C. The maximum deliverable heat flux and heating rate is 3.5 kW/m<sup>2</sup> and 2 °C/minute, respectively. The lamps were gold-coated, as gold has a high infrared reflectivity of 0.98.

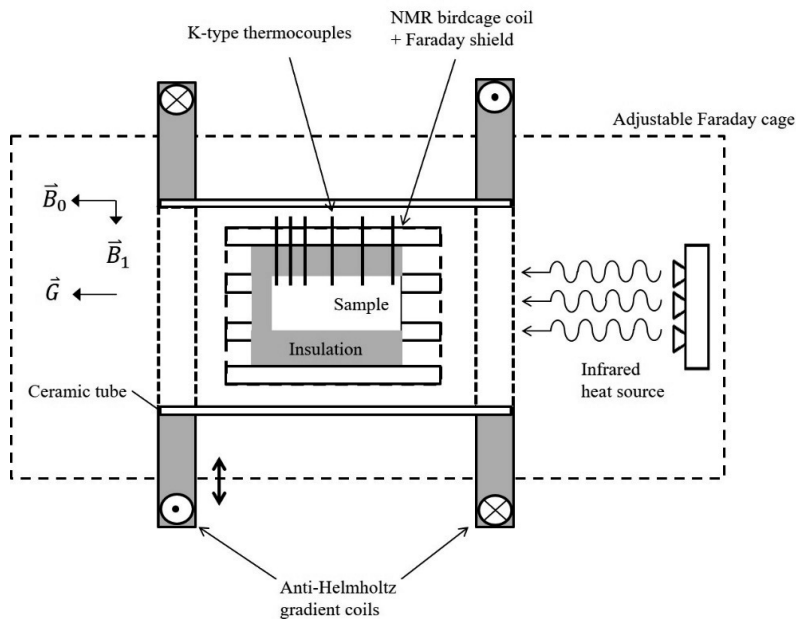


**Figure 4.1:** Schematic of the high-temperature experimental setup for measuring the moisture profiles during heating up. The sample is placed inside the birdcage coil, secured by an aluminum oxide ceramic tube. The K-type thermocouples are placed inside the holes of the sample. The insert is enclosed by a Faraday cage for tuning/matching. The heat source, i.e., an array of 100 W halogen lamps, is positioned at the end of the coil, providing a heat flux of 3.5 kW/m<sup>2</sup> and maximum average heating rate of 2 °C/minute.

### 4.3 Sample Preparation

For this study, the chosen materials of investigation are one generic, Tabular Alumina based castable; one Low Cement Castable (LCC), one microsilica gel-bonded Non-Cement Castable (NCC), one silica Fume-containing Low Cement Castable (LCC Fume) and one Regular Castable (RC), where the formulation recipe is shown in Table 4.1. The premixed dry components and binder are supplied by the manufacturers (ELKEM, Almatix and Imerys Aluminates). The only additional component for the gel-bond castables is liquid H<sub>2</sub>O, 4.35 % by dry mass. The materials are mixed, casted and cured in the laboratory for 24 hours at 20 °C. The mixing program is as follows: dry (1 minute) and wet (4 minutes) at low speed 1 with a Hobart mixer. This fixed formula guarantees homogenous dispersion of the matrix components. To achieve optimum densification of the porous structure, the samples are furthermore casted into moulds with mechanical vibration at an amplitude of 0.50 mm. This formula is applied upon advisement from the commercial suppliers.

**Table 4.1:** Materials recipe list of RC, LCC and NCC that were investigated in this study. The dry components (excluding PP fiber/M-ADS 1/M-ADW 1) add up to 100 percent (%) as indicated under the material label in the first row of the table; the calcium alumina phases are denoted by CA; microsilica 971U corresponds to Fume and the silica-bonded systems. The water demand is taken as a percentage (%) of the dry components.

	RC (%)	NCC-REF (%)	NCC-PP (%)	LCC-REF (%)	LCC-PP (%)	LCC Fume MIPORE (%)	LCC* Fume (%)
Microsilica 971U		5	5	6.3	6.3	3	3
CA-14		0.5	0.5	5	5		
CA-SECAR 71	20					2.5	5
TA 0-6mm	80	82.5	82.5	82.5	82.5	82	82
Calcined alumina fines	---	9	9	5.2	5.2	10	10
MIPORE 20	---	---	---	---	---	2.5	---
SioxX-Zero	---	3	3	1	1	---	---
PP-fiber	0.08	---	0.05	---	0.05	---	0.08
Water (% dry basis)	9	4.35	4.35	4.35	4.35	4.7	4.7

\*1% additive (M-ADS 1/M-ADW 1) was required for LCC Fume (MIPORE-free).

For the purpose of creating a 1D heat flow experiment, the wet samples are cast into cylindrical Teflon beakers. The hardened samples are themselves 74 mm x 74 mm. Furthermore, the beakers are radially pre-drilled with holes according to a template scale,



then plugged half-way with Teflon needles while the materials are still wet. The position of the holes from front to back are: 7, 27, 44, 56, 64 and 71 mm. After 24 hours, the needles are removed so that K-type thermocouples can be appropriately anchored into the holes for temperature profile measurements. The holes, with the thermocouples inside, are furthermore plugged with Teflon tape in order to prevent a pressure leakage.

Since we want to assess the influence of fiber burn-out on drying behavior, a fiber-free gel-bonded LCC reference sample (LCC-REF) and NCC reference sample (NCC-REF) have both been selected and compared with fiber-containing samples from the same family of materials. The water-to-binder ratio remains constant, while the fiber content is variable. The same approach was taken with LCC Fume MIPORE, for the purpose of comparing it to MIPORE-free LCC Fume.

#### **4.4 Moisture Loss During First-Drying as determined by NMR**

As a reference, we will first discuss the drying behavior of a regular castable, as measured by NMR. Next, the drying of Fume-containing and microsilica gel-bonded castables will be discussed. Finally, the influence of fibers and MIPORE on the drying behavior will be explored.

##### **4.4.1 Regular Castables**

As a starting material, we demonstrate moisture and temperature profiles with a Regular Castable (RC) that has been cured for 48 hours at 20 °C. This material has a high binder content (20 % wt.) and water demand (9 % wt.). Due to the relatively short sample length of 74 mm, the total timescale of an experiment is around 6 hours. In Figure 4.2B, the measured temperature profiles are shown, which demonstrate the conventional techniques of evaluating moisture loss in a first-drying experiment, i.e., where only the heat distribution across the sample is observable. The front of the sample, where the surface is exposed to the heat flux, corresponds to 0 mm. The sample average heating rate is on the order of 1 °C/minute.

As can be seen, once the heat flux is applied the temperature at the surface begins to rise rapidly and a temperature gradient starts to develop. This process goes on until 100-120 °C, the point at which liquid water transitions into vapour, i.e., the boiling of water begins. From this point on the temperature rise slows down as more energy is required to evaporate the moisture, i.e., the latent heat of vaporization is 2257 kJ/kg. As the surface reaches a temperature on the order of 180 °C, a decrease in the heating rate can be observed.

In Figure 4.2A the corresponding saturation profiles are shown, demonstrating that the spatially resolved moisture distribution can be directly measured with NMR. In this way, the moisture content is non-destructively and continuously measured as a function of time. The time in between two successive profiles is an average of 3 minutes. Each subsequent profile is divided by an isothermal reference profile taken at the beginning of the measurement at room temperature, which allows for eliminating sample inhomogeneities. Therefore, the first profile corresponds to a degree of saturation of 1.

When the heat is first turned on during the initial temperature increase up to about 70 °C in 30 minutes, a temperature gradient begins to develop. We observe that as the temperature gradient progresses, an increase of the moisture content can also be seen, i.e., a moisture front correlates with the temperature increase. Here, the final moisture content rises 8 % above the initially saturated state of 1. This initial moisture rise corresponds to the transforming hydrated compounds, which display structural properties that evolve with time and temperature [3]. Due to this process, the hydrates lose their water molecules.

Once the temperature crosses 70 °C, fast drying of the material is observed until the saturation reaches a constant level of 0.5. In this second stage of drying, both the external boundary conditions at the material surface, such as humidity and heat, and hydrate conversion are the determining factors of the speed of drying. This *externally limited* drying persists until the boiling point of water at 1 bar has been reached. However, once the temperature crosses 70 °C and climbs to 90 °C, the metastable hydrates undergo degradation into the more stable crystalline phase through a multistep reaction series; or dehydrate into structurally less stable forms [19][20]. This transformation can be observed as a locally generated moisture peak that quickly travels from the front toward the back of the sample as the sample is drying.

The source of this moisture peak can be further explained by considering that the saturation content at this position is within a temperature range of 80-90 °C. It was previously found that in this temperature range the pore structure is drastically changing as the water mobility is increasing [3]. Furthermore, the behavior of this moisture peak is a linear function of time, with a characteristic speed that is an order of magnitude larger than the capillary flux required for liquid transport across the sample (see Figure 4.2). Therefore, it is likely that dehydration is a source of water enrichment that is supplying the local moisture content faster than it can migrate toward the surface of the material.

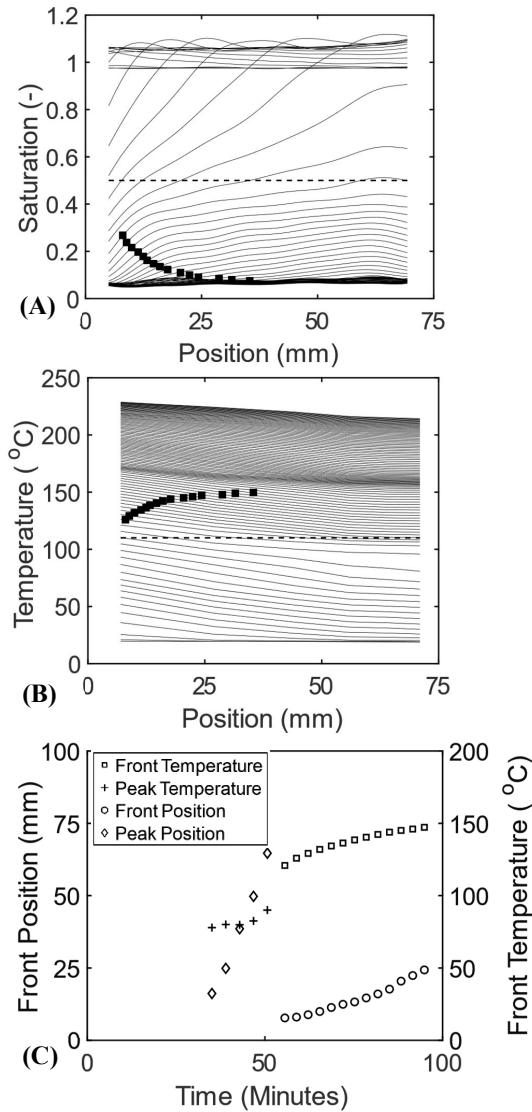


**Figure 4.2:** (A) The measured saturation profiles for RC measured at the same time as the temperature profiles with K-type thermocouples. (B) The measured temperature profiles for RC as a function of time by NMR. (C) The plotted boiling front/moisture peak position and front/moisture peak temperature as a function of time. The sample was cured for 48 hours at 20 °C. The black markers indicate the boiling front position (A) and front temperature (B). The time between subsequent profiles is 3 minutes and the profiles were measured for a total duration of 6 hours. However, the drying front disappears only after 2 hours. The dashed line corresponds to the critical moisture content.

As the moisture reaches an almost constant saturation of 0.5, we observe a transition toward the internally limited period of drying. This moment corresponds to the critical moisture content, where now the liquid clusters have broken up and are no longer in a state of percolation. At the same time the temperature at the surface has risen to around 100-120 °C and this drying front will correspond to the boiling front entering the material. As can be seen, the drying slows down as the progress of the boiling front is mainly determined by vapour transport toward the top of the sample and hence depends on the properties of the pore structure e.g. permeability.

We can characterize the position of the drying front by taking the midpoint along the liquid-vapour boundary as indicated by the square markers in Figure 4.2A. Accordingly, the corresponding temperature at the front position is also shown in Figure 4.2B by the black markers. In Figure 4.2C we have plotted both the front position and front temperature as a function of time. As can be seen in both cases, an approximately linear increase as a function of time is observed in the drying behavior up to 100 minutes.

Between 100-200 minutes into the experiment, the total measured moisture content rises by about 2 %. In Figure 4.3A we have plotted both the average saturation content and temperature as a function of time. As can be seen, there is a minor shoulder in the average moisture content just after 100 minutes and decreases after 200 minutes. In order to verify that this minor rise in the moisture content is physical, we have also plotted the local temperature rise and moisture content as a function of time for the middle of the sample (37-40 mm), as shown in Figure 4.3B. Indeed, it is clear that the moisture content is still rising within the same time frame of 100-200 minutes.

Furthermore, it is in this same window of time that the temperature begins to stagnate at 150-190 °C, as indicated by the vertical dashed lines in Figure 4.3. This temperature stagnation corresponds with a densification of the temperature profiles and is also associated with a decreased sample heating rate. In Figure 4.3C we have plotted the temperature and rate of change of temperature as a function of time. Here, we see that the heating rate certainly dips between 100-200 minutes. The source of the moisture rise is not exactly understood at the moment. However, it has been noted in the literature that in this temperature range dehydration of chemically bonded water is likely to take effect, thereby consuming energy [20]. Furthermore, it has been found for various regular castables elsewhere that the specific

heat capacity reaches a maximum value around 200 °C, which is consistent with the argument that dehydration is occurring at this point in time where the temperature is 150-190 °C [21].

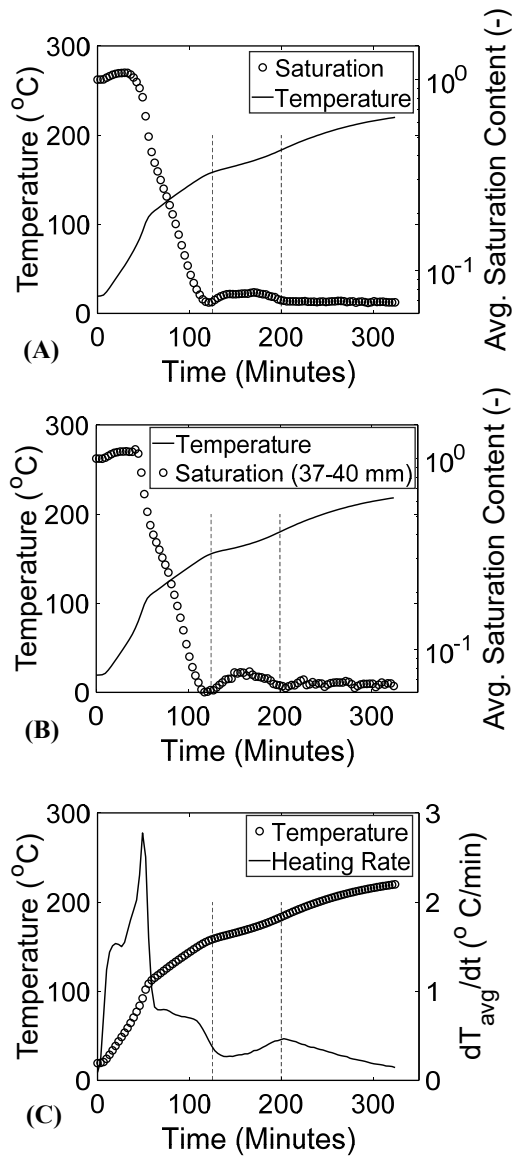


**Figure 4.3:** (A) Plot of the average saturation content and average temperature as a function of time based on the measured moisture and temperature profiles of RC. (B) A plot of the average local saturation content (depth of 37-40 mm) and average temperature as a function of time based on the measured moisture and temperature profiles of RC. (C) A plot of the average temperature and rate of change of temperature as a function of time based on the measured temperature profiles of RC. The vertical dashed lines correspond to the 150-190 °C region where a shoulder in the moisture content is observed.

At the end of the experiment, above 200 °C, the final moisture profiles are relatively flat and cluster in the same region at a saturation level of 2-5 %, until the end of the experiment. At the same time, the temperature slowly increases onto 240 °C. Indeed, placing a sample in a high-temperature furnace up to 1000 °C, after an NMR experiment, reveals that there is more water to be released. As previously shown, this is most probably a residual background level corresponding to free moisture still trapped inside small, isolated pores [22]. While the boiling point does in principle depend on pore size, previous investigations with mesoporous media revealed that even ultrashort length scales of 2-4 nm will have negligible influence on the boiling temperature [23]. Therefore, permeability is still the controlling factor.

In order to gain a more fundamental understanding of why the heating rate slows down and levels off toward 240 °C, we will present a 3D simulation of the heat transport taking place in our sample. A 3D simulation of the temperature profiles will allow us to visualize how the temperature is distributed in space and time  $T(x,t)$  across the sample, thereby providing access to important features such as the temperature gradient or the distribution of heat at the boundaries of the sample.

#### 4.4.2 Heat Transport in Castables

For our simulation of heat transfer, we will consider a 3D cylindrical geometry in which the sample is insulated with wool that is used in our actual experiments (see Figure 4.4A). The purpose of this simulation is only to understand how heat is being distributed across our sample in the experiments. The length of our geometry is 90 mm and the radius is 55 mm; thickness of the insulation is taken to be 20 mm in the simulation model.

For our 3D problem, the heat transport process is described by the well-known Fourier heat equation, without consideration of internal chemical changes occurring within our sample ( $Q_{\text{int}} = 0$ ). Moisture transport is excluded since in this higher temperature range the sample has already dried out [22]. Furthermore, there is no bulk transport of heat by any fluid body, i.e., no convective liquid water flux. Heat is transferred purely by conduction, slowly, via the dried, solid castable structure. Defining the temperature as  $T$ , it follows that:

$$\rho C \frac{\partial T}{\partial t} + \nabla \cdot (k \nabla T) = 0 \quad (4.1)$$

Here,  $\rho$ ,  $C$  and  $k$  correspond to the material density, specific heat capacity and thermal conductivity, respectively. Eq. (4.1) applies to both the solid material of our sample as well as the insulation material preventing heat losses. In an ideal scenario where the energy

supply is being entirely utilized toward the heating of our sample, there is no heat flux between the insulation and outside environment ( $Q_{\text{ext}} = 0$ ). In a more realistic situation, heat is radiatively lost across the insulation, where the ambient environment is fixed at room temperature. At the surface, the material is radiatively exposed to the heat flux from our heat source. Therefore, a (i) surface and (ii) insulation boundary condition exists according to the well-known Stefan-Boltzmann relation:

$$\bar{\mathbf{n}} \cdot k \nabla T = \varepsilon \sigma (T'^4 - T^4) \quad (4.2)$$

Above,  $T'$  and  $T$  correspond to the temperature of radiance (ambient surrounding or heat supply) and the material (insulation or sample surface), respectively.  $\varepsilon$  is the material-dependent emissivity and  $\sigma$  the Stefan-Boltzmann constant. The time window between each profile is 20 minutes and the total simulation time is 300 minutes. A list of physical parameters is listed in Table 4.2. The simulation was implemented in COMSOL Multiphysics.

**Table 4.2:** List of physical parameters for the 3D heat transport simulation on our RC sample as implemented in COMSOL Multiphysics. These values are taken for dried out samples.

Simulation Parameters	RC Sample	Insulation Layer
Thermal Conductivity (W/m K)	2.77	0.035
Specific Heat Capacity (J/Kg K)	900	840
Density (kg/m <sup>3</sup> )	2850	60
Emissivity (-)	0.5	0.9
Model Sample Dimensions	70 mm x 70 mm	20 mm

In Figure 4.4B we have plotted the average temperature increase of the sample as a function of time for both the simulation and the experiment on RC. The simulation corresponds to two cases: ideal heating ( $Q_{\text{ext}} = 0$ ) and radiative heat loss to the surrounding environment in accordance with Eq. (4.2). To a first-order approximation, the average heating rate in the experiment and simulation (ideal case) is comparable. We see that the temperature rise in our simulations is also non-linear, as reinforced by the experimental data as well. The decreasing heating rate in Figure 4.4B is explained by the radiative surface boundary condition of Eq. (4.2); as the temperature of the sample surface  $T$  increases it approaches the temperature of our heat source  $T'$  and therefore the right-side of Eq. (4.2) decreases. Thus, less heat is supplied to the surface over time.

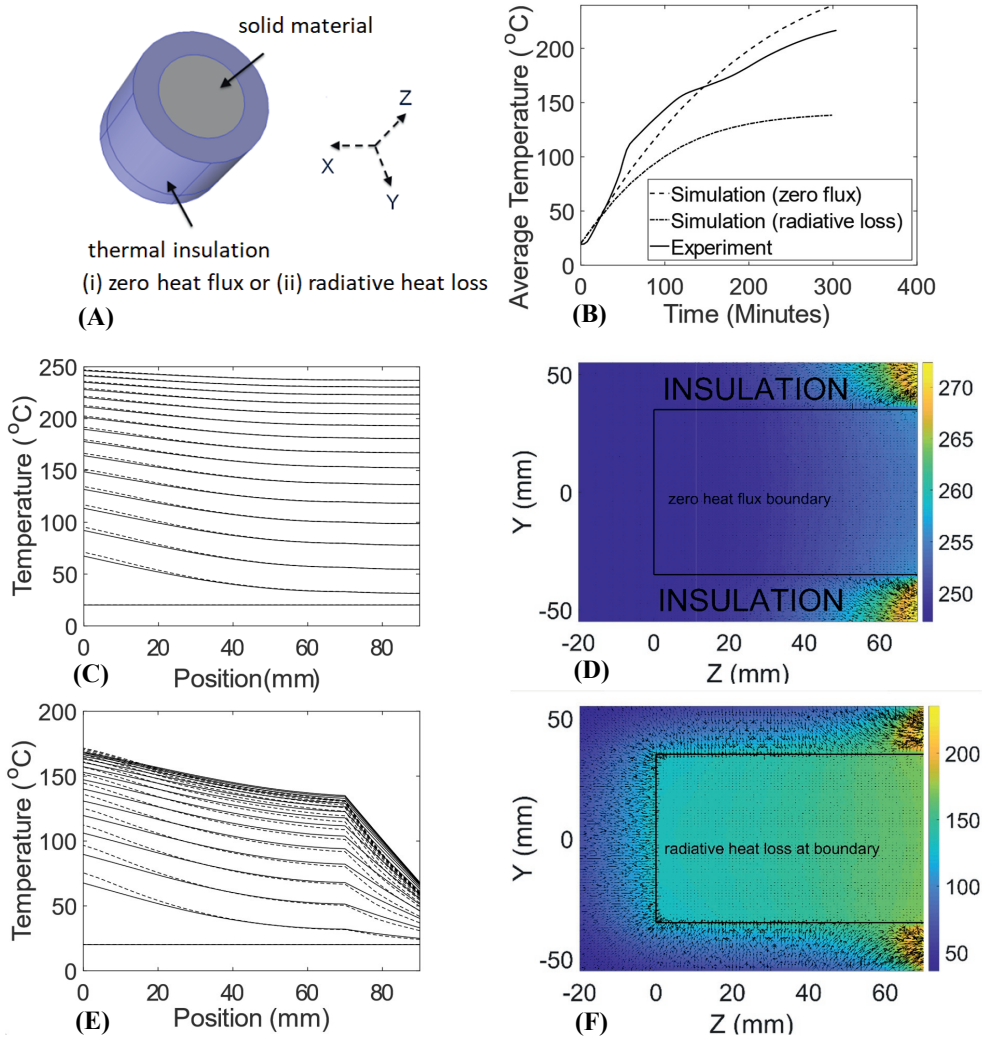


**Figure 4.4:** (A) A schematic of the 3D geometry being used in our simulation. (B) The average temperature rise as a function of time for both the measured profiles and the simulated profiles plotted together in comparison. The simulation is for two cases: zero heat loss (ideal) and radiative heat loss (non-ideal). (C) Plot of the simulated temperature profiles, for the ideal case, along the central axis and 30 mm from the central axis. (D) 2D contour plot of the ideal case at  $t = 300$  minutes. (E) Plot of the simulated temperature profiles, for the non-ideal case, along the central axis and 30 mm from the central axis. (F) 2D contour plot of the non-ideal case at  $t = 300$  minutes. The total simulation time was 300 minutes and the time between each profile is 20 minutes. The black border indicates the separation between the insulation zone and solid material zone.

The simulation for the non-ideal case, where heat is being dissipated at the insulation boundary due to radiation losses to the surrounding, reveals that there is a quantitative



discrepancy between what we predict and what we see experimentally. The maximum temperature here is just under 150 °C. However, there is qualitative agreement in the behavior of both heating rates, where again we see that at higher temperature the heating rate is decreasing due to a limited energy supply. As can be seen from the simulation, this means that more energy would be required to raise the temperatures closer to the experimental values. This makes sense since our simulation assumes that the radiative heat losses are bounded by  $T' = 20$  °C in comparison to the ideal case where all the energy is being consumed and is clearly shown in the maximum attainable temperature above 200 °C.

We also observe the heating rate of our sample to abruptly change in a way that is not captured by the simulation: there is a sudden increase from 50-100 °C followed by a decrease at 100-150 °C. This phenomenon can be due to the simplicity of our simulation, where we are excluding internal chemical and physical transformations that are occurring locally within our sample throughout a heating experiment, e.g. dehydration of chemical phases, latent heat of evaporation, etc.

In Figure 4.4C, selected temperature profiles as a function of longitudinal position and time are shown for the zero heat flux case at two locations in the radial plane (see Figure 4.4D too): (1) central axis and (2) +30 mm from the central axis. As can be seen, there is little difference between the profiles suggesting that the temperature gradient in the radial direction is insignificant compared to the longitudinal direction i.e., along the z-axis. Furthermore, for temperatures ranging from 150 °C and above, the heating rate begins to slow down as indicated by the closer proximity of the profiles. This is qualitatively comparable to the densification of our profiles in an actual experiment from 150 °C and onwards.

A 2D slice of the temperature distribution is also provided in Figure 4.4D corresponding to the geometric configuration in Figure 4.4A. This figure shows a contour plot of the final temperature profiles toward the end of the simulation at  $t = 300$  minutes for the ideal case of zero heat flux at the insulation boundary. Here, the full spatially resolved 2D temperature distribution from  $y = -55$  to  $y = 55$  mm is visualized. The rectangular solid black boundary corresponds to the division between insulation and solid material, i.e., our sample. Once again, we see that the temperature is quite uniform in the radial direction and longitudinally the distribution is comparable to the profiles from Figure 4.4C. The temperature in the insulation region is also quite high on the order of 250 °C. The direction of the temperature gradient is also represented by the arrow vectors which show that the gradient is quite steep at

the front section of the insulation layer. This is logical since Eq. (4.2) requires that the surface temperature approaches  $T'$  toward the end of the simulation, however at the same time the insulation will have a 60 % lower thermal diffusivity than the sample and will thus generate a higher surface temperature gradient.

In Figure 4.4E, selected temperature profiles as a function of longitudinal position and time are shown for the case of radiative heat loss at the boundary, at two locations in the radial plane: (1) central axis and (2) +30 mm from the central axis. Again we see little difference between the distributions along the two different axes. But there is clearly a significant difference between the temperature behavior here and that displayed in Figure 4.4C towards the back side of the sample, where the temperature is dramatically falling thereby enhancing the temperature gradient. This makes sense since we have imposed a radiative heat loss boundary condition at the insulation layer, therefore not all of the energy is going into heating up the sample. Furthermore, the maximum attainable temperature is about 170 °C. In order to raise the temperature, we would need to supply more energy from our heat source.

In Figure 4.4F, we have again plotted a 2D slice of the temperature distribution corresponding to the geometric configuration in Figure 4.4A. This figure shows a contour plot of the final temperature profiles toward the end of the simulation at  $t = 300$  minutes for the non-ideal case of radiative heat losses across the insulation boundary. Here we see the effect of the heat losses at the boundary as the temperature gradient is very pronounced within the insulation region towards the edges, in comparison to the relatively flatter profiles within the inner regions of the contour plot. Furthermore, the temperature at the surface is about 150-170 °C while the temperatures in the insulation region are around 100 °C. This near-boundary temperature is significantly lower than that displayed in the ideal case from Figure 4.4D, again reflecting the heat loss of our sample at the insulation boundary.

Therefore, to a first-order approximation, the late-behavior of the temperature profiles (150-250 °C) during the experiment can be accounted for by the decreasing supply of energy toward the surface of the sample.

4.4.3 Fiber-Free NCC and LCC

Next we have measured the drying of two micro-silica containing reference materials LCC-REF and NCC-REF, neither of which contains any fibers. The measured moisture and temperature profiles are given in Figure 4.5. Unlike RC, the initially rising moisture effect is not as pronounced in LCC-REF and NCC-REF. This is probably due to the fact that the microsilica containing materials have anywhere from four- to forty-times less calcium aluminate cement and half the water addition as compared to RC. From comparing these measurements with RC, we can see that the initial drying of NCC-REF and LCC-REF is slower; RC loses 50 % of its initial moisture content within the first 55 minutes of the experiment, where the halving of the initial moisture content for NCC-REF and LCC-REF doesn't occur for at least 90 minutes.

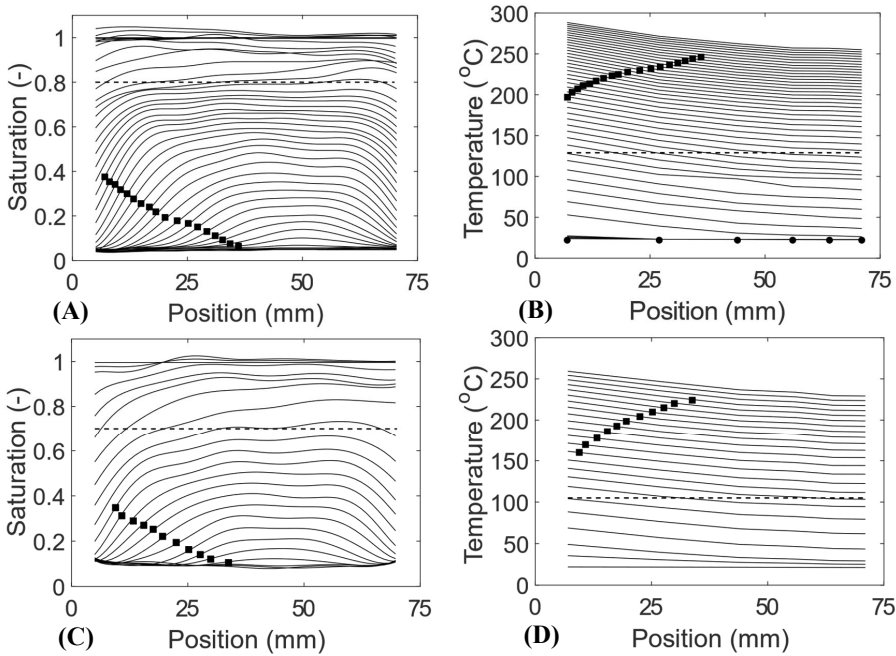


**Figure 4.5:** Measured saturation profiles as a function of time, by NMR for (A) LCC-REF and (C) NCC-REF. Temperature profiles measured at the same time as the saturation profiles with K-type thermocouples for (B) LCC-REF and (D) NCC-REF. These materials are cured for 24 hours at 20 °C. The black square markers indicate the boiling front position (A) and front temperature (B). The black round markers indicate the thermocouple positions for both (B) and (D). The time between subsequent profiles is 7 minutes and the profiles were measured for a total duration of 4 hours. The dashed line corresponds to the critical moisture content.

Moreover, the moisture profiles stay rather flat, reflecting that internal transport of moisture is much faster than drying at the surface or that internal transport of moisture is very low due to a very low permeability as compared to RC. Furthermore, the critical moisture-saturation content for both these materials is higher, i.e., 0.7 for NCC and 0.8 for LCC, in comparison to RC, which could be an indication of higher steam pressure in the pores of NCC-REF and LCC-REF.

After this critical moisture content has been reached for both materials, a boiling front begins to develop. Once more we have indicated the position of the boiling front and the corresponding temperature for both materials, where the position and temperature are plotted as a function of time in Figure 4.6. Again, a linear relation is found in the drying behavior of the front position and temperature. Moreover, as can be seen from the boiling front position as a function of time, the front of RC travels almost twice as fast as LCC-REF and NCC-REF, reflecting the denser structure of these materials. What is also quite clear from the data is that only the moisture profiles provide direct information about the boiling front. The temperature profiles alone give little information about the emergence of a boiling front.

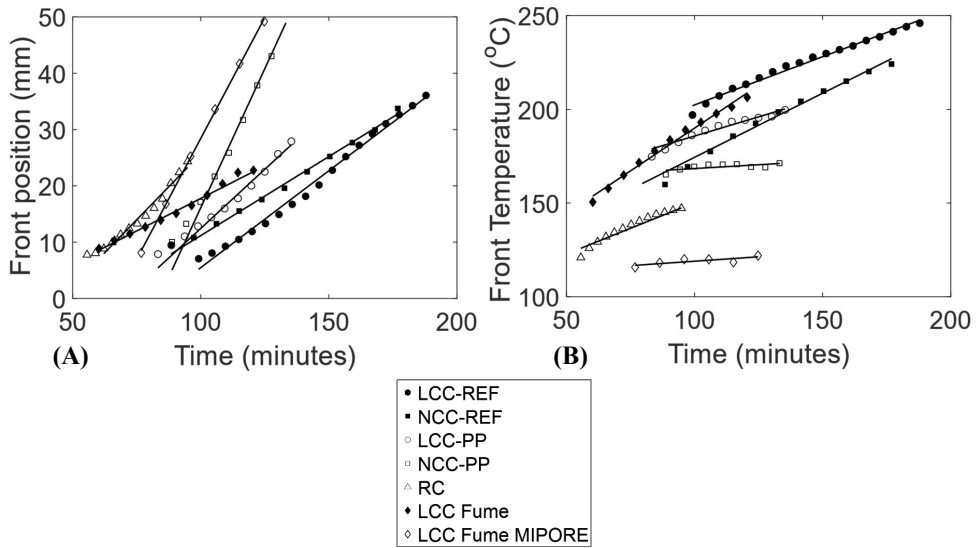


**Figure 4.6:** (A) The boiling front position and (B) front temperature as determined from the measured moisture and temperature profiles as a function of time for all materials (see also Table 4.1). The straight lines in (A) and (B) are a linear fit to the data.

The boiling front in LCC-REF and NCC-REF doesn't appear until 150 °C and 200 °C, respectively, and steeply climbs to 250 °C. Hence in this case the vapour pressures at the boiling front are approaching a maximum of 4 MPa, whereas for RC the maximum boiling front temperature and pressure is 150 °C and 0.5 MPa. These high boiling temperatures have been reported elsewhere before, where a temperature plateau associated with some endothermic process e.g. boiling, dehydration, etc. was observed [1][24]. These higher temperatures can be attributed to the lower permeability and hence higher vapour pressure needed to drive out the moisture. And, as a consequence, as the vapour pressures approach the strength of the castables, steam explosions become a more realistic outcome of the drying process (on industrial sized specimens [24]).

#### **4.4.4 The Effect of Fiber-Addition on Dry-Out**

To assess the effect of fibers on drying behavior we have prepared the same two microsilica gel-bonded reference materials LCC-REF and NCC-REF with fibers, i.e., both materials were prepared with a maximum of 0.05% PP fibers. We have first characterized the PP fibers using Thermal Gravimetric Analysis (TGA) and Differential Scanning Calorimetry (DSC). The results are given in Figure 4.7. As can be seen from TGA a dramatic drop in the mass fraction around 200 °C is observed which is in accordance with the observation of the measured heat flow with DSC. However, with DSC there is also an observed peak at 170 °C. To this end, we have additionally performed Thermal Mechanical Analysis (TMA) on the same batch of PP fibers, where the length displacement  $y$  is shown. Here it can be seen that the observed 170 °C peak from DSC is associated with the fibers' decreasing viscosity. However, this process is due to the melting of the fibrous crystal structure followed by oxidative thermal degradation of the polymer components at 200-220 °C, which coincides with the mass drop in TGA at the same temperature [6][25][26]. Hence, from these measurements alone we would expect the fibers to start to have a noticeable effect on the drying for temperatures beyond 170 - 200 °C. Due to the increased permeability, the generated maximum pressure and associated maximum temperature are expected to decrease.

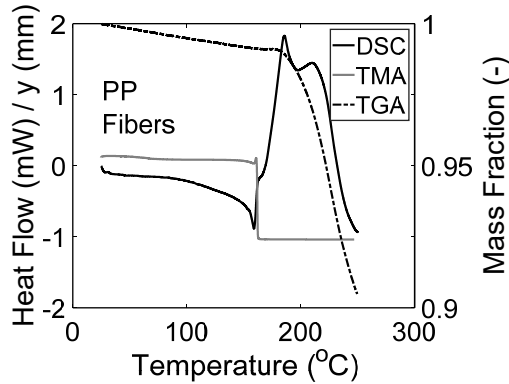


**Figure 4.7:** TGA, DSC and TMA measurements for the melting temperature of the PP fibers. The heat flow (DSC) and length displacement  $y$  (TMA) for the sample are shown together on the same left axis. The mass fraction (TGA) corresponds to the right axis.

The measured moisture and temperatures profiles for the fiber-containing LCC and NCC are given in Figure 4.8. Once again we observe the general two-stage drying process associated with externally limited and internally limited drying in the moisture profiles. However, if we look into more detail at the data, some notable differences can be observed. Initially, the drying for both fiber-free and fiber-containing materials is almost the same, which can be expected as the fibers will not exert much influence on the liquid transport. Indeed for both materials the critical saturation, which is on the order of 0.8, does not change due to the addition of fibers. It is only once a boiling front enters the material and the temperature exceeds 170 °C that we can observe a clear difference with respect to the fiber-free castables, where the materials are now drying much faster. For comparison, in Figure 4.6 we have plotted the boiling front temperature of the fiber-containing family along with the boiling front temperatures corresponding to the fiber-free materials from Figure 4.5 and RC from Figure 4.2. Especially for NCC a large effect is seen as the temperature at the boiling front only slightly increases in time, indicating the permeability has gone up considerably. Indeed, Salomao and Pandolfelli [6] also observed an increase in permeability by monitoring the air flow rates of the evolving castable pore structure throughout the temperature regime of fiber degradation. Moreover, as can be seen from the front temperature as a function of time, these measurements indicate that the effect of fiber-addition can already be observed from the moment the fiber becomes less viscous.

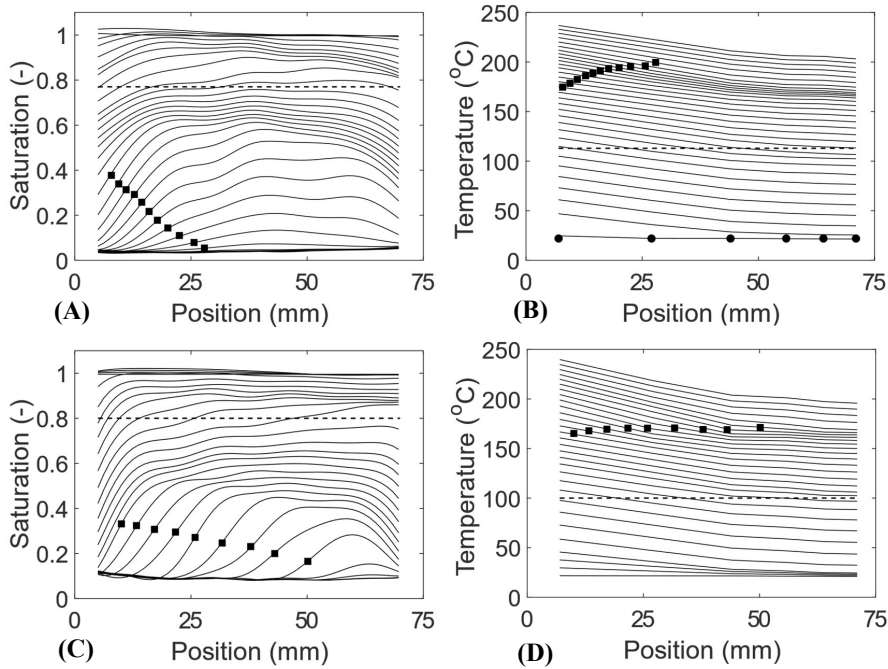


**Figure 4.8:** Measured saturation profiles as a function of time, by NMR for (A) LCC-PP and (C) NCC-PP. Temperature profiles measured at the same time as the saturation profiles with K-type thermocouples for (B) LCC-PP and (D) NCC-PP. The samples are cured for 24 hours at 20 °C. The black square markers indicate the boiling front position (A) and front temperature (B). The black round markers indicate the thermocouple positions for both (B) and (D). The time between subsequent profiles is 5 minutes and the profiles were measured for a total duration of 2.5 hours. The dashed line corresponds to the critical moisture content.

#### 4.4.5 MIPORE-Free LCC Fume

We have also looked at the drying behavior of a fume-containing, i.e., microsilica low-cement castable. This reference material is used because it is a standard formulation in the castable industry. The measured moisture and temperature profiles are provided in Figure 4.9A and Figure 4.9B. The total duration of the experiment was 2.5 hours. The time lapse in-between each profile is 6 minutes and the average heating rate is 1.3 °C/minute. Once again, we observe a difference in the initial behavior of the moisture profiles when compared to the drying of RC. For one thing, the initial rise in the moisture content seen with RC does not occur with LCC Fume. Here, it must be taken into account that LCC Fume has 4-times less calcium alumina binder than RC. Also, the first few moisture profiles of LCC Fume appear more homogeneous than RC, suggesting that the externally limited drying period is

quite uniform. However, the critical moisture content, as indicated by the dashed line, does not occur until a saturation level of 0.6 is reached, after 60 minutes, which also corresponds to a temperature of 125 °C as shown in Figure 4.9B. With RC, the critical moisture content is closer to 0.5 and the corresponding temperature is just above 100 °C. With the gel-bonded LCC/NCC, the critical moisture content is 0.8.

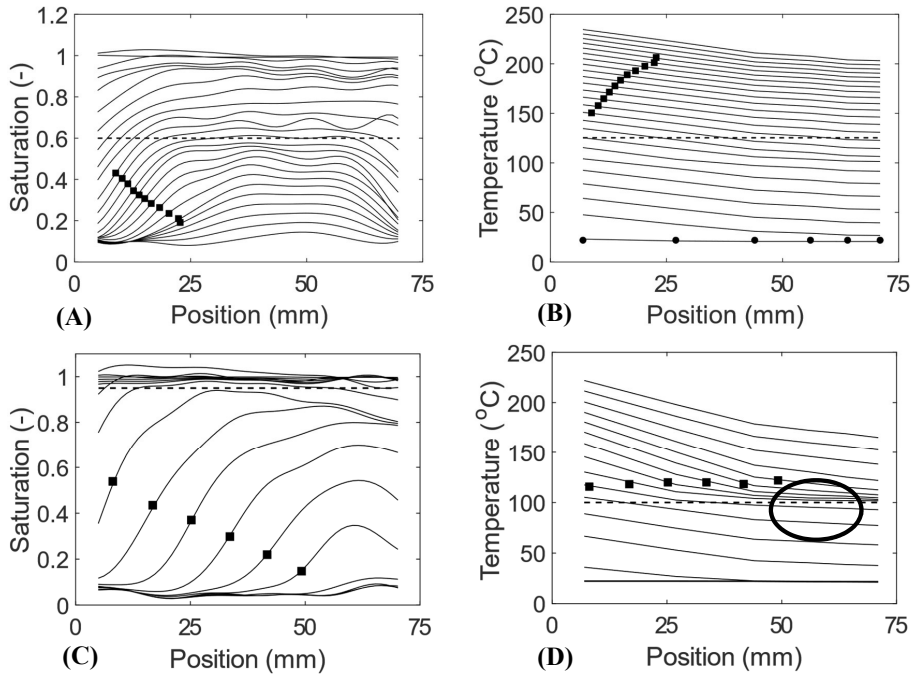


**Figure 4.9:** Measured saturation profiles as a function of time, by NMR for (A) LCC Fume and (C) LCC Fume MIPORE. Temperature profiles measured at the same time as the saturation profiles with K-type thermocouples for (B) LCC Fume and (D) LCC Fume MIPORE. The samples are cured for 24 hours at 20 °C. The black square markers indicate the boiling front position (A) and front temperature (B). The black round markers indicate the thermocouple positions for both (B) and (D). For LCC Fume MIPORE, the average time between subsequent profiles is 10 minutes and the profiles were measured for a total duration of 2.7 hours, with a heating rate of 1 °C/minute. For LCC Fume, the total duration of the experiment was 2.5 hours. The time lapse in-between each profile is 6 minutes. The dashed line corresponds to the critical moisture content for both materials. The circle in (D) corresponds to the momentary densification of the temperature profiles.

But, it is not until a moisture content of about 0.4 and temperature of 150 °C that we begin to see the appearance of the boiling front in LCC Fume that continues on until 215 °C. The position and temperature of the boiling front as a function of time have been plotted along



with the other materials in Figure 4.6. Furthermore, the functional form of this boiling front is also linear with time like the other materials. However, on the basis of the front temperature, the behavior of LCC Fume is closer to gel-bonded castables in the 150-210 °C range, indicating an equilibrium vapour pressure of 0.5 MPa – 2 MPa.

#### 4.4.6 The Effect of MIPORE-Addition on Dry-Out

To assess the effect of MIPORE on the drying behavior of LCC Fume we have replaced 50 % of the usual CA binder content with MIPORE 20 powder, a permeability enhancing active compound as shown in Table 4.1. Just as we characterized the fibers with TGA/DSC, we employed the same approach to MIPORE in order to understand its physical and morphological characteristics more clearly.

In Figure 4.10, a plot of the mass change (TGA) and heat flow (DSC) as a function of temperature is provided for anhydrous MIPORE, i.e., no water addition. As can be seen, the behavior of this compound is quite different from PP fibers. In the case of unmixed PP fibers, we have already shown that the polymer components eventually evaporate away, as demonstrated by the rapid, non-linear mass loss. However, with MIPORE, it does not seem to evaporate, which is signified by the moderate, approximately linear reduction in mass with temperature. Furthermore, DSC indicates that there is some structural change occurring in the 140-150 °C range.

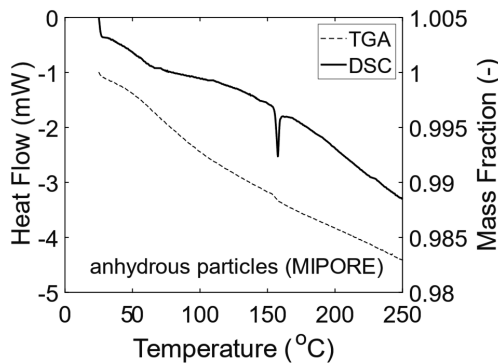


**Figure 4.10:** TGA and DSC measurements as a function of temperature on the structural change in an isolated batch of anhydrous MIPORE particles.

In order to investigate the behavior of MIPORE in the presence of water, a dry sample of powder was taken and dissolved in water with the same proportion as required by the mixing

recipe in Table 4.1, and then dried in a 130 °C oven for several days. The result was that a semi-continuous structure had emerged, which was quite different from the previous anhydrous state of fine particles that are only a few tens of micrometers in diameter. The texture of this structure is rather delicate and easily cracks under stress. The sample was furthermore taken and subjected to Scanning Electron Microscopy (SEM) imaging at different resolutions as shown in Figure 4.11 to reveal some more of these physical details.

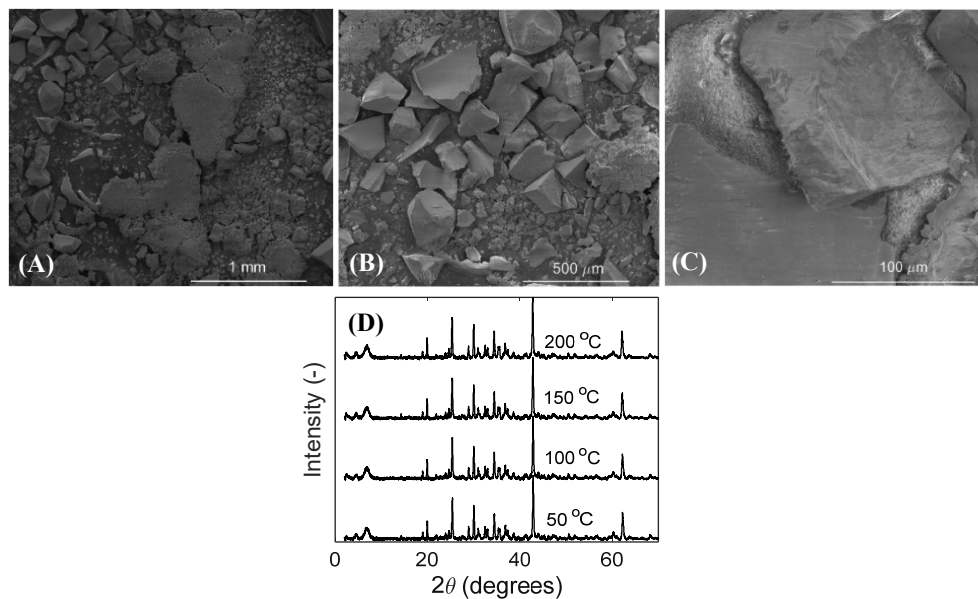


**Figure 4.11:** SEM images of the hydrated MIPORE particles after being dried for 130 °C at different resolutions of (A) 1 mm (B) 500 μm (C) 100 μm. The circle in (C) corresponds to the apparent phase differences. (D) XRD spectra for the same sample from (A-C) heated one more time from 50-200 °C.

In Figure 4.11A and Figure 4.11B, it appears there are different structural phases, i.e., some larger and tabular, others smaller and finer. In Figure 4.11C we see that at about 50-100 μm (see black circle), a form resembling some morphological-like structure is possibly identified. However, in order to verify this crystalline structure, the sample was taken and placed in X-Ray Diffraction (XRD) over a variable temperature range of 50-200 °C, as shown in Figure 4.11D. It is seen from the distinctly defined peaks in the spectrum that crystals are indeed present. What is more, the diffraction peaks remain entirely constant with temperature and do not shift at all, which can be explained by the stable nature of the mineral carrier that MIPORE uses for its active organic components. Previous XRD analysis on an actual

MIPORE-containing castable, that is activated with CA binding phases, identified non-crystalline bonding phases, particularly CA hydrated gel phases [11]. As a final observation, it should be noted that with MIPORE the particles participate in the hydration process, whereas with PP fibers they play no role in hydration.

In order to further understand the effects of MIPORE on the dry-out process, NMR moisture profiles were measured on MIPORE-containing LCC Fume, in accordance with the mixing recipe in Table 4.1. The experiment was conducted under the same conditions as the LCC Fume reference sample, where the moisture and temperature profiles are shown in Figure 4.9C and Figure 4.9D. The total experiment was 2.7 hours and the time between profiles was 10 minutes and the heating rate 1 °C/minute. As can be seen, there are extremely significant differences between this material and the reference from the previous section.

First, it is clear that the critical moisture content of 0.95 is reached almost immediately the moment the experiment begins, as indicated by the dashed line in both the moisture and temperature profiles. This is the highest observed critical moisture content of all the materials considered in this entire study. This corresponds to around 100 °C in the temperature profiles, beyond which a gradient in the moisture content appears. Then around a moisture content of 0.6, a boiling front emerges as indicated by the black markers and enters the material, along with the corresponding temperature at the front as shown in Figure 4.9.

In Figure 4.6, the position and temperature of the boiling front is plotted along with the other materials as a function of time. What is clear from the moisture profiles and the boiling front as a function of time is again the linear behavior, but also that the front is very sharp, much like LCC-PP, and appears to move at the same speed (for both position and temperature) again like LCC-PP, which is the fastest of any material considered. This sharp front, therefore, moves rapidly compared to the LCC Fume reference sample, advancing twice the maximum distance into the sample as the boiling front of LCC Fume. The low, stagnating front temperature of 120-130 °C implies that the permeability is indeed enhanced and thus the equilibrium vapour pressure is quite low around 0.1-0.2 MPa. It is also at 120-130 °C we observe a minimum in the heating rate, indicated by the momentary clustering of the profiles, before spreading out again (see black circle in Figure 4.9D). With some of the other materials, we have observed that the heating rate continues to decrease as the temperature profiles become more densely packed.

Compared to LCC-PP and NCC-PP, which have starting front temperatures at or above 150 °C, LCC Fume MIPORE loses its water below 150 °C. Therefore, its permeability opens up at lower temperatures and lower pressures. Furthermore, the fact that the temperature at the front is in the range of 100-150 °C corresponds with findings in the literature that the TGA mass loss of a MIPORE-containing castable is quite rapid within the same temperature range [11][14][27].

Furthermore, the NMR moisture profiles demonstrate that the permeability enhancement of CA-containing castables is certainly realized in the 100-150 °C temperature regime, which is more beneficial from an industrial point of view.

#### **4.5 Conclusion**

Here we have presented and demonstrated a high-temperature NMR setup that is capable of performing quantitative measurements of the moisture and temperature distribution on a series of first-drying experiments for castable materials. This experimental configuration has provided direct evidence of the effect of MIPORE 20 or PP fibers on the boiling front temperature, thereby confirming what has already been previously established in literature.

In the NMR study of moisture and heat transport processes in castables, we introduced an example material that is rich in water, i.e., RC cured 48 hours. It was found that there are three uniquely distinct stages of drying and heating: (i) evolution/or liberation of the hydrate compounds, i.e., dehydration (ii) externally limited drying and (iii) internally limited drying.

The near completion of stage (i) also revealed a fast traveling moisture peak that is probably related to dehydration of the metastable structures. After stage (iii), when the sample has fully dried, the heating rate slows down and the temperature profiles become denser. This densification of the temperature distribution can be explained on the basis of a decreasing energy supply, where radiative heat limitations are the most dominant effects governing heat transport towards the very end of the experiment. We also observe a minor shoulder in the local moisture content around 100-200 minutes, which is possibly due to dehydration around 150-200 °C. It should be kept in mind that in our experiments, we do not observe a steep temperature gradient. This is due to the physical limitations of our sample and experimental setup. Therefore, the small moisture rise at 100-200 minutes cannot be due to water migration toward the back of the sample.

An investigation into the drying properties of microsilica containing castables reveals the effects of adding fibers to the castable formulation procedure. In all cases, we observe two drying stages: (1) a rapid, externally limited drying process that depends on the surface boundary conditions of the material and (2) internally limited drying, which is intrinsically determined by the pore structure of the materials. In the latter case, a boiling front develops and enters the pores of the material.

Formulating the materials without PP fiber addition causes the boiling front temperature to rise up to 250 °C under the applied boundary conditions, yielding a high pressure of 4 MPa which is within the range of the material's mechanical strength. However, adding fibers to the mix will decrease the maximum boiling front temperature and pressure to about a maximum of 200 °C and 1 MPa, respectively. This is consistent with the TGA/DSC/TMA results, which indicate that the fiber viscosity begins to decrease as it starts to melt around 180-200 °C thereby increasing the permeability and opening up pathways for the vapour to escape. Furthermore, fiber-addition does not significantly affect the initial liquid transport at the start of the drying process nor the critical saturation content for different materials, because the functions of the fiber are only relevant to the vapour permeability, i.e., fibers promote easy escape of vapour and they do not interact with the hydration process, in the first place.

In the case of LCC Fume MIPORE, we see that there is indeed a very pronounced difference in the drying behavior between the reference LCC Fume (MIPORE-free) and LCC Fume MIPORE-containing castables. While the boiling front temperature starts at 120 °C, it barely increases to a higher temperature throughout the duration of the experiment corresponding to a low vapour pressure of 0.2 MPa, demonstrating that moisture is evacuated from the material at lower temperatures than PP-containing castables. However, the physical and structural properties of MIPORE are more complex than PP. While PP has a polymer network that burns out and evaporates at higher temperatures, MIPORE plays an active role in the hydration process of a calcium aluminate bonded castable.

#### 4.6 References

- [1] D.A. Bell, "First Heat-up of Ladle Linings," *Proceedings of the Unified International Technical Conference on Refractories*, Berlin, Germany, 1999.
- [2] B. Myhre, H. Peng, "Why do industrial-sized no-cement castables sometimes explode during heat-up? A remedy to ensure safe and fast heat-up of microsilica-gel bond castables," *Proceedings of the 53<sup>rd</sup> Annual Symposium on Refractories from the American Ceramic Society*, pp. 43–56, 2017.
- [3] A.J. Barakat, L. Pel and O.C.G. Adan, "One-dimensional NMR imaging of high-temperature first-drying in monolithics," *Applied Magnetic Resonance*, vol. 49, no. 7, pp. 739–753, 2018.
- [4] G.H.A. van der Heijden, H.P. Huinink, L.Pel and K. Kopinga, "One-dimensional scanning of moisture in heated porous building materials with NMR," *Journal of Magnetic Resonance*, vol. 208, no. 2, pp. 235-242, 2011.
- [5] P. Pilate, J. Tirlocq and F. Cambier, "Refractory Castables: an Overview," *Process Engineering*, vol. 84, no. 6, pp. 43-49, 2007.
- [6] R. Salomão, L. R. M. Bittencourt, V. C. Pandolfelli, "Drying additives for refractory castables: Aluminum powder and polymeric fibers," *Cerâmica*, vol. 54, no. 330, pp. 259-267, 2008.
- [7] M.D.M. Innocentini, C. Ribeiro, R. Salomao, V.C. Pandolfelli and L.R.M. Bittencourt, "Assessment of Mass Loss and Permeability Changes during the Dewatering Process of Refractory Castables Containing Polypropylene Fibers," *Journal of the American Ceramic Society*, vol. 85, no. 8, pp. 2110-2112, 2002.
- [8] R. Salomao and V.C. Pandolfelli, "Polypropylene Fibers and their Effect on Processing Refractory Castables," *International Journal of Applied Ceramic Technology*, vol. 4, no. 6, pp. 496-502, 2007.
- [9] R. Salomao and V.C. Pandolfelli, "Drying Behavior of Polymeric Fiber-Containing Refractory Castables," *Journal of the Technical Association of Refractories (Japan)*,

- vol. 24, no.2, pp. 83-87, 2004.
- [10] C.M. Peret, R. Salomão and V.C. Pandolfelli, "Polymeric Fibers as Additives for the Drying of Refractory Castables," *Journal of the Technical Association of Refractories (Japan)*, vol. 24, no. 2, pp. 88-92, 2004.
- [11] C. Wohrmeyer, J.M. Auvray and C. Zetterstrom, "Dry Out of Dense Refractory Castables via Use of Permeability Enhancing Active Compound," *Proceedings of 59th International Colloquium on Refractories*, Aachen, Germany, pp. 40-44, 2016.
- [12] C. Zetterstrom, J.M. Auvray, C. Wohrmeyer and C. Parr, "Enhanced permeability for a rapid dry-out of refractory castables," *Proceedings of the Unified International Technical Conference on Refractories*, Vienna, Austria, pp. 1-4, 2015.
- [13] J.M. Auvray, C. Zetterstrom, C. Wohrmeyer, C. Parr and F. Kebli, "The impact of permeability for a rapid dry-out of refractory castables," *Proceedings of the Unified International Technical Conference on Refractories*, Vienna, Austria, pp. 1-4, 2015.
- [14] C. Wohrmeyer, P. Edwards and C. Parr, "Raw Material Innovations- a Key Success Factor in a Fast Changing Refractories World," *Refractories Worldforum*, vol. 9, no. 4, pp. 89-93, 2017.
- [15] M.T. Vlaardingerbroek and J.A. Den Boer, *Magnetic Resonance Imaging Theory and Practice*. Springer, Berlin, Heidelberg, 1996.
- [16] L. Pel and H.P. Huinink, "Building Materials Studied by MRI," in *Encyclopedia of Magnetic Resonance*, vol. 1, no. 4. John Wiley & Sons, Ltd., 2012.
- [17] K. Kopinga and L. Pel, "One-dimensional scanning of moisture in porous materials with NMR," *Review of Scientific Instruments*, vol. 65, no. 12, pp. 3673-3681, 1994.
- [18] L. Pel, P.A.J. Donkers, K. Kopinga and J.J. Noijen, "<sup>1</sup>H, <sup>23</sup>Na and <sup>35</sup>Cl Imaging in Cementitious Materials with NMR," *Applied Magnetic Resonance*, vol. 47, no. 3, pp 265–276, 2016.
- [19] W.E. Lee, W. Vieira, S. Zhang, K.G. Ahari, H. Sarpoolaky and C. Parr, "Castable refractory concretes," *International Materials Reviews*, vol. 46, no. 3, pp. 145-167,

- 2001.
- [20] F.A. Cardoso, M.D.M. Innocentini, M.M. Akiyoshi and V.C. Pandolfelli, "Effect of curing time on the properties of CAC bonded refractory castables," *Journal of the European Ceramic Society*, vol. 24, no. 7, pp. 2073-2078, 2004.
- [21] W.N. dos Santos, "Effect of moisture and porosity on the thermal properties of a conventional refractory concrete," *Journal of the European Ceramic Society*, vol. 23, no. 5, pp. 745-755, 2003.
- [22] A.J. Barakat, L. Pel, O. Krause, O.C.G. Adan, "Direct observation of the moisture distribution in calcium aluminate cement and hydratable alumina-bonded castables during first-drying: An NMR study," *Journal of the American Ceramic Society*, 2019 ( DOI:10.1111/jace.16814).
- [23] E.W. Hansen, R. Schmidt and M. Stocker, "Boiling-point elevation of water confined in mesoporous MCM-41 materials probed by  $^1\text{H}$  NMR," *Studies in Surface Science and Catalysis*, vol. 105, pp. 543-550, 1997.
- [24] H. Peng, B. Myhre, "Improvements in Drying Behaviour and Explosion Resistance of Microsilica-Gel Bonded No-Cement Castables," *Refractories Worldforum*, vol. 9, no. 3, pp. 61-66, 2017.
- [25] A.P. da Luz, M.A.L. Braulio and V.C. Pandolfelli, *Refractory Castable Engineering*. Baden-Baden & Karlsruhe: Federation for International Refractory Research and Education & Goller Verlag, 2015.
- [26] J.A. Larbi and R.B. Polder, "Effects of polypropylene fibres in concrete: Microstructure after fire testing and chloride migration," *Heron*, vol. 52, no. 4, pp. 289-306, 2007.
- [27] A.P. Luz, M.H. Moreira, C. Wohrmeyer, C. Parr, V.C. Pandolfelli, "Drying behavior optimization of dense refractory castables by adding a permeability enhancing active compound," *Ceramics International*, vol. 45, no. 7, pp. 9048-9060, 2019.



---

## Chapter 5: Moisture transport in heated pine wood

---

### Abstract

The quantification of moisture transport in heated wood is relevant to several fields, e.g. for lumber drying and processing and for fire safety risk assessment. We present non-destructive and simultaneous measurements of the moisture content and temperature distributions in pine wood during unilateral exposure to a heat source. The moisture content is measured by a nuclear magnetic resonance setup specifically built for the evaluation of moisture transport in porous materials at elevated temperatures. Temperature profiles are obtained by thermocouples placed at different distances from the exposed surface. While the temperature rises, a peak in the moisture content is formed, which travels towards the unexposed surface. The velocity of the moisture content peak depends on the principal direction in which transport occurs, as confirmed by experiments. Moreover, several characteristics, such as the timescale and non-linearity of the moisture peak position, are well captured. The influence of several input parameters, such as the permeability and diffusion coefficient, on the moisture peak dynamics is elaborately explored.

*This chapter has been adapted from Arends, T., Barakat, A.J. & Pel, L., Exp. Therm. Flu. Sci. (2018) 99. This chapter has also appeared as a section of a chapter in the PhD thesis of Thomas Arends.*

## 5.1 Introduction

Due to its wide availability and renewability, wood has applications in many fields. Wood has been used as a heat source, for weaponry, in creating works of art, and as a construction material for centuries. If applied correctly, wood is a highly durable material, able to stand the test of time [1]. In unfavorable conditions, however, wood can degrade biologically by e.g. fungal growth [2], or mechanically due to moisture-induced stresses. Furthermore, during fire exposure, wood degenerates by pyrolysis, which can result in the failure of a structural element. For that reason, several high-temperature performance requirements are imposed on a building component [3], e.g. on the conservation of loadbearing or insulating capacities. In fire risk assessment, it is therefore of high importance to be able to accurately predict the fire behavior of materials comprising the building component. Since moisture plays a major role in many properties of wood, the qualification and quantification of moisture transport mechanisms is essential.

Numerous modeling studies on heat and mass transfer in wood during exposure to high temperatures exist in literature [3][4][5]; applications are in both fire safety of wood building components [6], as well as in industrial applications, e.g. wood drying [7][8][9][10][11][12]. These models consist of coupled heat and moisture transport equations, i.e., the temperature distribution is influenced by moisture transport and vice versa. Most experimental studies on fire behavior of wood are comprised of measurements of the temperature distribution alone [13]. Experimental studies on moisture transport in wood during fire conditions are scarce; measuring moisture content non-destructively is more complex. Moisture content meters, embedded in a wood slab in a vertical furnace, have been used before to measure moisture profiles at high temperatures by White and Schaffer [14]. The authors recognized, however, that using moisture content meters comes at the expense of large errors. Other non-destructive measurement methods are therefore preferred when measuring moisture content [15], such as neutron imaging [16][17], which, however, requires a neutron source. Another powerful technique is nuclear magnetic resonance (NMR), which has been widely applied to study moisture transport in a variety of porous materials, such as granular beds [18], fluidized bed dryers [19], building materials [20], and also wood [21][22]. Most NMR studies focus on isothermal moisture transport; performing non-isothermal measurements on porous materials requires a specialized setup, able to withstand high temperatures and equipped with a Faraday shield to allow quantitative measurement. Moreover, several materials, e.g. concrete and refractories, possess the risk of explosive spalling when heated, requiring additional safety

measures. Such a custom-built NMR setup has been developed to assess the non-isothermal moisture transport in concrete [23][24], fired-clay brick [25], gypsum [26], and refractory materials [27]. Here, we will employ the setup to explore the moisture transport in wood during heating.

The goal of this study is the simultaneous and non-destructive measurement of both moisture content and temperature in pine wood during intensive one-sided heating, simulating the initial period of a fire. Accordingly a custom-built NMR setup is used, which has been introduced before [28], in combination with inserted thermocouples. Moreover, numerical experiments with a non-isothermal moisture transport model are performed to capture basic characteristic features of moisture transport during these conditions. A concise description of the experimental procedure is discussed first. Experimental results are presented and also discussed, and finally conclusions are drawn and an outlook is presented.

## **5.2 Sample Preparation**

Pine wood cylinders with a diameter of 70 mm and a length of 70 mm are prepared with their axis in either one of the principal directions of wood (longitudinal, i.e., along the grain, and, perpendicular to that, combined radial/tangential). The cylinders are equilibrated at an RH of 53 %, after which they are wrapped in Teflon tape and squeezed in a tight Teflon beaker to seal the sides for moisture transfer, thus creating a semi one-dimensional experiment. Holes are drilled at different distances from the exposed surface (5, 12, 20, 30, 45, and 65 mm), in which thermocouples are placed to measure the temperature during the experiment. The beakers are additionally wrapped in a layer of Rockwool© insulation material to prevent heat losses to the sides and the back surface. The beakers are then placed in the NMR setup, described below.

## **5.3 Experimental Setup**

A home-built NMR setup is used to measure moisture content profiles of a pine cylinder, while it is exposed to a heat source on one side. The setup, schematically shown in Figure 5.1, was specifically designed for performing non-isothermal moisture measurements on building materials, and will be introduced here briefly.

The setup is placed inside the bore of a 1.5 T whole-body medical scanner (Gyrosan, Philips), which provides the main magnetic field during the experiments. A constant gradient of 80 mT/m in the main magnetic field is achieved with two anti-Helmholtz coils, enabling us

to measure one-dimensional profiles with a spatial resolution of approximately 3 mm [27]. A birdcage coil, made from copper strips wrapped around an alumina ( $\text{AlO}_3$ ) tube, is used for sending radio-frequency (RF) pulses and receiving the signal from the sample. The alumina tube is able to withstand high temperatures and provides no background signal. In order to perform quantitative measurements, the coil is equipped with an internal Faraday shield, which prevents detuning of the RF-coil induced by changes in the dielectric constant. To measure the spatial distribution of the moisture content, a Hahn spin echo with an echo time of 300  $\mu\text{s}$  is performed under a gradient at different frequencies, i.e., different slices along the length of the cylinder are excited by RF pulses and measured.

The one-sided heating of the cylinder is achieved by an array of seven 100 W halogen lamps. The reflective surfaces of the lamps are gold-plated to maximize the infrared radiative flux towards the exposed sample surface. Accordingly, the surface can be heated up quickly. The radiative temperature of the lamps is estimated based on the measured temperature increase of the sample.

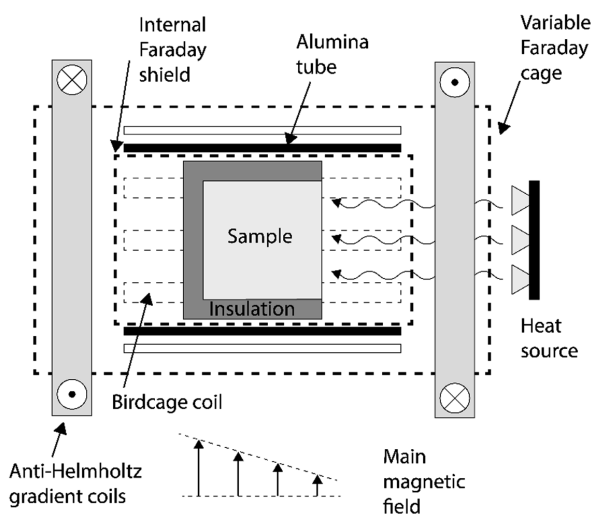


**Figure 5.1:** Schematic representation of the NMR setup used to continuously measure moisture content profiles of a cylindrical pine wood sample, while heated unilaterally by an array of halogen lamps.

#### 5.4 $T_2$ relaxation and signal correction

During our NMR experiments, we measure the magnitude of the nuclear magnetization of protons present in a sample. In general porous media and isothermal conditions, the signal can be directly related to the moisture content of the material and a single conversion factor can be used to calibrate the obtained signal. In our experiments, however, we deal with large temperature differences over the length of the sample, which affects the measured signal twofold. The magnetization magnitude of an unchanging volume of water is inversely proportional to the absolute temperature, also known as the Curie law [28]. Hence, even though the moisture content remains equal, the obtained signal changes continuously. Furthermore, temperature influences the  $T_2$  relaxation times of a system, which characterize the loss of magnetization after excitation in an NMR experiment (i.e.,  $S \sim \exp(-t_E/T_2)$ ). Below the fiber saturation point, i.e., the moisture content of wood in equilibrium with a relative humidity of 100 %, the magnetization decay of moisture in wood can be well described by a single  $T_2$  relaxation time [29]. Generally, the  $T_2$  relaxation time increases with temperature [27][28]. Thence, the obtained signal after an echo time  $t_E$  will be larger at higher temperatures. Accordingly the corrected signal  $S_C$  is obtained from the collected raw signal  $S_R$  as

$$S_C = C_M(T)C_{T_2}(T)S_R, \quad (5.1)$$

where  $C_M$  and  $C_{T_2}$  are correction functions for the magnetization and the  $T_2$  relaxation time respectively.  $C_M$  is proportional to the absolute temperature, which has been verified before by heating a cylindrical flask containing a 0.1 M  $\text{CuSO}_4$  solution while measuring its signal [28].  $C_{T_2}$  is determined on a different setup (0.78 T, for a more detailed description see [30]). A cylindrical pine sample (20 mm in diameter, 20 mm in height) is placed in a closed Teflon sample holder, additionally wrapped in Teflon tape to prevent loss of water. At different temperatures, which is achieved by placing the sample holder in the oven for a sufficiently long period of time, a CPMG sequence [31][32] is performed to determine the  $T_2$  relaxation time.

The  $T_2$  as a function of temperature is shown in Figure 5.2A for two different samples: equilibrated with an RH of 53 % and 93 % respectively. The generally higher  $T_2$  with a higher equilibration RH has been observed before [22], and is most likely due to the increased cell wall water mobility at higher moisture content. In both samples, the  $T_2$  of the

cell wall moisture increases up to a temperature of 100 °C, after which it decreases again. The corresponding total signal of the two samples (extrapolated from the measured CPMG and corrected for the decreased magnetization at higher temperatures using  $C_M$ ) is shown in Figure 5.2B. As can be seen, the signal increases slightly up to a temperature of 100 °C, the origin of which remains unknown to this point. Exceeding 100 °C, the signal rapidly drops to low values. Despite the vapor-tight sealing using Teflon tape, excessive vapour pressure has apparently forced out water vapour from the Teflon sample holder. This is also verified by simultaneously measuring the mass of the samples.

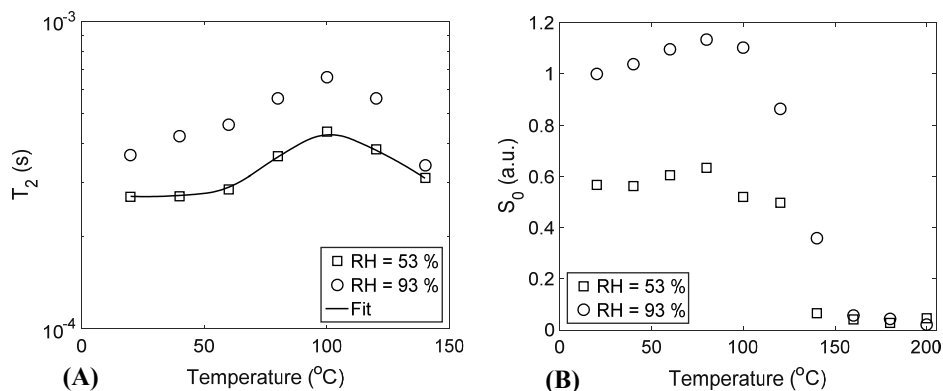


**Figure 5.2:** (A)  $T_2$  relaxation time as a function of temperature for two pine cylinders, initially in equilibrium with a relative humidity of 53 % and 93 % respectively, contained in a closed sample holder. (B) The signal of the pine samples as a function of temperature, additionally corrected for the temperature-dependence of the magnetization.

As can be seen from Figure 5.2A, the  $T_2$  relaxation time of the cell wall moisture is dependent on both moisture content and temperature. Hence, the  $T_2$  correction applied to the raw experimental data is highly complex and non-linear. As a first-order approximation, we neglect the moisture content dependence of the  $T_2$  and employ the correction corresponding to the initial conditions in the experiments (samples equilibrated at RH = 53 %). The  $T_2$ -correction can then be expressed as  $C_{T_2} = \exp(t_E/T_2(T))$ , where  $t_E$  is the echo time in the NMR measurement ( $t_E = 300 \mu\text{s}$ ) and  $T_2(T)$  the free cubic spline fit to the temperature-dependent  $T_2$  data for the sample equilibrated at an RH of 53 % in Figure 5.2A. We thus likely overestimate high values in moisture content. To provide an estimate of the involved error, we take the ratio of the correction factor  $C_{T_2}$  for RH = 53 % and 93 % at 100 °C, which is approximately 1.3. Hence, the moisture content is overestimated by ~30 % at maximum. To

minimize this error, the  $T_2$  as a function of both temperature and moisture content should be determined, which is a subject for future study. The correction to the raw experimental data applied here is qualitatively similar to cases presented by van der Heijden et al. [28] and Barakat et al. [27], where examples of the correction are shown. Additionally, moisture content distributions are normalized by the first profile to account for the decreasing sensitivity away from the center of the coil and for local inhomogeneities in the wood structure.

Several parameters influence the accuracy of moisture measurement using NMR. First of all, a small background signal contributes to the measured signal. To correct for this, the background signal is subtracted from the signal. Furthermore, the signal-to-noise ratio is improved by averaging the signal at each measurement point in space and time. The first profile, which is used to normalize subsequent profiles, is obtained using 64 measurements, all points in successive profiles are averaged 16 times to arrive at an acceptable time resolution of 3.5 minutes per profile (25 points per profile). Each measurement in turn is an average over a slice with a thickness of approximately 3 mm, which further enhances the signal-to-noise ratio. To account for the different time stamp of each measurement point, the acquired data points are linearly interpolated over time to obtain profiles at matching time stamps. Due to the high time resolution, this leads to small errors related to the sequential measurement of profile points.

## 5.5 Discussion and results

### 5.5.1 Moisture content and temperature distribution

Normalized moisture content and temperature profiles during one-sided heating of a pine cylinder, with its axis in the combined radial/tangential direction, are shown in Figure 5.3A and Figure 5.3B respectively. Time between two consecutive profiles is 10 minutes. Initially, the moisture content and temperature are constant throughout the sample. After switching on the heat source, the temperature near the surface quickly rises, resulting in steep gradients as extreme as  $\sim 500$  °C/m. Meanwhile, a peak in the moisture content is formed, which travels towards the back of the sample, while the moisture content left from the peak attenuates to low values. A sharp boundary between dry material left from the peak and the peak in the moisture content itself is observed. The emergence of the moisture content peak is related to rapid release of cell wall moisture in regions with high temperatures. The resulting vapour pressure gradient induces vapour transport. In addition, diffusive vapour transport may also

occur due to concentration differences. Moisture then travels as vapour towards regions of low vapour pressure or low vapour concentration, i.e., towards the surface and towards the back of the sample. Whereas the temperature near the exposed surface is high, lower temperatures toward the back of the sample cause exchange of the water vapour to cell wall moisture, which results in an increase in measurable moisture content. This increase is perceived as the peak shown in Figure 5.3A.

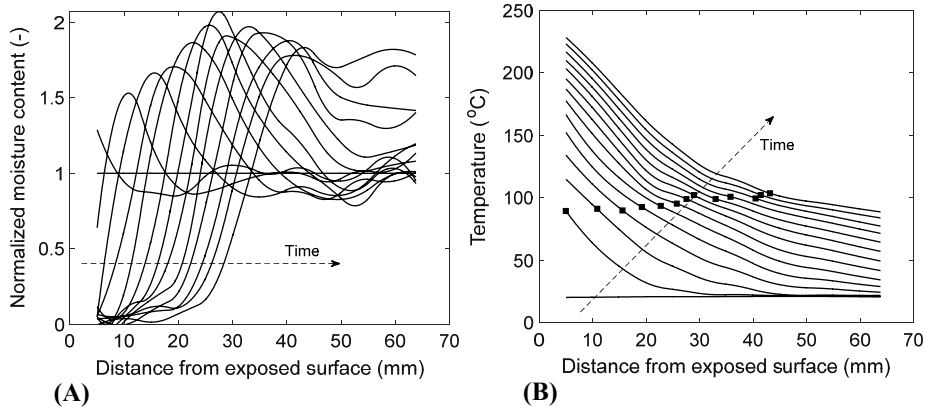


**Figure 5.3:** (A) Normalized moisture content profiles and (B) temperature profiles during one-sided heating of a pine cylinder, with its axis in the combined radial/tangential direction. The time between consecutive profiles is 10 minutes. The position of the peak in moisture content is indicated in each temperature profile with a marker.

Another representation of the same results is shown as the time-evolution of the moisture content and temperature at different distances from the exposed surface in Figure 5.4A and Figure 5.4B respectively. Closest to the surface, the normalized moisture content increases slightly before rapidly decreasing, whereas further away from the exposed surface, the moisture content increases to higher values before decreasing. The peak in moisture content occurs later in time further away from the surface, reaching higher values. A similar time-evolution was found by White and Schaffer [14] and Fredlund [3]. Meanwhile the temperature near the exposed surface quickly rises to high values. White and Schaffer [14] and Fredlund [3] found a plateau in the temperature around 100 °C, which they linked to the heat associated with water evaporation. In this case, a change in the temperature increase is observed around 100 °C as well, although it is less pronounced. A possible cause is the different exposure condition. In the mentioned studies, the sample is either placed in a furnace with temperatures of over 900 °C [14] or exposed to much higher radiant power than



in this study [3]. Furthermore, a higher initial moisture content can affect the temperature course over time due to the higher amount of energy required for evaporation.

It is well-known that the different principal directions in wood exhibit different transport characteristics. Whereas little difference is found between the radial and tangential permeability, the longitudinal permeability can be several orders of magnitude higher, depending on the wood species [33][34]. It is therefore expected that the observed moisture transport characteristics are different in case transport occurs in the longitudinal direction, as opposed to the radial/tangential direction. Normalized moisture content and temperature profiles for the cylinder with its axis along the longitudinal direction are shown in Figure 5.5. Time between two consecutive profiles is 5 minutes, i.e., the time resolution is higher than in Figure 5.3. As can be seen when comparing Figure 5.5A to Figure 5.3A, the peak travels faster in the longitudinal direction, due to the higher permeability. Furthermore, the increase in temperature is more rapid in the longitudinal direction, although the profiles are qualitatively similar. The generally higher thermal conductivity in this direction, typically differing by a factor of two [35], results in a faster increase in temperature. Flatter temperature profiles are, however, expected in case of a higher thermal conductivity, which is not seen in the experimental results.

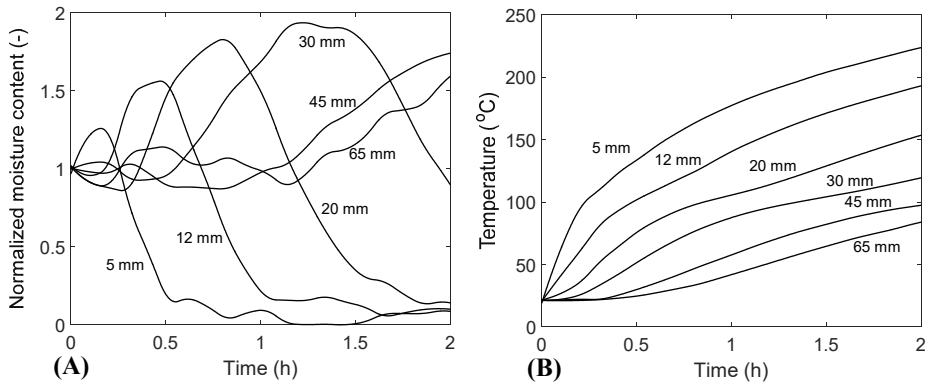


**Figure 5.4:** The time-evolution of (A) the normalized moisture content and (B) temperature at different distances from the exposed surface ( $x = 5, 12, 20, 30, 45,$  and  $65$  mm) in the radial/tangential sample.

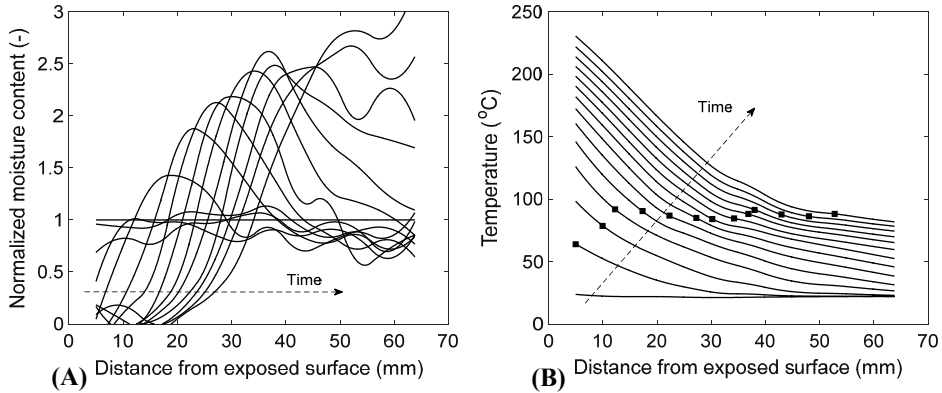


**Figure 5.5:** (A) Normalized moisture content profiles and (B) temperature profiles during one-sided heating of a pine cylinder, with its axis in the longitudinal direction. The time between consecutive profiles is 5 minutes. The position of the peak in moisture content is indicated in each temperature profile with a marker.

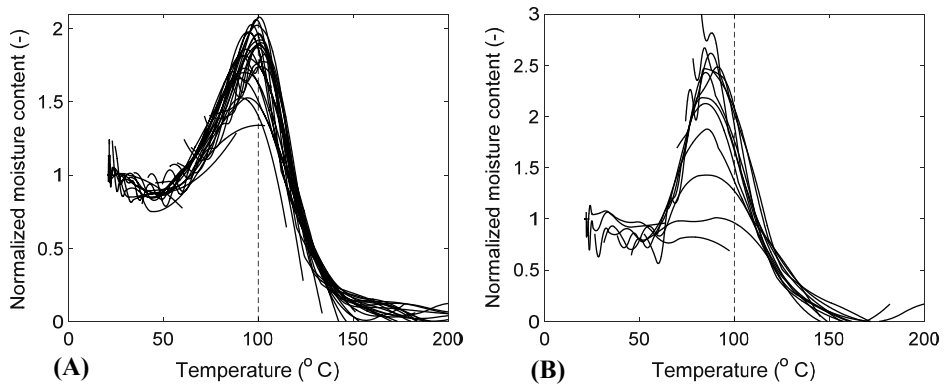


**Figure 5.6:** Normalized moisture content as a function of the temperature during the experiment for the sample with its axis in the (a) combined radial/tangential and (b) longitudinal direction.

Although the timescales associated with moisture and heat transport in the different principal directions are different, the behavior is qualitatively similar. As demonstrated in Figure 5.3B and Figure 5.5B, in both cases the peak in moisture content travels at a constant temperature around 100 °C, which suggests similar timescales for moisture and heat transport respectively in each direction. This is elucidated by plotting the normalized signal as a function of the temperature for each distribution during the experiment in Figure 5.6A and Figure 5.6B for

the combined radial/tangential and longitudinal direction respectively. For temperatures up to  $\sim 70$  °C the moisture content remains equal. With a further increase in temperature, the moisture content rises towards its peak value around 100 °C, followed by a steep decrease in moisture content with increasingly higher temperature. At temperatures above  $\sim 130$  °C, all moisture has been removed from the material. The figure is similar for transport in the longitudinal direction, although the rise of the moisture peak value at a constant temperature of 100 °C is more noticeable.

### 5.5.2 Peak in moisture content

The emergence of a peak in the moisture content was observed in the profiles displayed in Figure 5.3A and Figure 5.5A. This peak travels towards the unexposed surface of the sample and its value grows over time. Its occurrence is linked to the rapid moisture exchange in regions of high temperature and the consequent vapour transport to and moisture exchange in regions of lower temperature. In a later section, numerical simulations are performed to study influential parameters. Here, we will study features of this peak in moisture content in more detail.

The peak position and peak temperature over time for transport in the combined radial/tangential direction are presented in Figure 5.7. As can be seen, the peak position follows a slightly non-linear course over time. This occurs in both principal directions, which is demonstrated by the time-evolution of the peak position in Figure 5.8A. Two measurements have been performed in each direction. The non-linear time-evolution of the peak position can be well fitted with a power law, producing exponents in the range 0.67-0.82. As already observed, the peak velocity is higher in the longitudinal direction than in the radial/tangential direction. Slight differences are found between repeated measurements with different, but similarly cut samples. Nevertheless, the overall behavior is similar, with power law time-dependence of the peak position. This also becomes apparent upon a closer look at the data presented by White and Schaffer, which reveals a power law ( $t^b$ ) dependence of the peak position too rather than the linear dependence reported by the authors.

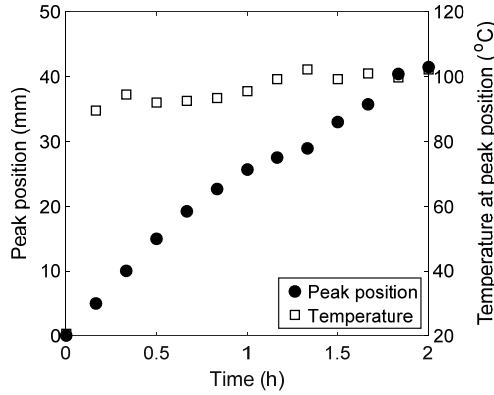


**Figure 5.7:** Peak position and temperature at the peak over time during one-sided heating of a pine cylinder, with its axis in the combined radial/tangential direction.

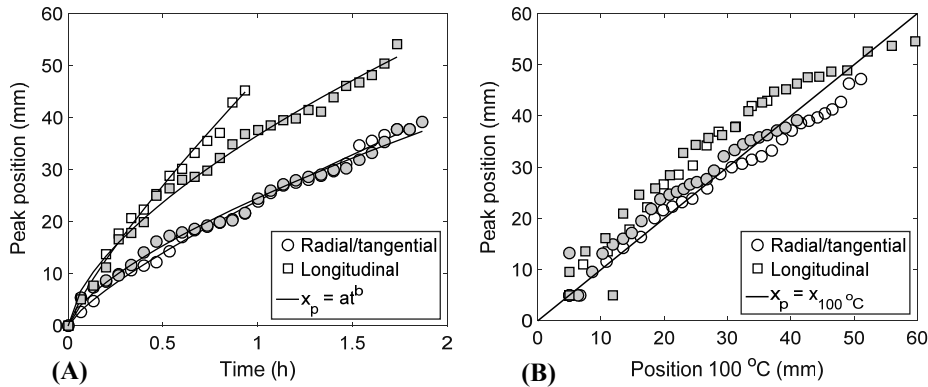


**Figure 5.8:** (A) The peak position as a function of time for the combined radial/tangential and longitudinal cylinders. Grey markers indicate a second measurement under identical conditions, but with a different sample. A power fit to the peak position is added in the figure. (B) The position of the peak in moisture content ( $x_p$ ) as a function of the position where the temperature is 100 °C ( $x_{100^\circ\text{C}}$ ) for the different profiles.

Figure 5.7 also elucidates that the peak temperature quickly attains a constant value around 100 °C. This occurs in both measurements in the radial/tangential direction, which is highlighted in Figure 5.8B by plotting the peak position as a function of the position where the temperature is 100 °C. The values are scattered around the line  $x_{peak} = x_{100}$ , which marks the agreement in position of both the peak moisture content and boiling point. A similar value (98 °C) was measured in the experiments by White and Schaffer [14]. A constant temperature at the peak position indicates that the two timescales of moisture and heat transport are of

similar order. Moreover, it suggests that the pressure in the material does not reach excessive values. In other words, the permeability is sufficiently high to prevent a temperature rise above 100 °C, which can only be achieved at high pressures. For transport in the longitudinal direction we observe a peak temperature which is moderately lower than 100 °C (also observable in Figure 5.6B), but slightly increases over the course of the experiment. This is expressed by the peak position preceding the position of 100 °C in Figure 5.8B, but decelerating in a later stage of the process.

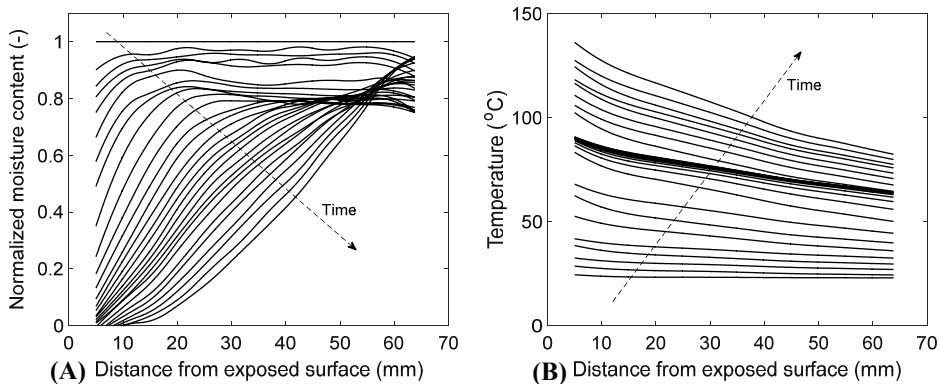


**Figure 5.9:** (A) Normalized moisture content profiles and (B) temperature profiles for a low heating rate of a radial/tangential sample. The heating rate was controlled to have a more or less steady temperature increase over time near the surface. Time between consecutive profiles is 60 minutes.

### 5.5.3 Low heating rate

In isothermal drying of wood, the local moisture content decreases monotonically; a peak in the moisture content only emerges in non-isothermal conditions [3][14]. It can therefore be hypothesized that, in case of a low heating rate and thus small temperature gradients, the peak in moisture content will not appear. To verify this hypothesis, an experiment with a radial/tangential cylinder is carried out in which the heating rate is kept low to ensure small temperature gradients. The normalized moisture content profiles and temperature profiles are shown in Figure 5.9. The time between profiles is 60 minutes. The large number of profiles measured indicates the larger timescale associated with this process (27 hours compared to 1-2 hours). Furthermore, the temperature gradients are considerably smaller when compared to the results in Figure 5.3B. Moreover, as expected, no peak in the moisture content is observed. The slower heating rate results in a lower moisture exchange rate and thus smaller

pressure gradients. Moisture transport is governed by diffusive water vapour transport towards regions of low vapour content, i.e., towards the exposed surface. At a certain moment, a non-uniformity in the temperature increase is observed (the temperature distribution is unchanged), represented by overlapping profiles. This is caused by the stepwise elevation of the power to the halogen lamps ensuring a heat flux towards the surface to arrive at low temperature gradients and an approximately linear increase in surface temperature. At night, however, the constant heat flux resulted in an unchanged temperature distribution, which is most likely caused by heat losses towards the sides and possibly back of the sample. Consecutive elevation of the heat flux results in a temperature increase again.

## **5.6 Conclusion**

We have demonstrated the possibility to assess moisture transport in pine wood at elevated temperatures using NMR. The non-destructive nature of NMR enables us to measure profiles continuously while controlling the heating rate at the exposed surface. A constant heat flux at the exposed surface, imposed by the radiance of gold-coated halogen lamps, results in steep temperature gradients near the surface. Cell wall moisture is released and transported as water vapor. The vapour travels towards regions of lower pressure, i.e., both towards the exposed surface, where the sample dries, and towards the back surface. Near the back surface, the lower temperatures result in exchange of water vapour into cell wall moisture and thus a local increase in the measurable moisture content. Consequentially, a peak in the moisture content is formed, which travels towards the back surface while increasing in intensity. Owing to the direction-dependent transport properties of wood, this peak velocity is higher in the longitudinal direction than in the radial/tangential direction. The temperature at this peak is nearly constant at 100 °C, suggesting the absence of high pressures required for reaching higher temperatures brought about by a sufficiently high permeability. For low heating rates, temperature gradients are considerably lower. Hence the pressure buildup is minor. Water vapour transport toward the back surface is not dominant and therefore no peak in the moisture content is observed. In addition, the whole process is appreciably slower, covering 27 hours instead of two.

## 5.7 References

- [1] K.E. Larsen and N. Marstein, Conservation of historic timber structures: an ecological approach. Oxford: Butterworth-Heinemann, 2000.
- [2] O. Schmidt, Wood and tree fungi: Biology, Damage, Protection, and Use. Berlin: Springer-Verlag, 2006.
- [3] B. Fredlund, "Modelling of heat and mass transfer in wood structures during fire," *Fire Safety Journal*, vol. 20, pp. 39-69, 1993.
- [4] M.L. Janssens, "Modeling of the thermal degradation of structural wood members exposed to fire," *Fire and Materials*, vol. 28, pp. 199-207, 2004.
- [5] R. Pecenko, S. Svensson and T. Hozjan, "Modelling heat and moisture transfer in timber exposed to fire," *International Journal of Heat and Mass Transfer*, vol. 87, pp. 598-605, 2015.
- [6] V.D. Thi, M. Khelifa, M. Oudjene, M. El Ganaoui and Y. Rogaume, "Finite element analysis of heat transfer through timber elements exposed to fire," *Engineering Structures*, vol. 143, pp. 11-21, 2017.
- [7] O.A. Plumb, G.A. Spolek and B.A. Olmstead, "Heat and mass transfer in wood during drying," *International Journal of Heat and Mass Transfer*, vol. 28, no. 9, pp. 1669-1678, 1985.
- [8] N. Oumarou, D. Kocaefe and Y. Kocaefe, "3D-modelling of conjugate heat and mass transfers: Effects of storage conditions and species on wood high temperature treatment," *International Journal of Heat and Mass Transfer*, vol. 79, pp. 945-953, 2014.
- [9] C. Di Blasi, "Multi-phase moisture transfer in the high-temperature drying of wood particles," *Chemical Engineering Science*, vol. 53, pp. 353-366, 1998.
- [10] H.T. Vu and E. Tsotsas, "Mass and heat transport models for analysis of the drying process in porous media: a review and numerical implementation," *International*

- Journal of Chemical Engineering*, vol. 2018, 2018.
- [11] P. Perre and I. W. Turner, "A heterogeneous wood drying computational model that accounts for material property variation across growth rings," *Chemical Engineering Journal*, vol. 86, pp. 117-131, 2002.
- [12] E.J. Carr, I.W. Turner and P. Perre, "A variable-stepsize Jacobian-free exponential integrator for simulating transport in heterogeneous porous media: application to wood drying," *Journal of Computational Physics*, vol. 233, pp. 66-82, 2013.
- [13] P. Reszka and J.L. Torero, "In-depth temperature measurements in wood exposed to intense radiant energy," *Experimental Thermal and Fluid Science*, vol. 32, pp. 1405-1411, 2008.
- [14] R.H. White and E.L. Schaffer, "Transient moisture gradient in fire-exposed wood slab," *Wood and Fiber*, vol. 13, no. 1, pp. 17-38, 1981.
- [15] S. Roels, J. Carmeliet, H. Hens, O. Adan, H. Brocken, R. Cerny, Z. Pavlik, A.T. Ellis, C. Hall and K. Kumaran, "A comparison of different techniques to quantify moisture content profiles in porous building materials," *Journal of Thermal Envelope and Building Science*, vol. 27, pp. 261-276, 2004.
- [16] M.S. Ghilani, S. Abbasion, E. Lehmann, J. Carmeliet and D. Derome, "Neutron imaging of moisture displacement due to steep temperature gradients in hardwood," *International Journal of Thermal Sciences*, vol. 81, pp. 1-12, 2014.
- [17] M. Sedighi Gilani, P. Vontobel, E. Lehmann, J. Carmeliet and D. Derome, "Moisture migration in wood under heating measured by thermal neutron radiography," *Experimental Heat Transfer*, vol. 27, no. 2, pp. 160-179, 2014.
- [18] P.A.J. Donkers, L. Pel and O.C.G. Adan, "Dehydration/hydration of granular beds for thermal storage applications: a combined NMR and temperature study," *International Journal of Heat and Mass Transfer*, vol. 105, pp. 826-830, 2017.
- [19] M. Peglow, U. Cunäus and E. Tsotsas, "An analytical solution of population balance equations for continuous bed drying," *Chemical Engineering Science*, vol. 66, pp.



1916-1922, 2011.

- [20] C. Nunes, L. Pel, J. Kunecký and Z. Slízková, "The influence of the pore structure on the moisture transport in lime plaster-brick systems as studied by NMR," *Construction and Building Materials*, vol. 142, pp. 395-402, 2017.
- [21] T. Arends, L. Pel and D.M.J. Smeulders, "Moisture penetration in oak during sinusoidal humidity fluctuations studied by NMR," *Construction and Building Materials*, vol. 166, pp. 196-203, 2018.
- [22] M. Zhou, S. Caré, D. Courtier-Murias, P. Faure, S. Rodts and P. Coussot, "Magnetic resonance imaging evidences of the impact of water sorption on hardwood capillary imbibition dynamics," *Wood Science and Technology*, 2018.
- [23] G.H.A. van der Heijden, R.M.W. van Bijnen, L. Pel and H.P. Huinink, "Moisture transport in heated concrete, as studied by NMR, and its consequences for fire spalling," *Cement and Concrete Research*, vol. 37, no. 6, pp. 894-901, 2007.
- [24] G.H.A. van der Heijden, L. Pel and O.C.G. Adan, "Fire spalling of concrete, as studied by NMR," *Cement and Concrete Research*, vol. 42, no. 2, pp. 265-271, 2012.
- [25] G.H.A. van der Heijden, H.P. Huinink, L. Pel and K. Kopinga, "Non-isothermal drying of fired-clay brick, an NMR study," *Chemical Engineering Science*, vol. 64, no. 12, pp. 3010-3018, 2009.
- [26] G.H.A. van der Heijden, L. Pel, H.P. Huinink and K. Kopinga, "Moisture transport and dehydration in heated gypsum, an NMR study," *Chemical Engineering Science*, vol. 66, no. 18, pp. 4241-4250, 2011.
- [27] A.J. Barakat, L. Pel and O.C.G. Adan, "One-dimensional NMR imaging of high-temperature first-drying in monolithics," *Applied Magnetic Resonance*, 2018.
- [28] G.H.A. van der Heijden, H.P. Huinink, L. Pel and K. Kopinga, "One-dimensional scanning of moisture in heated porous building materials with NMR," *Journal of Magnetic Resonance*, vol. 208, no. 2, pp. 235-242, 2011.

- [29] Ö. Gezici-Koç, S.J.F. Erich, H.P. Huinink, L.G.J. van der Ven and O.C.G. Adan, "Bound and free water distribution in wood during water uptake and drying as measured by 1D magnetic resonance imaging," *Cellulose*, vol. 24, no. 2, pp. 535-553, 2017.
- [30] R.M.E. Valckenborg, L. Pel, K. Hazrati, K. Kopinga and J. Marchand, "Pore water distribution in mortar during drying as determined by NMR," *Materials and Structures*, vol. 34, pp. 599-604, 2001.
- [31] H.Y. Carr and E.M. Purcell, "Effects of diffusion on free precession in nuclear magnetic resonance experiments," *Physical Review*, vol. 94, no. 3, pp. 630-638, 1954.
- [32] S. Meiboom and D. Gill, "Modified spin-echo method for measuring nuclear relaxation times," *The Review of Scientific Instruments*, vol. 29, pp. 688-691, 1958.
- [33] J.F. Siau, *Transport processes in wood*. Berlin, Heidelberg, New York: Springer, 1984.
- [34] W. Jinman, D. Chengyue and L. Yixing, "Wood permeability," *J. Northeast For. Univ.*, vol. 2, no. 1, pp. 91-97, 1991.
- [35] J.F. Siau, "A geometrical model for thermal conductivity," *Wood and Fiber Science*, vol. 1, pp. 302-307, 1970.

---

## Chapter 6: Conclusions and outlook

---

### 6.1 Conclusions

In this thesis we have set out to investigate the drying behavior (100-300 °C) of various calcium alumina- and hydratable alumina-bonded refractory castables in relation to their physical and chemical properties. This knowledge was furthermore employed to validate a more fundamental understanding of 1D moisture and heat transport processes governing the drying of these materials.

As outlined at the end of Chapter 1, the motivation for this research was to provide industrial users of refractories with a more *quantitative* understanding of how moisture behaves as it is being driven out of the castable pore structure, after placement along the refractory lining of steel ladles. Knowledge of drying also provides a clearer understanding of how high vapour pressures may dangerously approach values resulting in explosive spalling of the refractory lining.

For the purpose of meeting this goal, a specialized high-temperature Nuclear Magnetic Resonance (NMR) setup was constructed, calibrated and tested demonstrating that quantitative measurements of the moisture and temperature profiles as a function of time was possible for samples as long as 100 mm. The main findings and conclusions of using this setup for first-drying experiments will be presented and discussed in this chapter.

First, the drying behavior of a survey list of various castable materials, prepared with different formulation parameters and inputs, e.g. binder content, water demand, additives, etc. was investigated. The moisture and temperature profiles revealed two general, universal features:

- i. Externally-limited drying: fast, homogeneous, environmentally-determined dewatering rate.
- ii. Internally-limited drying: slow, heterogeneous, locally-determined, i.e., permeability, pore structure, etc. dewatering rate.

Furthermore, it is found for (ii) that a boiling front emerges and travels through the material. This boiling front associated with (ii) is characterized by the following three universal observations:

- (A) The boiling front defines a boundary between liquid and vapour.
- (B) The front position  $u$  is increasingly a linear function of time. The corresponding speed  $du/dt$  of this drying front is the same for most materials within a first-order approximation.
- (C) The front temperature  $T(u)$  is increasingly a linear function of time. The corresponding heating rate  $dT/dt$  of this drying front is the same for most materials within a first-order approximation.

Regarding item (C), the boiling front temperature correlates with certain material characteristics. It is found that Low-Cement Castables (LCC) display higher front temperatures than Regular Castables (RC). However, it is microsilica fume-containing LCC that display the highest front temperatures (200 °C), non-fume LCC and Non-Cement Castables (NCC) that display intermediate starting front temperatures (150 °C). RC and LCC Fume MIPORE display the lowest starting front temperatures (110-120 °C), where the latter material is a variant of the LCC Fume formulation in which 50 % of CA binder is replaced with a permeability enhancing active compound. The calculated vapour pressures based on these starting boiling front temperature range from 0.1 MPa (110-120 °C) to 2 MPa (200 °C). On the basis of the drying behavior, we can group the materials into families with common properties, i.e., starting boiling front temperature.

The universal features in (A)-(C) suggest that the speed and heating rate of evaporation has a more fundamental explanation, which is independent of the material characteristics. In terms of the drying front speed, the linear functional form can be qualitatively related to the lumped moisture diffusivity parameter that appears in the one-dimensional analytical model of drying. By applying the non-linear diffusion equation over a spatially finite domain, the quasi-steady state solution to the drying problem yields a form of  $u$  that varies linearly with  $t$ , i.e., constant speed. This is a significant result as solving the diffusion equation over a semi-infinite domain yields a boiling front position that varies with  $\sqrt{t}$  [1]. Furthermore, the universal linear functional form of the front speed may also be determined by parameters related to both the liquid and vapour diffusion terms [2].

By employing a simple first-order model that only considers vapour transport toward the surface of the material, we are able to relate the drying behavior of different materials with the pore structure, i.e., high-temperature vapour permeability. This follows from the fact that permeability is the only required free parameter, which greatly simplifies the model in comparison with other models requiring several free parameters.

Here we see an inverse relationship between the boiling front temperature and permeability; thus high-permeability materials (e.g. RC) correspond with a low boiling front temperature and low-permeability materials correspond with a high boiling front temperature (e.g. LCC Fume). Also, what was found was that the characteristic material permeability measured at room temperature differs from the fitted value provided by the model, i.e., vapour permeability in some cases by a whole order of magnitude, such as RC.

From a materials specification point of view, there are also generally differences in the properties between RC and dispersed formulations e.g. LCC. The LCC family (especially LCC Fume) tend to be denser and finer in grain size. In the case of Fume-containing formulations, the microsilica particles act as fillers thereby reducing grain porosity even further. Additionally, the pore size evolution as a function of temperature is different for both of these materials at much higher temperatures. In Figure 6.1, we plot the median pore sizes as a function of temperature for RC and LCC samples to illustrate some of the differences in pore structure at very high temperatures. As can be seen, the temperature range which this thesis focuses on is unaffected by the early stage transformation of pore size.

It was shown in Chapter 3 that there is also a linear relationship between the front position and front temperature for two materials: (1) RC and (2) LCC Fume A. By fitting our model through the data, it was demonstrated that the linear behavior could be explained in terms of the fitted permeability. Furthermore, to the extent that thermal diffusion plays a less dominant role in vapour transport toward the surface than pressure-flow, the fit turns out to be more agreeable thereby validating the assumptions of the model. Therefore, both (a) front linearity and (b) inverse relationship between front temperature and permeability is due to the weak propagation of heat throughout our sample, where only the equilibrium vapour pressure can effectively drive out the moisture. This also means that from an industrial point of view low-permeability materials have to be dried very cautiously as the pressure is the primary critical factor ensuring safe moisture release, at these given heating rates.

On this basis of fitting the model to our experimental data, the drying behavior of different materials is classified as a function of the starting front temperature and vapour permeability  $k$  (by order of magnitude):

<b>Material</b>	<b>Starting Drying Front Temperature</b>	<b>Vapour Permeability</b>
RC	110 °C	$k_1 = 10^{-15} \text{ m}^2$
LCC/NCC	150 °C	$k_2 = 10^{-16} \text{ m}^2$
LCC Fume	170-200 °C	$k_3 = 10^{-17} \text{ m}^2$
NCC 48 hours	150 °C	$k_4 = 10^{-18} \text{ m}^2$

The unique case of NCC cured for 48 hours is an outlier. This material has the slowest boiling front speed of all materials, and thus the boiling front will travel quite slowly into deeper regions of the material. Therefore, both  $k$  and  $du/dt$  take on relatively low values.

However, regardless of the material of choice, all the dry components were impregnated with polypropylene (PP) fibers to promote escape of moisture at higher temperatures. In a further study, we aimed to investigate the effects of fiber additions on dry-out behavior. Therefore, we chose a fiber-free reference material and compared it with the drying profiles of fiber-containing products, with the same water-to-binder ratios. The materials chosen for this study were microsilica gel-bonded castables of two types: (1) LCC and (2) NCC. We also chose to gain a better understanding of the use of another permeability enhancing active compound, MIPORE 20.

The results show that drying LCC/NCC results in a boiling front temperature as low as 150 °C and as high as 250 °C. This corresponds with an equilibrium vapour pressure of 0.5 MPa-4 MPa. The addition of PP fibers generates a stagnating front temperature of 170 °C for NCC, which doesn't move, and 150-200 °C for LCC corresponding to a vapour pressure of 0.5 MPa-2 MPa. As demonstrated in Chapter 3 with our simple vapour transport model, this stagnation of the front temperature has more to do with having a higher permeability. In the case of LCC Fume, the front doesn't emerge until 150 °C and continues on to just a bit above 200 °C, i.e., a vapour pressure of 2 MPa and thus lower permeability. However, with MIPORE-containing LCC Fume, the front temperature begins at 120 °C and more or less stays there, corresponding to a vapour pressure of 0.2 MPa, i.e., higher permeability.

Therefore, with MIPORE the water is released at 100-150 °C and for PP fibers between 150-200 °C.

In a final analysis of our materials, we decided to compare the drying of castables with that of pine wood under fire conditions. The motivation for this was in order to compare castables with a porous material of very different physical and thermal characteristics, i.e., larger temperature gradient, permeability, etc. Here, the same specialized high-temperature NMR setup introduced in Chapter 2 was applied for performing these experiments. Like before, the quantitative moisture profiles and temperature profiles were measured at the same time. The moisture loss of wood displayed a very different behavior than that of castables.

First, the temperature gradient was about 1000 times larger than that generated by the heating of castables. Within 30 minutes, the surface temperature approaches 100 °C, at which point a moisture peak emerges and begins to travel toward the back of the sample. Overtime, the moisture content corresponding to this peak will also increase and reach a maximum value, rising as high as more than twice the initial moisture content. This increasing peak is associated with the moisture transport from high-temperature regions toward low-temperature regions at the back of the sample. Furthermore, the temperature of this peak remains approximately constant at 100 °C throughout the experiment, suggesting that the moisture can easily escape at the normal boiling pressure of water. With most castables, the starting boiling temperature is at 150 °C and increases to 200 °C or higher. Hence, we already see two primary differences between the drying of castables and pine wood: (i) lower boiling pressure of water and (ii) the influence of a steep temperature gradient on the moisture release of water.

With our unique high-temperature experimental setup, we have demonstrated that the transport processes governing the drying of castables can be quantitatively understood as a function of different material inputs. To the best of our available knowledge, this thesis provides the first direct evidence of the emergence of a boiling front with the characteristic properties already described at length. These associated properties include certain general features e.g. constant boiling front speed; physical transport parameters, e.g. vapour permeability, evaporation front temperature; and the effect of controlling some of these parameters, e.g. fiber- or MIPORE-addition. To this end, we have also provided industrial

users of refractories with benchmark information on the drying of these materials for future applications.

In Chapter 1, we sought to answer some research challenges presented by gaps in knowledge on the relationship between the boiling front behavior e.g. position and temperature, and free moisture and material characteristics. Until now, this knowledge has been seen as “mystical” or “black magic” from the point of view of the refractory user.

The general conclusion of this thesis is that a simple vapour transport model can quantitatively explain the observable boiling front behavior (in space and temperature) as a function of specific material inputs, namely the water demand and binder content. These inputs can furthermore be related to the output characteristics of the material, such as the permeability, which is able to predict the boiling front temperatures and pressures when adjusting for material selection. We find that the boiling front position is a linear function of time, which is probably a reflection of the moisture diffusivity behavior for a sample with short dimensions; and that the boiling front temperature is inversely related to the vapour permeability. As the vapour permeability varies by an order-of-magnitude for each material family, we see that each family has a different characteristic microstructure. Therefore the drying behavior is a thermally non-diffusive, pressure-driven phenomenon, i.e., via Darcy’s law, controlled by only the vapour permeability.

## **6.2 Outlook**

As the research goal and conclusions of this study have been laid out, there are still areas of improvement that should be considered and explored for future work on the subject of first-drying of refractory castables. In this section, we will briefly outline some of these research questions of further investigation.

### **6.2.1 Heating Rate**

The experiments in this thesis were performed using the same maximum heating rate of 1-2 °C/minute. In an actual preheating plant, the manufacturer must control the pressure development as a matter of safety during first-drying. Therefore, it is often necessary for



refractory driers to apply slow heating rates of less than 0.5 °C/minute. To this end, we have also performed some experiments with lowered heating rates on the order of 0.3-0.4 °C/minute that may serve as a future guide for further experiments with lower, adjusted heating rates on the same order as the heating schedules described in Chapter 1.

Normally, the heat flux was supplied by increasing the power to the allowable maximum capacity. For the lowered heating rates, we remotely controlled the heating rate in order to slow down the temperature rise. By doing this, the moisture and temperature profiles were measured for a select list of samples that have already been considered in this thesis: LCC; LCC Fume B; LCC Fume A MIPORE. In the same way as before, we then analysed the drying front behavior as a function of time and compared the results with the data from the normal heating rates. The results are shown in Figure 6.2.

What is seen from the drying behavior of low and high heating rates is that the drying front position is a linear function of time in both cases. The drying front temperature is also a linear function of time, as seen with the high heating rates. Furthermore, to a first-order approximation, the speeds of the drying front position and temperature are similar to those displayed from the high heating rate experiments. The one notable exception comes from LCC Fume MIPORE under a low heating rate, which shows that the front temperature slightly increases with time. Therefore, these experiments suggest that lowering the heating rate does not allow for control of the pressure development during the internally limited drying stage, and thus caution should be taken during this final period of dry-out.

However, it should also be taken with caution that LCC and LCC MIPORE do not generate hydrate phases that are stable over higher temperatures. In particular, the experiments presented here reveal a boiling front temperature that is solely governed by the internal pore pressure development, i.e., the evaporation of bulk water, not by the decay of hydrate phases.

While the low heating rate is less than half the value of our usual heating rates, the literature focuses on more extreme heating rates that are an order of magnitude higher than the ones used in our laboratory [3][4][5].

Therefore, for future work it would be advisable to increase the heating rate by an order of magnitude e.g. 10-20 °C/minute to see if this affects the temperature or speed of the drying front. In such a case, we would expect the pressure development to be much faster than the moisture release rate, as already discussed in Chapter 1.

### **6.2.2 Temperature**

Another benefit of increasing the heating rate is accessing those higher temperatures in the 300-400 °C range that will allow us to probe dehydration, which is known to be the more dominant mechanism of water release at such higher temperatures. It has already been verified that a post-fired specimen can still continue to lose water by placing it in a high-temperature furnace. While there is much literature elaborating on the vapour pressure development inside the pores, there does not seem to be solid consensus on whether dehydration or free moisture is the most crucial step in safe dry-out of castables [5][6]. As a note of consideration, it should be mentioned that dehydration is not necessarily limited to this upper temperature range. And furthermore, the phase stability of the hydrates is dependent on both the temperature and pressure inside the pores.

### **6.2.3 Temperature Gradient**

In the conclusions section, we have already mentioned the fact that the heating up of wood generates temperature gradients orders of magnitude higher than that observed with the heating of castables. In our experiments, the samples are well insulated to prevent heat losses. However, in an actual refractory lining there will be cooling effects that introduce much larger temperature gradients. In the conclusions of chapter 4, we noted that a large temperature gradient does not occur, thereby preventing water migration to the coolest part of the back of the sample.

Therefore, for future work, we advise increasing the temperature gradient of castables by fixing the temperature at the back of the sample, e.g. via cooling or again utilizing the greater energy input at the front of the sample by increasing the maximum deliverable power of our heat source, i.e., increasing the heating rate. Furthermore, it is also suggested to increase the sample dimensions in order to see how the temperature distribution changes.

### **6.2.4 NMR Relaxation**

The considered castables contain three different states of water: free water (bulk state); gel-bounded water (physically combined state); and hydrate-bounded water (chemically combined state). For a model material, i.e., Regular Castable, it was found that the characteristic transverse relaxation time was a function of temperature and hydrate state, based on the measured temperature profiles. Additionally, the equilibrium magnetisation in a

homogeneous magnetic field varies with the temperature of the field. Thus, the quantitative moisture profiles were calibrated to reflect such temperature-dependent correction factors for all subsequent measurements on different materials.

In chapter 2, we measured variations in the transverse relaxation time,  $T_2$ , as a function of temperature, on a model material, RC. What was seen was that  $T_2$  could be fitted to an Arrhenius function, revealing the linear dependence of relaxation on temperature and hydration state. However, at around 90 °C there was a rapid spike in the  $T_2$  behavior and then a rapid decline after 100 °C. It was deduced that this erratic  $T_2$  behavior was likely due to the evolving pore network, i.e., the surface-to-volume ratio was changing.

With an echo time of 110  $\mu$ s, we were only able to measure the  $T_2$  components corresponding to pore water, which was on the order of 500-1000  $\mu$ s. With castables, the active bond system generates hydrate phases that lose their water or transform upon heating. In the case of a material like RC, the aggregate-matrix is enriched with these metastable calcium alumina phases. For instance, amorphous CAH<sub>10</sub> can dissociate at 120 °C and it was seen earlier with RC that around 90 °C a moisture peak suddenly emerged and quickly travelled to the back of the sample [6]. As far as the  $T_2$  analysis and initial moisture rise is concerned, no other material examined so far in this entire thesis has displayed such an irregular evolution in its pore structure as much as RC. And the reason behind this non-linear  $T_2$  change is not completely understood. Therefore, a further investigation into characterizing the material properties of RC with other techniques (e.g. XRD, TGA, permeametry, etc.) is necessary in order to gain a more rigorous understanding of the castable microstructure over this temperature range.

Furthermore, in the case of RC a minor increase in the average moisture content occurred around 150-200 °C, after the sample has already dried. This also corresponded with a densification in the temperature profiles, and an inflection point in the heating rate within the same temperature range. Previous investigations suggest that this could be due to the release of the stabilized hydrate compounds known to begin dehydrating at these higher temperatures, i.e., the decomposition of C<sub>2</sub>AH<sub>8</sub> (170-195 °C) [6][7].

Finally, it was shown in Chapter 3 that as the sample begins to cool down after reaching 250 °C, the moisture content will decrease, but still hover above the NMR noise level, i.e., there is a residual moisture content at the end of the experiment. One offered hypothesis for this moisture decrease upon cooling, was that the active matrix underwent rehydration with the remaining pore water. In principle this would be possible to verify by continuously measuring the changing  $T_2$  as a function of temperature. An overview of these hydrates and their corresponding decomposition temperature  $T_d$  was already provided in Table 3.3:  $C_2AH_8$  ( $T_d = 170-195$  °C);  $C_3AH_6$  ( $T_d = 240-370$  °C); or  $AH_3$  – gibbsite ( $T_d = 210-300$  °C). However, the exact phase morphology would have to be independently verified in order to complement the  $T_2$  data.

If the echo time can be reduced to less than 100  $\mu s$ , it may be possible to observe how the chemically bound components of water, the hydrate phases, are altering the pore microstructure. And by comparing these shorter components to the longer  $T_2$  components of water, we can directly observe how the different states of water are interacting with the entire castable system.

### **6.2.5 MIPORE Addition**

The use of a permeability enhancing active compound, MIPORE 20, was used to characterize how the permeability can change in a first-drying experiment. Fume-containing castables are standard formulations in the industry and as their permeability is quite low compared to other castables, they provide a convenient reference case for evaluating the effects of permeability-enhancement. With the use of LCC Fume 1 as a reference material, the NMR moisture profiles revealed that the permeability indeed increases quite a lot. This was illustrated by the fact that the drying front temperature was reduced from 150-200 °C (MIPORE-free) to 120 °C (MIPORE-containing).

Furthermore, in Chapter 3 we introduced a simple vapour transport model to fit the high-temperature permeability through our experimental data for a variety of castables. In this simple model, permeability is the only free parameter. The agreement between our data and the fit was relatively good. However, our fit represented a kind of average over the vapour regime of drying. In Figure 6.3, we have plotted the boiling front position and boiling front temperature as a function of time and fitted it to our simple model. In this case, the fit is

implemented over two different time periods  $k_1$  and  $k_2$  (solid and dashed lines) in order to see if the permeability changes at all. The boiling front temperature does not show much of a difference between  $k_1$  and  $k_2$ , though the fits are already an order-of-magnitude higher than the measured permeability at room temperature, where  $k_{roomT} = 3 \cdot 10^{-15} \text{ m}^2$ . Furthermore, the fit to the boiling front position indeed shows that the permeability is drastically increasing from  $10^{-15} \text{ m}^2$ , at around 100 minutes, towards a similar fitted value seen from the boiling front temperature, that is on the order of  $10^{-14} \text{ m}^2$ . Therefore, on the basis of this simple model it is observed that the permeability of the MIPORE-containing castable is increasing by the time the vapour phase has been reached.

Unlike PP fibers, which evaporate and burn away, MIPORE undergoes structural transformation when bonded into calcium alumina. The reaction of MIPORE and hydrated CA yields non-crystalline CA hydrate gel phases that experience some kind of rupture or cracking [8][9]. In this way, water is believed to escape at lower temperatures.

However, our characterization (XRD, TGA/DSC) of hydrated CA-free MIPORE particles reveals that there is a crystalline phase, which does not seem to significantly restructure above  $100 \text{ }^\circ\text{C}$  in the same way as PP fibers. On the other hand, the NMR profiles and simple model have shown that there is indeed some internal transformation occurring thereby facilitating easy escape of moisture. As this is a puzzling revelation, more work needs to be undertaken to fully understand the characteristics of this material.

For one thing, it would be advised to perform NMR experiments on more than just one reference material, i.e., LCC Fume A. It may be useful to add MIPORE to one LCC, LCC Fume and NCC material. For NCC, this would be most interesting since the literature states that CA gel phases are generated by adding MIPORE to the castable formulation, therefore raising the question if an NCC (CA-free) castable would lead to the same results.

Furthermore, in order to gain a more complete understanding of the phase morphology, additional measurements should be conducted to complement the NMR measurement. Isolated anhydrous MIPORE particles, hydrated MIPORE particles and CA hydrated MIPORE particles should be characterized with XRD across the full temperature range of  $20\text{-}200 \text{ }^\circ\text{C}$ .

In summary, the key remaining issues that need to be resolved or investigated further for future work are:

- How higher heating rates affect the boiling of moisture (temperature, pressure).
- The relationship between temperature gradient and moisture release.
- The degree of influence dehydration has on the drying process.
- Expanding characterization techniques for understanding the relationship between structural transformation of the MIPORE phases and vapour permeability, during dry-out.
- Gaining a deeper understanding of the material characteristics as a function of temperature and water pressure.

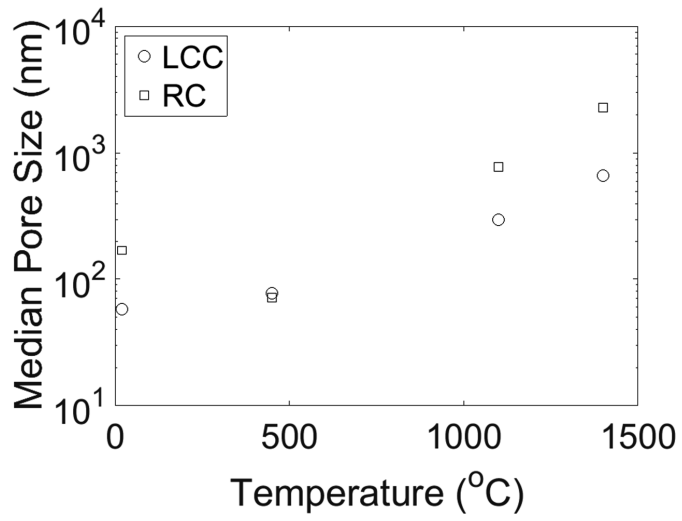


**Figure 6.1:** Plot of the median pore size as a function of temperature for RC and LCC samples (source: Koblenz University of Applied Sciences, Germany).

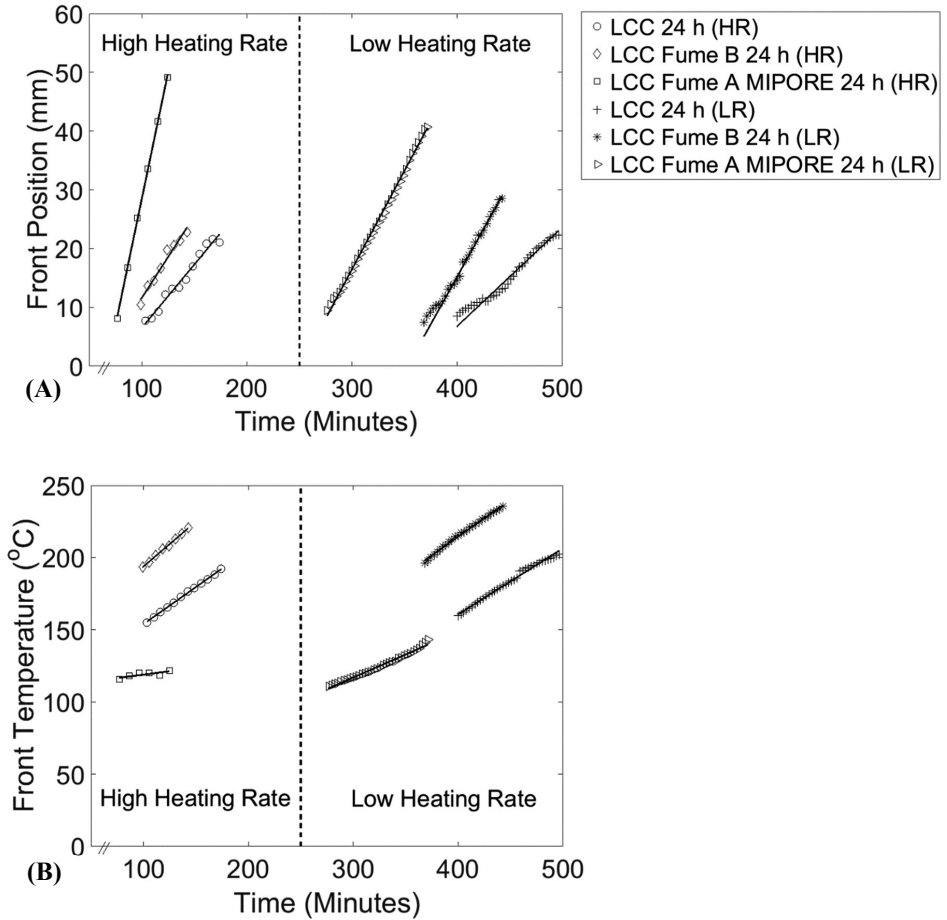


**Figure 6.2:** Plot of the (A) boiling front position and (B) boiling temperature as a function of time, taken from the measured NMR saturation and temperature profiles. Three different materials are investigated: LCC, LCC Fume B, LCC Fume A MIPORE. The vertical dashed line separates two different heating rates used in the experiments: high rate (HR) 1-2 °C/minute and low rate (LR) 0.3-0.4 °C/minute. The solid lines in both plots correspond to the linear fit of our data.



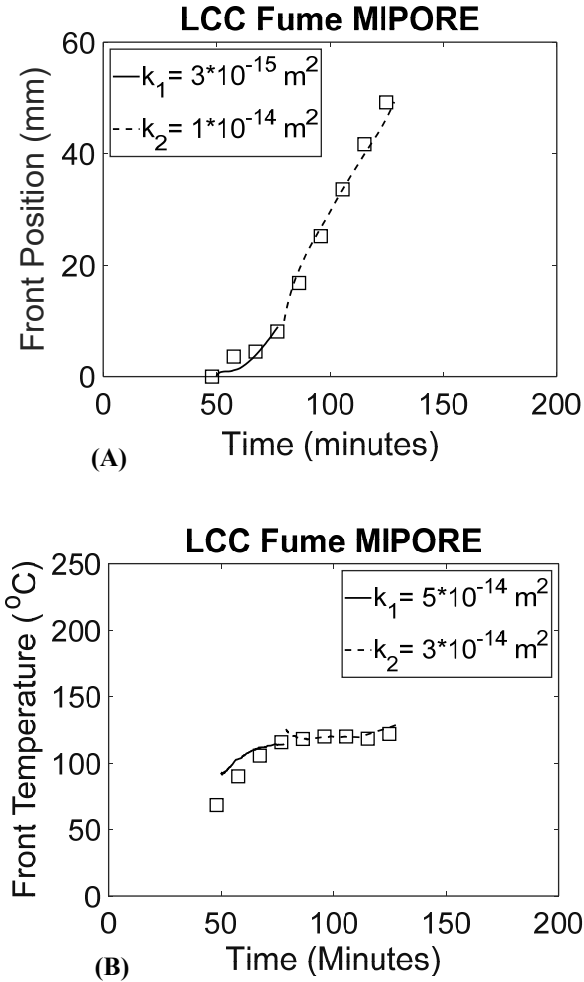


**Figure 6.3:** Plot of the (A) boiling front position and (B) boiling front temperature as a function of time for LCC Fume A MIPORE. The data is taken from the measured NMR saturation profiles and temperature profiles. In both plots,  $k_1$  and  $k_2$  (solid and dashed lines) correspond to the fit of the experimental data to the simple model. The experimentally measured permeability at room temperature is on the order of  $k_{roomT} = 3 \cdot 10^{-15} \text{ m}^2$ .

### 6.3 References

- [1] K.A. Landman, L. Pel and E.F. Kaasschieter, "Analytic modelling of drying of porous materials," *Mathematical Engineering in Industry*, vol. 8, no. 2, pp. 89-122, 2001.
- [2] L. Pel, K.A. Landman and E.F. Kaasschieter, "Analytic solution for the non-linear drying problem," *International Journal of Heat and Mass Transfer*, vol. 45, no. 15, pp. 3173-3180, 2002.
- [3] M.D.M. Innocentini, M.F.S. Miranda, F.A. Cardoso and V.C. Pandolfelli, "Vaporization Processes and Pressure Buildup during Dewatering of Dense Refractory Castables," *Journal of the American Ceramic Society*, vol. 86, no. 9, pp. 1500–1503, 2003.
- [4] F.A. Cardoso, M.D.M. Innocentini, M.F.S. Miranda, F.A.O. Valenzuela and V.C. Pandolfelli, "Drying behavior of hydratable alumina-bonded refractory castables," *Journal of the European Ceramic Society*, vol. 24, no.5, pp. 797-802, 2004.
- [5] A.P. da Luz, M.A. Braulio and V.C. Pandolfelli, *Refractory Castable Engineering*, Baden-Baden & Karlsruhe: Federation for International Refractory Research and Education & Goller Verlag, 2015.
- [6] W.E. Lee, W. Vieira, S. Zhang, K.G. Ahari, H. Sarpoolaky and C. Parr, "Castable refractory concretes," *International Materials Reviews*, vol. 46, no. 3, pp. 145-167, 2001.
- [7] F.A. Cardoso, M.D.M. Innocentini, M.M. Akiyoshi and V.C. Pandolfelli, "Effect of curing time on the properties of CAC bonded refractory castables," *Journal of the European Ceramic Society*, vol. 24, no. 7, pp. 2073-2078, 2004.
- [8] C. Wohrmeyer, J.M. Auvray and C. Zetterstrom, "Dry Out of Dense Refractory Castables via Use of Permeability Enhancing Active Compound," in *Proceedings of Eurogress*, Aachen, 2016.
- [9] C. Wohrmeyer, P. Edwards and C. Parr, "Raw Material Innovations- a Key Success Factor in a Fast Changing Refractories World," *Refractories Worldforum*, 2017.

---

## Summary

---

High-alumina refractory castables are vital to the lifetime of a steel ladle's performance, such that it ensures physical and thermal durability at the melting temperature of steel, in the temperature range of 1000 to 1750 °C. In particular, calcium alumina/hydratable alumina castables present a serious challenge with regards to removing the physical and chemically combined water components from the porous network prior to taking them into full service. Due to the high-risk of generated steam pressures destroying the material at temperatures above the boiling point of water, castables must be pre-dried at less than 1 °C/minute to ensure safe evacuation of the moisture. In particular, the dangerous ebullition stage (100-300 °C) and decomposition of the hydrate phases (200-300 °C) pose the greatest concern during heat-up. Therefore, a quantitative understanding of the transport processes that govern first-drying (100-300 °C) will help inform refractory engineers in selecting suitable heating schedules for a given set of materials. Furthermore, mapping the influence of various key parameters, i.e. heating rate, water demand, binder content, curing time, etc. on drying behavior can also provide insight for optimizing the drying schedule. Because the materials are actually heated from one-side, first-drying of castables can be regarded as a one-dimensional heating problem.

Since most techniques (e.g. TGA, DSC, etc.) can only detect the total moisture loss over time and temperature by heating the sample uniformly, only global information is possible. For the purpose of detecting moisture transport across the sample, the data should be temporally- and spatially-resolved, such as to provide insight about the moisture distribution over time. With such information, further features about the drying behavior, e.g. drying front speed, temperature and vapour pressure, can be quantitatively derived and cross-referenced with specific formulation characteristics that are unique to each material. To this end, use is made of a home-built high-temperature Nuclear Magnetic Resonance (NMR) setup, which has been temperature calibrated and tested for performing first-drying measurements on a whole survey of different castables: Regular Castables (RC), Low-Cement Castables (LCC) and Non-Cement Castables (NCC). Samples were prepared from

each materials family. Within each family, the additives were varied for comparison. The experiments were conducted with an average heating rate of 1-2 °C/minute.

The results of this project reveal that drying behavior correlates with control of various key material parameters, such as binder content, water demand and additives. The LCCs display the most extreme pressures, due to the relatively lower water demand and binder content. The microsilica-containing LCC Fume especially approaches very high pressures, i.e., 4 MPa, as the temperature of the drying front starts at 200 °C and nears 250 °C just before dry-out occurs. RC/LCC MIPORE Fume (a variant of LCC Fume) display the lowest vapour pressures (0.1-0.5 MPa). The first-stage of drying, preceding the development of a drying front, corresponds to a rapid moisture loss. This stage of drying can be controlled via external boundary conditions, such as the heat input. However, the second and final stage of drying, corresponding to moisture levels below the critical moisture content, is entirely determined by the internal pore structure. In fact, the speed of the drying front in this range is almost the same for most materials considered in this study and independent of the heat flux, as well as behaving linear with time. Therefore, in the final stage of drying the heating rates must be as slow as possible, such as to prevent a possible explosion as a result of the high steam pressures.

Furthermore, a simple vapour transport model was used in which the high-temperature vapour permeability, corresponding to internally limited drying, was the only free parameter. By employing this simple model, we were able to relate the high-temperature boiling front behavior of the different materials with the permeability. In this way, we can interpret the material drying behavior on the basis of the unique characteristics of each material family, i.e. microstructure. These characteristics can furthermore be correlated with the formulation properties of the chosen material.

Up to this point, several material parameters were varied, e.g. water demand, binder content, etc. In an additional study we focused on drying as a function of only one material parameter: the microstructural permeability. In the first set of experiments, a polypropylene fiber-containing material was evaluated next to a fiber-free reference. This was done in order to quantify the influence of permeable pathways generated by the evaporation of fibers at 150-200 °C, on the vapour transport. To this end, the material chosen was microsilica gel-bonded NCC. What was found was that fiber-containing materials yielded a boiling front temperature in the range of 150-200 °C and vapour pressure of 0.5-1.5 MPa, in some cases

even stagnating until the end of the experiment. In contrast, the fiber-free materials displayed a boiling front temperature, which gradually climbed well above 200 °C at a corresponding vapour pressure of nearly 4 MPa.

Besides fibers, the use of a commercially new permeability enhancing active compound called MIPORE 20, was also investigated for the matrix system of LCC Fume. Again, a MIPORE-free reference sample was compared with a MIPORE-containing sample in order to assess the effects of the active mineral compound on the vapour permeability. Unlike fibers, which do not participate in the hydration process and burn out and evaporate at temperatures above 150 °C, MIPORE does not melt but undergoes some phase transformation in the temperature range of 100-150 °C. What was found was that the boiling front emerges a little above 100 °C and continues on until 150 °C, which is much lower than the 200 °C starting temperature of the MIPORE-free sample.

In a final study, the drying behavior of pine wood under the same heating conditions as drying of castables was investigated in order to compare the physical and thermal properties of both materials. It was found that a steep temperature gradient develops in wood on the order of several hundred °C/m as compared to castables. The effect of this steep gradient is that the high vapour pressure forces moisture to evaporate toward the surface or travel to the back region of the sample, which is cooler, and thus results in a local increase in the moisture content. Furthermore, the temperature of evaporation is around the normal boiling point of water, i.e. 100 °C, which remains constant throughout the experiment. Both of these observations reflect the different thermal properties of wood, as well as revealing a much higher vapour permeability.



---

## Samenvatting

---

Vuurvaste castables (gietproducten) met een hoog aluminiumoxide-gehalte zijn van vitaal belang voor de prestaties van een gietpan in een hoogoven, zodat deze fysieke en thermische duurzaamheid garandeert bij de smelttemperatuur van staal in het temperatuurbereik van 1000 tot 1750 °C. Castables van calcium aluminiumoxide/hydrateerbare aluminiumoxide in het bijzonder vormen een serieuze uitdaging met betrekking tot het verwijderen van de fysische en chemisch gecombineerde watercomponenten uit het poreuze netwerk voordat ze volledig in gebruik worden genomen. Vanwege het hoge risico van gegenereerde stoomdrukken die het materiaal vernietigen bij temperaturen boven het kookpunt van water, moeten castables worden voorgedroogd met minder dan 1 °C/minuut om een veilige afvoer van het vocht te garanderen. De gevaarlijke uitroeiingsfase (100-300 °C) en de ontleding van de hydraatfasen (200-300 °C) vormen de grootste zorg tijdens het opwarmen. Daarom zal een kwantitatief begrip van de transportprocessen die de eerste droging bepalen (100-300 °C), ingenieurs helpen bij het selecteren van geschikte verwarmingsschema's voor een bepaalde set materialen. Bovendien kan het in kaart brengen van de invloed van verschillende belangrijke parameters, zoals verwarmingssnelheid, waterbehoefte, bindmiddelgehalte en uithardingstijd, op drooggedrag ook inzicht verschaffen voor het optimaliseren van het droogschema. Omdat de materialen feitelijk aan één kant worden verwarmd, kan het drogen van castables worden beschouwd als een eendimensionaal verwarmingsprobleem.

Aangezien de meeste technieken (bijvoorbeeld TGA en DSC) alleen het totale vochtverlies over tijd en temperatuur kunnen kwantificeren door het monster uniform te verwarmen, is alleen globale informatie te verkrijgen. Voor het meten van vochttransport door het monster is plaats- en tijdafhankelijke informatie vereist, zodat inzicht in de vochtverdeling in de tijd wordt verkregen. Met dergelijke informatie kunnen verdere kenmerken van het drooggedrag, bijvoorbeeld droogsnelheid, temperatuur en dampdruk, kwantitatief worden afgeleid en gerelateerd aan unieke materiaaleigenschappen. Hiertoe wordt gebruik gemaakt van een zelfgebouwde Nuclear Magnetic Resonance (NMR)-

opstelling voor metingen bij hoge temperaturen, die op temperatuur is gekalibreerd en getest voor het uitvoeren van eerste-droogmetingen op verschillende castables: Regular Castables (RC), Low-Cement Castables (LCC) en Non-Cement Castables (NCC). Monsters werden bereid uit elke materialenfamilie. Binnen elke familie werden de additieven ter vergelijking gevarieerd. De experimenten werden uitgevoerd met een gemiddelde verwarmingssnelheid van 1-2 °C/minuut.

De resultaten van dit project laten zien dat het drooggedrag correleert met verschillende belangrijke materiaalparameters, zoals bindmiddelgehalte, waterbehoefte en additieven. De LCC's vertonen de meest extreme drukken, vanwege de relatief lagere waterbehoefte en het bindmiddelgehalte. De microsilica-bevattende LCC Fume in het bijzonder benadert zeer hoge drukken van 4 MPa, omdat de temperatuur van het droogfront begint bij 200 °C en bijna 250 °C nadert vlak voordat het uitdrogen optreedt. RC / LCC MIPORE Fume (een variant van LCC Fume) ondervindt de laagste dampdrukken (0,1-0,5 MPa). De eerste fase van het drogen, voorafgaand aan de ontwikkeling van een droogfront, komt overeen met snel vochtverlies. Deze droogfase kan worden beheerst via externe randvoorwaarden, zoals de warmtetoever. De tweede en laatste droogfase, overeenkomend met vocht niveaus onder het kritische vochtgehalte, wordt echter volledig bepaald door de interne poriestructuur. De snelheid van het droogfront is in dit bereik lineair met de tijd en onafhankelijk van de warmteflux, en bijna gelijk voor de meeste materialen die in deze studie werden behandeld. In de laatste fase van het drogen moeten de verwarmingssnelheden daarom zo laag mogelijk zijn, om een mogelijke explosie als gevolg van de hoge stoomdrukken te voorkomen.

Verder werd een eenvoudig damptransportmodel gebruikt waarbij de dampdoorlatendheid bij hoge temperaturen, overeenkomend met intern gelimiteerd drogen, de enige vrije parameter was. Door dit eenvoudige model te gebruiken, konden we het kookgedrag bij hoge temperaturen van de verschillende materialen in verband brengen met de permeabiliteit. Op deze manier kunnen we het drooggedrag interpreteren op basis van de unieke kenmerken van elke materiaalfamilie, in termen van de microstructuur. Deze eigenschappen kunnen bovendien worden gecorreleerd met de formuleringseigenschappen van het gekozen materiaal.

We hebben verschillende materiaalparameters gevarieerd, zoals waterbehoefte en bindmiddelgehalte. In een aanvullend onderzoek hebben we ons gericht op drogen als functie



van slechts één materiaalparameter: de microstructurele permeabiliteit. In de eerste reeks experimenten werd een polypropyleenvezel-bevattend materiaal geëvalueerd naast een vezelvrije referentie. Dit werd gedaan om de invloed van permeabele paden die worden gegenereerd door de verdamping van vezels bij 150-200 °C op het damptransport te kwantificeren. Hiertoe was het gekozen materiaal micro-silicagel-gebonden NCC. De vezel-bevattende materialen gaven een kookfronttemperatuur in het bereik van 150-200 °C en een dampdruk van 0,5-1,5 MPa, in sommige gevallen zelfs stagnerend tot het einde van het experiment. De vezelvrije materialen daarentegen vertoonden een kookfronttemperatuur die geleidelijk ruim boven de 200 °C klom bij een overeenkomstige dampdruk van bijna 4 MPa.

Naast vezels werd ook het gebruik van een commercieel nieuwe permeabiliteit-verhogende actieve stof, onder de naam MIPORE 20, onderzocht voor het matrixsysteem van LCC Fume. Wederom werd een MIPORE-vrij referentiemonster vergeleken met een MIPORE-bevattend monster om de effecten van de actieve minerale component op de dampdoorlaatbaarheid te beoordelen. In tegenstelling tot vezels, die niet deelnemen aan het hydratatieproces en doorbranden en verdampen bij temperaturen boven 150 °C, smelt MIPORE niet maar ondergaat een fasetransformatie in het temperatuurbereik van 100-150 °C. Het kookfront komt iets boven de 100 °C uit en gaat door tot 150 °C, wat veel lager is dan de 200 °C van het MIPORE-vrije monster.

In een laatste studie werd het drooggedrag van dennenhout onder dezelfde verwarmingsomstandigheden als het drogen van castables onderzocht om de fysische en thermische eigenschappen van beide materialen te vergelijken. Een steile temperatuurgradiënt ontwikkelt zich in het hout met waarden in de orde van enkele honderden °C/m. Het effect van deze steile gradiënt is dat de hoge dampdruk ervoor zorgt dat vocht zich als damp naar het oppervlak of naar het achterste gedeelte van het monster verplaatst. De lagere temperaturen in het achterste gedeelte van het monster resulteren in een lokale toename van het vochtgehalte. Verder ligt de verdampingstemperatuur rond het normale kookpunt van water, d.w.z. 100 °C, dat constant blijft gedurende het experiment. Beide observaties weerspiegelen de verschillende thermische eigenschappen van hout en onthullen een veel hogere dampdoorlatendheid.



---

## Journal Publications

---

“One-dimensional NMR imaging of high-temperature first-drying in monolithics”, **A.J. Barakat**, L. Pel, O.C.G. Adan. *Applied Magnetic Resonance*, **49**, pp. 739-753, 2018

“Moisture transport in pine wood during one-sided heating studied by NMR”, T. Arends, **A.J. Barakat**, L. Pel. *Experimental Thermal and Fluid Science*, **99**, pp. 259-271, 2018

“Setting characteristics, mechanical properties and microstructure of cement pastes containing accelerators mixed with Superabsorbent polymers (SAPs): an NMR study combined with additional methods”, Y. Ji, Z. Sun, C. Chen, L. Pel, **A. Barakat**. *Materials*, **12**, pp. 1-14, 2019.

“Direct observation of the moisture distribution in calcium aluminate cement and hydratable alumina-bonded castables during first-drying: an NMR study”, **A.J. Barakat**, L. Pel, O. Krause, O.C.G. Adan. *American Ceramic Society*, 2019 (accepted)

“The effect of permeability enhancement on dry-out behavior of CA- and microsilica gel-bonded castables as determined by NMR” **A.J. Barakat**, L. Pel, O.C.G. Adan, B. Myhre, H. Peng, C. Wohrmeyer, O. Krause. *Ceramics International*, 2019 (submitted).



---

## Acknowledgments

---

I would first like to acknowledge my research group TPM for giving me the opportunity to complete my PhD in a topic that was both very interesting and formative to my growth as a researcher. I relied on the knowledge and resources of many invaluable people without whom I could never have finished my work.

The first person I would like to acknowledge is my supervisor Leo for guiding me throughout my PhD project and giving me direction when I was hopeless. It was not without difficulty, and took some time for me to find the right “rhythm” of communication and output, but in the end it paid off and I am grateful for it. And of course, I am very proud of the work and final results we generated.

To my promoter Olaf, thank you for your counsel during the final stages of publishing and finalizing everything. There were moments during writing which were foggy and confusing, but your signals helped me quite a lot. My second promoter, Olaf Krause, your knowledge on the material science aspect of the project was enormously insightful and helped improve the quality of the thesis. I believe our different points of view on the subject were also quite constructive in the end. Furthermore, my project could not have been completed without the collaboration, support and direction of my industrial partners: Tata Steel, Almatris, Imerys Aluminates and Elkem. They were always there to advise and inform me on materials applications and quick to respond to my inquiries.

Henk, thank you for having discussions with me from time to time about my data analysis and helping me clarify some ambiguities in the final research results. You were always rigorous and to the point. Bart, I appreciated your input and feedback during group meetings, and otherwise, on instrumental issues and COMSOL modeling.

The construction of my experimental setup required a lot of machining and manufacturing expertise, which could not have been possible without the excellent handywork of Henk and Gini from the workshop.

Jef: I cannot overstate the value of your knowledge of RF systems and NMR troubleshooting and how resourceful you were whenever I had technical difficulties with the setup. And you were always very kind and considerate with me, which I greatly appreciated. Hans: you were an encyclopedia of chemistry, materials and manufacturing knowledge when I was constructing my setup. Perfection was your highest quality. I lost count of how many times you supplied me with new, high-functioning thermocouples on demand. I also had many nice conversations with both of you during coffee break, which I will greatly miss.

To my other peers and colleagues, current and former, Thomas, Philip, Jelle, Pim, Raheleh, Leyla, Benjamin, Anja, Rick, Natalia, Kees, Cemal, Okan, Negar, Ozlem, Sofiia, Sonia, Karel, Ji, Faiyas and everyone else who I worked with, thank you for contributing to a healthy working environment. Pim, I owe you for being an engaging (office) roommate in the beginning and helping me at the start of my PhD whenever I requested it. Thomas, you were always willing to assist me when needed and your computational craftsmanship in matlab was beyond helpful. Not to mention the fun times we occasionally had watching SNL and listening to Hip Hop music during breaks. With some of you, we also became good friends over the course of 6 years. Thomas, Philip, Jelle we had some marvelous times outside of the office- many dinners and excursions in the city center.

Outside of TPM and the university, I was fortunate enough to befriend a very interesting and diverse assortment of people- you know who you are-with whom I shared some splendid times in the greater Eindhoven area. Fabulous dinner parties, late night conversations and hilarious moments. You were always just a phone call away. Thanks for always being there. Memories were definitely made.

Finally, of course I would like to acknowledge my parents, Abtihal and Jamal, to whom I am eternally grateful for giving me everything I needed in life. I know tolerating the long distance from home, USA, as I was pursuing my postgraduate studies was not easy, so thank you. Mom, I also appreciated you checking up on me all the time. To my brother and best friend, Mahdi, your regular visits to Eindhoven, as well as your uncomplaining assistance around the house and superb culinary skills, really meant a great deal to me. I cant wait to see all of you again.

---

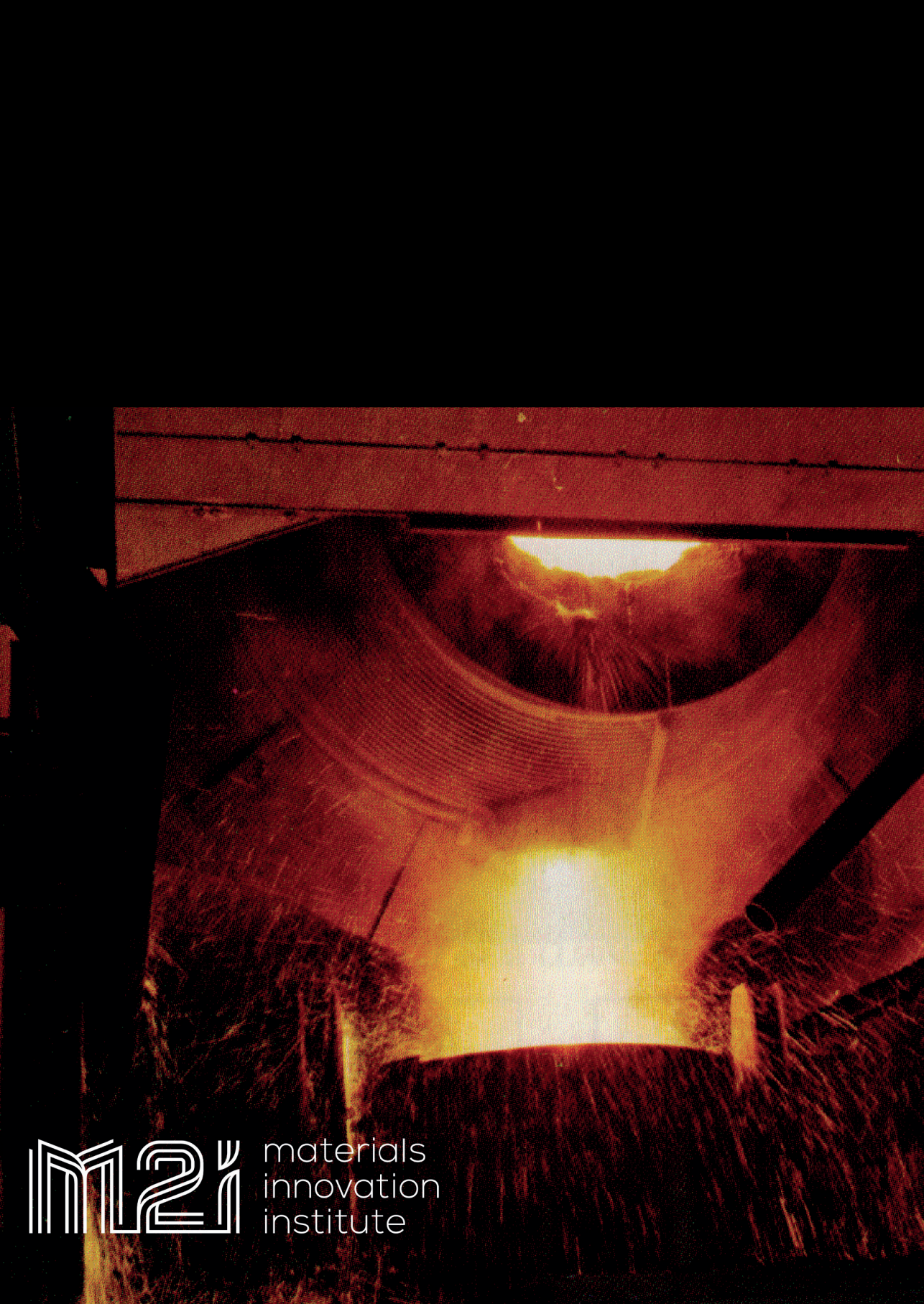
## **Curriculum Vitae**

---

Ahmed Jamal Barakat was born on the 23<sup>rd</sup> of October, 1985 in Los Angeles, United States. After completing his diploma at Skyline High School in Salt Lake City, Utah, he received a Bachelor's and Master's degree in Physics and Nanoscience from Arizona State University from 2011-2013. Starting in 2013, he pursued his PhD research at the Eindhoven University of Technology within the group of Transport in Permeable Media of the Applied Physics department. The corresponding results of that project are the subject of this thesis.







**M2I** materials  
innovation  
institute